# LECTURE NOTES  3

## Davide Bigoni

# Selected Mechanical Problems in Structural Ceramics

AMAS

**Centre of Excellence for Advanced Materials and Structures**

# AMAS LECTURE NOTES

*Series Editors*:

*Executive Committee of AMAS*:

    Zenon Mróz (*Scientific Coordinator*)

    Krzysztof Doliński

    Wojciech Nowacki

    Henryk Petryk

    Andrzej Siemaszko

    Kazimierz Sobczyk

*Executive Editor*:

    Józef Joachim Telega

*Edition of this volume has been partially supported by the European Commission*

# Preface

Part of my research activity in the last few years has potentially applications in the field of ceramic materials. In the notes which follow, I have not attempted to provide a comprehensive guide to the mechanical behaviour of ceramics. Instead, I have collected together a number of unpublished contributions, in which I was involved at different levels. These regard particular and often unrelated aspects of mechanical behaviour of ceramics. Moreover, results have been obtained following an approach peculiar to Solid Mechanics and they are not based on extensive experimental results. However, I hope that some of the presented material might stimulate the scientific curiosity of researchers in the field.

All the results presented have been obtained in co-operation with different researchers, to which I would express my sincere gratitude. In particular, I owe much to Giancarlo Celotti, Goffredo De Portu, Leonardo Esposito, Alessandro Gajo, Massimiliano Gei, Stefano Guicciardi, Alexander B. Movchan, Andrea Piccolroaz, Enrico Radi, Sergei K. Serkov, Anna Tampieri, Antonella Tucci, Monica Valentini.

Povo di Trento, January 2002. *Davide Bigoni*

# Contents

# An introduction to the mechanical behaviour of ceramics

D. Bigoni [1]

*Mechanical behaviour of ceramics is summarized with emphasis on some issues that will be addressed in the subsequent chapters. Elastic, plastic and viscous behaviour, fracture and large strain effects are considered.*

## 1.1. Preliminaries

Since neolithic times ceramics have played a fundamental role in man's development and survival (Scott, 1954). But during the last thirty years the technology of ceramic design and production has undergone a spectacular growth.

The peculiar optical, electrical, and magnetic characteristics, connected to the excellent thermo-chemical stability at high temperatures drives the industrial exploitation of ceramics. Following a modern definition of ceramics, these are materials manufactured from non-metallic, inorganic substances exhibiting high thermal stability. A broad class of materials falls within the

---

[1] Dipartimento di Ingegneria Meccanica e Strutturale, Università di Trento, Via Mesiano 77, 38050 Trento, Italy.

above definition, including – for instance – superconductors, tiles, diamonds, zirconia, alumina, and glasses (Pampuch, 1991).

Structural ceramics are the main focus of the present notes. These differ from traditional ceramics essentially because of their high purity and the presence of substances different from silicates, such as oxides, carbides, nitrides, etc. Moreover, *mechanical properties* are a crucial design target within this class of materials.

Our main interest here is the mechanical behaviour of structural ceramics related to fracture initiation and growth under service conditions. In particular, the present monograph is articulated as follows.

A brief review of the mechanical behaviour of ceramics is included in Chapter 1. The treatment is far from exhaustive and the interested reader is referred to De Portu (1992), Evans (1984), Green (1998), Lawn (1993), Munz and Fett (1999) for a comprehensive view of field of ceramics and to Ashby and Jones (1980), Bridgman (1952), Cottrel (1964), McClintock and Argon (1966) and Nadai (1950) for more general notions of material science.

Stable, rectilinear crack propagation in zirconia-containing ceramics is analyzed in Chapter 2. The focus is on the toughening mechanism related to stress-induced phase transformation in the near crack tip zone.

Deflection of crack path as induced by inhomogeneities in the form of cavities, rigid/soft inclusions or cracks is analyzed in Chapter 3. Toughening may be connected to crack deflection, so that the investigation becomes important for ceramic materials.

A peculiar failure mode, namely, failure under uniaxial compression is analyzed in Chapter 4 for silicon nitride at high temperature. Performed experiments demonstrate an elastic-plastic behaviour. Failure is interpreted in the framework of bifurcation theory.

Chapter 5 is devoted to the analysis of cold forming of powders. Problems related to forming technology involve the major part of ceramic materials and are connected to the analysis of density and residual stress distributions in greens.

## 1.2. Elastic behaviour

Deformation in the elastic range of crystalline materials is related to (reversible) movements of atoms, which – for instance – may be experimentally demonstrated using x-ray diffraction during deformation of a material ele-

ment. At room temperature, linear elasticity is a common behaviour of many ceramics, such as alumina ($Al_2O_3$) or silicon nitride ($Si_3N_4$).

Within the realm of linear elasticity, stress $\sigma$ and strain $\epsilon$ are related through a linear relationship

$$\sigma = \mathcal{E}[\epsilon], \tag{1.1}$$

where the fourth-order tensor $\mathcal{E}$ may describe a broad class of *anisotropic* behaviours ($\mathcal{E}$ is characterized, in the most general case, by 21 material constants, when a stress potential is assumed). The behaviour of *single-crystals* is always anisotropic and the particular class of crystal symmetry defines the number of elastic constants (Love, 1927). For instance, three or five elastic constants describe cubic or hexagonal single crystals (Fig. 1.1).
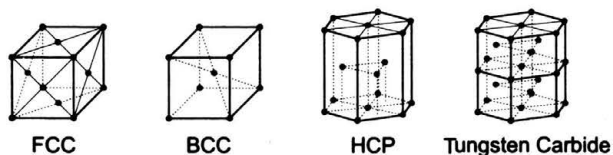


FIGURE 1.1. Crystal lattice structures: Face Centered Cubic, Body Centered Cubic, Hexagonal Close Packed, Tungsten carbide.

At a macroscopic scale, *polycrystalline ceramics* often consist of a random array of single-crystals, so that an isotropic elastic behaviour follows. In this case, the elastic constants reduce to two, the Young modulus $E$ and the Poisson's ratio $\nu$. The elastic fourth-order tensor thus becomes:

$$\mathcal{E} = \lambda I \otimes I + 2\mu I \boxdot I, \tag{1.2}$$

where

$$\lambda = \frac{\nu E}{(1+\nu)(1-2\nu)}, \qquad \mu = \frac{E}{2(1+\nu)}, \tag{1.3}$$

are the Lamé constants ($\mu$ is the shear modulus, often denoted by $G$) and $I \otimes I$ and $I \boxdot I$ are fourth-order tensors defined, for every second-order tensor $A$, in the following way:

$$I \otimes I[A] = (\operatorname{tr} A)I, \qquad I \boxdot I[A] = \frac{1}{2}(A + A^T). \tag{1.4}$$

Indicative values of the elastic constants for some materials at room temperature are reported in Table 1.1 (data taken from Green, 1998; Kingery et al. 1960; Meyers and Chawla, 1999; Munz and Fett, 1999; Shackelford, 1985).

Table 1.1. Elastic constants $E$, $\nu$ at 20°C.

| Material | Young modulus $E$ (GPa) | Poisson's ratio $\nu$ |
|---|---|---|
| 1040 carbon steel | 200 | 0.3 |
| 304 stainless steel | 193 | 0.29 |
| 3003-H14 aluminum | 70 | 0.33 |
| Copper | 129.8 | 0.343 |
| Polyamides (nylon 66) | 2.8 | 0.41 |
| Acetals | 3.1 | 0.35 |
| Borosilicate glass | 69 | 0.2 |
| Silicon nitride (HPSN) | 320 | 0.28 |
| Sintered alumina (95% dense) | 320 | 0.20-0.26 |
| Sintered stabilized zirconia | 150-240 | 0.22-0.30 |
| Ceramic fibre SiC | 430 | – |
| Glass fibre (S-glass) | 85.5 | – |
| Polymer fibre (Kevlar) | 131 | – |
| Ceramic whisker $Al_2O_3$ | 430 | – |
| $Al_2O_3$ whiskers (14 vol%) in epoxy | 41 | – |

## 1.3. Fracture

At room temperature, ceramics are typically brittle materials, which usually fail as a consequence of rapid and catastrophic fracture propagation [2]. Perhaps the major research goal of the last thirty years (in the field of ceramics!) has been indeed directed to emend this characteristic, which is unacceptable in many technological applications.

There are essentially two approaches to linear elastic fracture mechanics: the energy approach and the stress intensity approach. The former was initiated by Griffith (1920) and is equivalent to the latter, that is followed below (for a detailed presentation of fracture mechanics see Anderson, 1995; Broberg, 1999; Lawn, 1993). With reference to the coordinate system introduced in Fig. 1.2, the asymptotic stress fields near a crack tip in an isotropic, linearly elastic material, subject to symmetric boundary conditions – the so-called Mode I problem – can be expressed as (Westergaard, 1939)

$$\left. \begin{array}{c} \sigma_{11}(r,\theta) \\ \sigma_{22}(r,\theta) \\ \sigma_{12}(r,\theta) \end{array} \right\} = \frac{K_I}{\sqrt{2\pi r}} \cos\frac{\theta}{2} \left\{ \begin{array}{c} (1 - \sin\frac{\theta}{2}\sin\frac{3\theta}{2}) \\ (1 + \sin\frac{\theta}{2}\sin\frac{3\theta}{2}) \\ \sin\frac{\theta}{2}\cos\frac{3\theta}{2} \end{array} \right. \quad . \tag{1.5}$$

---

[2] Brittle crack propagation occurs essentially by bond rupture, for cracks of atomic sharpness.
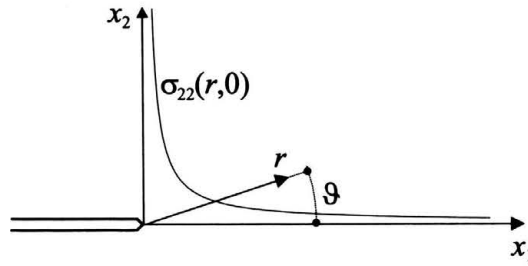
FIGURE 1.2. Polar and cartesian coordinates used to describe crack fields. The stress component $\sigma_{22}(r, 0)$ is also reported.

It should be noted that fields (1.5) satisfy equilibrium with null body forces

$$\mathbf{div}\boldsymbol{\sigma} = \boldsymbol{0}, \tag{1.6}$$

the traction-free boundary conditions on crack faces

$$\sigma_{22}(r, \pi) = \sigma_{12}(r, \pi) = 0, \tag{1.7}$$

and the symmetry condition ahead of the crack

$$\sigma_{12}(r, 0) = 0, \tag{1.8}$$

for *every value* of $K_I$.

Two key points emerge from an analysis of (1.5), namely:

- the stress field is proportional to the unknown amplitude $K_I$, the so-called *stress intensity factor*;
- the stress field is singular, in the sense that the stress approaches infinity when the distance to the crack tip $r$ tends to zero.

The stress intensity factor completely characterizes the near-tip stress state and therefore depends on the particular geometry of the loaded structure. For instance, in the case of an infinite plate subject to a remote tensile stress $\sigma$,

$$K_I = \sigma\sqrt{\pi a},$$

for a through-thickness crack of length $2a$ and

$$K_I = 1.12\,\sigma\sqrt{\pi a},$$

for an edge crack of length $a$.

Being the stress infinite at the crack tip, it cannot be sustained by any real material. However, the fracture concept introduced above follows from a mathematical model, so that on one hand a perfectly sharp crack is impossible in a real problem and, on the other hand, an elastic material is also an ideal notion. Consequently, *for brittle materials* it is assumed that the stress is high, though not infinite, at a real crack tip and that it is reasonably described by representation (1.5), at least outside a *process zone*, which is very small when compared to the problem size. Therefore, let us analyze loading of a structure containing a crack. Under the hypothesis that a given stress combination leads to failure, the achievement of this must correspond to the attainment of a critical value of the stress intensity factor $K_{Ic}$. A fundamental assumption of fracture mechanics is that the critical stress intensity factor depends only on the nature of the material and is therefore independent of the geometry and size of the fractured body. As a consequence, once $K_{Ic}$ is known for a given material, a failure analysis can be performed for a structure made up of that material.

In addition to the symmetric mode illustrated above, there are other two types of loading that a crack may experience, so that Mode I, Mode II and Mode III are distinguished (Fig. 1.3). However, brittle materials are more prone to fracture by normal tensile stresses than by shear stresses, so that Mode I loading has the most practical importance.



Mode I        Mode II        Mode III
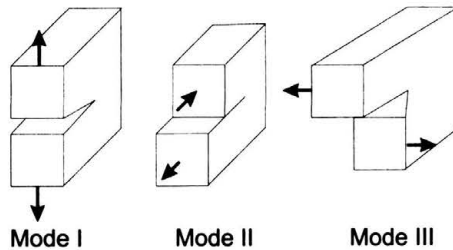
FIGURE 1.3. The three modes of crack loading.

The fracture toughness $K_{Ic}$ can be experimentally determined by introducing an artificial crack in a testing structure, subsequently loaded to failure. Different test settings are used for ceramic materials (Anderson, 1995; Green, 1998). Some indicative values of toughness in different materials are reported in Table 1.2 (data taken from Ashby and Jones (1980); Cook and Pharr, 1994; Evans, 1989; Green, 1998; Meyers and Chawla, 1999; Shackelford, 1985).

TABLE 1.2.  Toughness $K_{Ic}$ of materials at room temperature.

| Material | $K_{Ic}$ (MPa $\sqrt{m}$) |
|---|---|
| Mild steel | 140 |
| Medium-carbon steel | 51 |
| High strength steel (HSS) | 50-154 |
| Aluminum alloys | 23-45 |
| Cast iron | 6-20 |
| Rigid PVC | 3-7 |
| Polyamides (nylon 66) | 3 |
| Cement/Concrete | 0.2 |
| Soda-lime glass | 0.7-0.9 |
| $Al_2O_3$ | 3-5 |
| SiC | 3-4 |
| $Si_3N_4$ | 4-7 |
| Zirconia ceramics | 5-35 |
| E-glass (73.3 vol %) in epoxy | 42-60 |
| Fibre reinforced Glass/C | 20 |
| SiC fibres in SiC | 25 |
| SiC whiskers in $Al_2O_3$ | 8.7 |
| Wisker reinforced $Si_3N_4$ | 14 |

The above presented scenario for fracture is very simple. In reality, cracks interact with material microstructure, during propagation. This interaction strongly influences toughness. In view of the fact that brittleness still perhaps remains the most important limiting factor in the design of ceramics components, it follows that the understanding of the micromechanics of fracture propagation becomes crucially important. Following Green (1998), toughening mechanisms can be classified in three groups (Figs. 1.4–1.6):

1. Crack tip interactions:
   (a) crack bowing,
   (b) crack deflection.
2. Crack tip shielding:
   (a) transformation toughening,
   (b) microcrack toughening.
3. Crack bridging.

During crack bowing process, the crack front interacts with obstacles – such as tough second phase particles – impeding propagation and does not
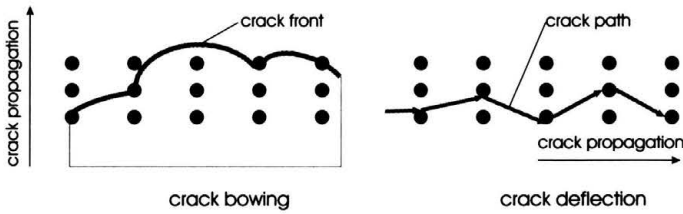
FIGURE 1.4. Crack tip interaction with a periodic composite.
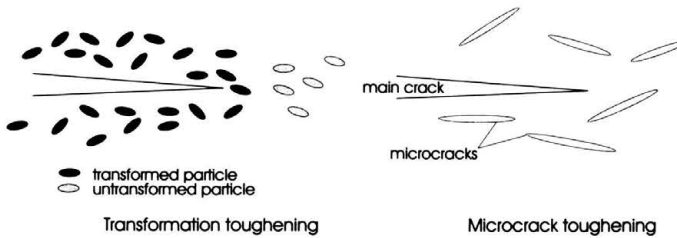


FIGURE 1.5. Crack tip shielding.
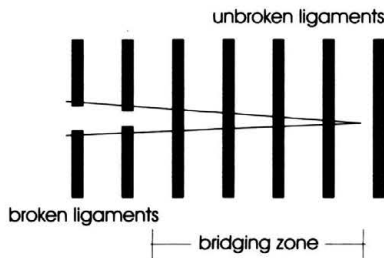


FIGURE 1.6. Crack bridging.

remain straight. This mechanism is related to an increase in toughness, as evidenced by Bower and Ortiz (1991).

Crack deflection occurs when fractures deviates from rectilinearity, so that mixed mode loading is involved. Note that crack deflection produces non-planar fracture, whereas crack bowing corresponds to nonlinear crack front. Both toughening mechanisms are often concurrent and strongly influenced by the morphology and contact conditions of the second-phase particles. Crack deflection, which is experimentally revealed by the roughness of the final fracture surface, was analyzed by Cotterel and Rice (1980) and Faber and

Evans (1983). An alternative analysis is provided in Chapter 3, under the assumption that the particles inducing deflection are far enough from the fracture trajectory.

Transformation toughening is related to dilatant, stress-induced phase transformation of particles in a ceramic matrix, a problem addressed in Chapter 2.

Microcracks can be present in ceramics as induced by the fabrication process or may nucleate as a consequence of a state of prestress or, finally, can be induced by stress.

Under certain circumstances, a microcracked zone around a larger crack may yield a crack tip shielding effect [3]. This effect, analyzed in (Evans and Faber, 1981; Evans and Fu, 1985; Fu and Evans, 1985; Clarke, 1984; Rose, 1986; Rubinstein, 1986 and Hutchinson, 1987; Duan et al., 1995), is however controversial in the sense that it may be almost entirely counterbalanced by the resistance reduction caused by the presence microcracks in the material (Ortiz, 1988; Ortiz and Giannakopoulos, 1989). Crack deflection as induced by interaction with a diluted distribution of cracks can also be analyzed with the model presented in Chapter 3.

Finally, crack bridging occurs when there are fibres or particles in the wake of the crack pinning its faces and therefore reducing the crack tip stress intensity factor (Rose, 1982, 1987; Cox and Marshall, 1988, 1994; Budiansky and Amazigo, 1989; Movchan and Willis, 1993; Movchan and Willis, 1996, 1997 a, b, 1998). With the exception of transformation toughening, crack bridging is the most important toughening mechanisms among all discussed above (Pezzotti, 1993; Pezzotti et al., 1996).

## 1.4. Plastic behaviour

Inelastic deformation is usually related to dislocation activity. In monolithic ceramic materials such as alumina, temperatures superior to 1300°C are needed to make dislocation motion appreciable. Therefore, although ceramics are crystalline materials like metals, plastic deformation is not exhibited in ordinary conditions. However, micromechanisms different from dislocation activity may also induce irreversible deformation. For instance, inelastic deformation of silicon nitride at high temperature is related to the viscous flow

---

[3] Porosity decreases toughening as evidenced by Rice, 1984; Zimmermann et al. (1998) and Zimmermann and Rödel (1998).

of a a glassy phase often present in the grain boundaries of this material. An example of such a behaviour is presented in Chapter 4. Completely different micromechanisms of plastic deformations take place during forming of ceramic powders. These are presented in Chapter 5 and, in summary, consist in rearrangements, deformation and collapse of particles. Finally, inelastic deformation is connected to phase transformation occurring – for instance – in zirconia-containing ceramics. Elastoplastic constitutive laws are therefore employed in Chapter 2, when analyzing transformation toughening during crack propagation.

Let us consider behaviour of an elastic-plastic material deformed in uniaxial tension, as illustrated in Fig. 1.7.



hardening/softening plasticity                    ideal plasticity
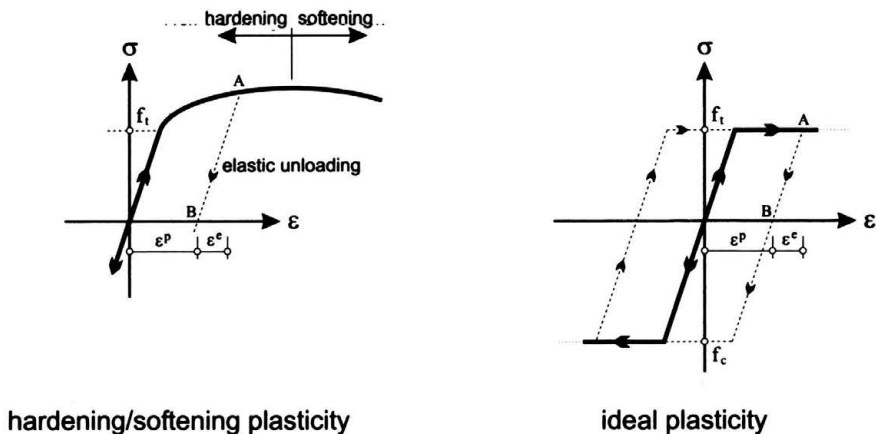
Figure 1.7.  Elastoplastic models.

When unloading occurs after a plastic state has been reached, e.g. point A, the inelastic deformation $\epsilon^p$ is not recovered. A key ingredient in any phenomenological theory of plasticity is the fact that plastic deformation is possible only when the stress state satisfies a yield criterion. For isotropic materials, a yield criterion may be visualized as a locus in the principal stress space representing elastic states of the material (Fig. 1.8). Plastic deformation is possible only when the stress state lies on the boundary of the yield locus, namely, the yield surface.

Plastic or elastic deformation actually takes place if a loading/unloading criterion is met. This criterion is necessarily *incremental*. In fact, starting from point A in Fig. 1.7, incremental plastic or incremental elastic deforma-

FIGURE 1.8. Yield surfaces in the principal stress space.

tions may occur. As a consequence, time independent, inelastic deformation is described by a rate theory, as briefly explained below (the interested reader is referred to Hill, 1950; Besseling and van der Giessen, 1994; Lubliner, 1998).

The skeleton of a generic phenomenological theory of plasticity usually consists in the following hypotheses:

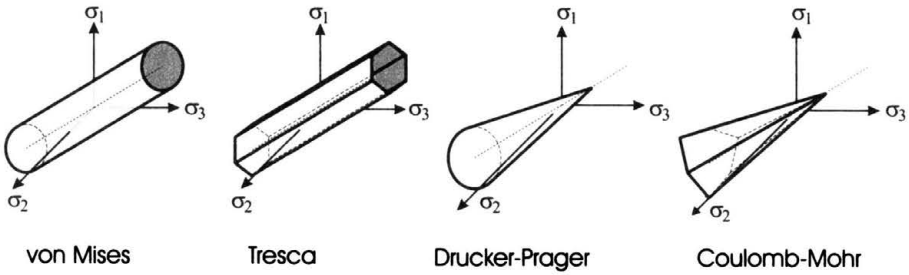$\mathcal{A}$1. Additive decomposition of total strain $\epsilon$ into an elastic part and a plastic part:

$$\epsilon = \epsilon^e + \epsilon^p. \tag{1.9}$$

$\mathcal{A}$2. Elastic law (1.1) defined by the constant fourth-order elastic tensor $\mathcal{E}$ and relating the stress to the elastic deformation:

$$\sigma = \mathcal{E}[\epsilon^e]. \tag{1.10}$$

$\mathcal{A}$3. Yield function defined in terms of stress $\sigma$ and $\mathcal{K}$, a generic set of internal variables of arbitrary tensorial nature, so that:

$$\begin{array}{ll} f(\sigma, \mathcal{K}) < 0 & \text{elastic behaviour is only possible,} \\ f(\sigma, \mathcal{K}) = 0 & \text{plastic deformation rate may occur,} \\ f(\sigma, \mathcal{K}) > 0 & \text{is not defined.} \end{array} \tag{1.11}$$

$\mathcal{A}$4. Plastic flow rule in terms of a symmetric, second-order tensor $\mathbf{P}$, the flow mode tensor:

$$\dot{\epsilon}^p = \dot{\Lambda}\, \mathbf{P}, \tag{1.12}$$

where $\dot{\Lambda} \geq 0$ is the non-negative plastic multiplier and a dot over a symbol denotes the derivative with respect to a time-like, non-decreasing scalar parameter governing the rate problem.

$\mathcal{A}$5. Hardening law:

$$\dot{\mathcal{K}} = \dot{\Lambda}\,\bar{\mathcal{K}}, \tag{1.13}$$

where $\bar{\mathcal{K}}$ is a continuous function of the state variables.

The above equations yield the *rate constitutive equations* in the general form (Bigoni, 2000)

$$\dot{\sigma} = \begin{cases} \mathcal{E}[\dot{\epsilon}] - \frac{1}{H} < \mathbf{Q} \cdot \mathcal{E}[\dot{\epsilon}] > \mathcal{E}[\mathbf{P}] & \text{if } f(\sigma, \mathcal{K}) = 0, \\ \mathcal{E}[\dot{\epsilon}] & \text{if } f(\sigma, \mathcal{K}) < 0, \end{cases} \tag{1.14}$$

where the operator $< \cdot >$ denotes the Macaulay brackets which associates to any scalar $\alpha$ the value $< \alpha >= \max\{\alpha, 0\}$, tensor $\mathbf{Q}$ is the yield function gradient

$$\mathbf{Q} = \frac{\partial f}{\partial \sigma},$$

and the plastic modulus $H$ is related to the hardening modulus $h$ through

$$H = h + \mathbf{Q} \cdot \mathcal{E}[\mathbf{P}]. \tag{1.15}$$

The hardening modulus $h$, defined as

$$h = -\frac{\partial f}{\partial \mathcal{K}} \cdot \bar{\mathcal{K}}, \tag{1.16}$$

describes the type of hardening of the material. In particular, $h$ is positive for strain hardening, negative for softening and null in the case of ideal plasticity. When $h$ is constant, linear hardening occurs, but $h$ may be function of the state, thus describing a nonlinear hardening law (Fig. 1.7). When the hardening is strictly positive, $h > 0$, the constitutive law (1.14) can be inverted

$$\dot{\epsilon} = \begin{cases} \mathcal{E}^{-1}[\dot{\sigma}] + \frac{1}{h} < \mathbf{Q} \cdot \dot{\sigma} > \mathbf{P} & \text{if } f(\sigma, \mathcal{K}) = 0, \\ \mathcal{E}^{-1}[\dot{\sigma}] & \text{if } f(\sigma, \mathcal{K}) < 0. \end{cases} \tag{1.17}$$

In the particular but relevant case in which the flow mode tensor is equal to the yield function gradient, $\mathbf{P} = \mathbf{Q}$, the yield function is called "associative".

Comparing to linear elasticity (1.1), two key points emerge from the analysis of the constitutive equations (1.14) or (1.17), namely:

- the constitutive equations (1.14) are written in rate form. This does not imply dependence on physical time, rather time is identified with any scalar parameter governing the loading process.

- the constitutive equations (1.14) are *incrementally nonlinear*, due to the presence of the Macauley brackets.

It follows from the above points that in any problem of plastic flow, the constitutive equations have to be integrated with respect to the time-like parameter governing the flow.

## 1.5. Viscous behaviour

When deformation depends on physical time, the behaviour is viscous. Viscous flow, typical of fluids, may also occur in solids and its occurrence is related to the period of time over which the stress is applied [4]. The simplest viscous constitutive equations are those for an incompressible *Newtonian fluid*

$$\boldsymbol{\sigma} = -p\boldsymbol{I} + 2\eta\dot{\boldsymbol{\epsilon}}, \qquad \text{tr}\dot{\boldsymbol{\epsilon}} = \text{div}\boldsymbol{v} = 0, \qquad (1.18)$$

where $\eta$ is the viscosity of the fluid, $\boldsymbol{v}$ its velocity and $\dot{\boldsymbol{\epsilon}}$ the Eulerian strain rate (the symmetric part of the velocity gradient), finally, $p = -\frac{\text{tr}\boldsymbol{\sigma}}{3}$ is the pressure at a point of the fluid.

As a crucial point, we note that Eq. (1.18) relates the Eulerian strain rate to the current stress.

In a number of circumstances, fluids are involved in the industrial applications of ceramics, for instance during injection molding or slip casting. During the latter process, emulsions and slurries are usually employed, consisting of suspended solid particles in a fluid. Flow of these material is usually sensible to the volume fraction of particle and violate Newtonian behaviour in several ways. First, the viscous flow becomes nonlinear, so that the shear stress is a nonlinear function of strain rate. Second, the shear stress depends not only on the local strain rate, but also on its history (so-called "memory effect"). The latter is described by *viscoelasticity*, which – according to the Kelvin-Voigt scheme – can be viewed as an "parallel" combination of (1.1) and (1.18)

$$\boldsymbol{\sigma} = -p\boldsymbol{I} + 2\eta\dot{\boldsymbol{\epsilon}} + 2\mu\boldsymbol{\epsilon}, \qquad \text{tr}\dot{\boldsymbol{\epsilon}} = \text{div}\boldsymbol{v} = 0, \qquad (1.19)$$

---

[4] For instance, the hot rocks of the Earth's mantle may be considered as solid when deform under the action of seismic waves. On a completely different time scale – on the order of a million years – the same rocks are unable to support shearing stresses and flow as a fluid.

or – according to the Maxwell scheme – can be viewed as a "series" combination of (1.18) and (the rate of) (1.1)

$$\dot{\boldsymbol{\sigma}} = -\dot{p}\boldsymbol{I} + 2\mu\,\dot{\boldsymbol{\epsilon}} - \frac{1}{\tau}\,(p\boldsymbol{I} + \boldsymbol{\sigma})\,, \qquad \text{tr}\dot{\boldsymbol{\epsilon}} = \text{div}\boldsymbol{v} = 0, \qquad (1.20)$$

where $\tau = \eta/\mu$ is the relaxation time. Constitutive equations (1.19) and (1.20) describe two specific incompressible, viscoelastic behaviours (further details can be found in Malvern, 1969).

Finally, in applications at high temperature, ceramics often exhibit a time-dependent plastic deformation, the so-called *creep*. An elastic-viscoplastic behaviour can be defined as a generalization of (1.20), where a threshold for viscous behaviour is introduced (Duvaut and Lions, 1976; Loret and Prevost, 1990)

$$\dot{\boldsymbol{\sigma}} = \mathcal{E}\dot{\boldsymbol{\epsilon}} - \frac{1}{\tau}(\boldsymbol{\sigma} - \boldsymbol{\sigma}_0)H(f(\boldsymbol{\sigma}(t)), \qquad (1.21)$$

where $H$ is the Heaviside function ($H(x) = 1$ for $x > 0$, otherwise $H(x) = 0$), $f$ is the yield function, dependent on current stress $\boldsymbol{\sigma}(t)$, and $\boldsymbol{\sigma}_0$ is the projection of $\boldsymbol{\sigma}$ on the yield surface at time $t$. Differently from the usual definition employed in rate-independent elastoplasticity, positive values of $f(\boldsymbol{\sigma}(t))$ are fully allowed in (1.21). Constitutive equation (1.21) describes an elastic rate-indepedent behaviour within the yield function. When the stress intensity corresponds to positive values of the yield function, the material flows with a viscous deformation rate proportional to $|\boldsymbol{\sigma} - \boldsymbol{\sigma}_0|$.

## 1.6. Large strains

Large deformations may occur in the elastic or inelastic range. For instance, ceramic whiskers – such as SiC – or silica-glass fibres may often be so strong that deformation can proceed beyond the limit of linearity to a range of nonlinear elastic deformation (Green, 1998). Moreover, during compaction of ceramic powders large plastic strains occur, while elastic deformation usually remains small. An example of this large strain elastic-plastic behaviour is presented in Chapter 5.

In other cases, deformations are actually small, but effects such as *instabilities* (for instance buckling of fibres which may occur in a composite) may be properly captured only within a theory taking into account large strain effects. For instance, failure of silicon nitride cylinders subject to uniaxial compression is described in Chapter 4, employing bifurcation theory of

finitely deformed, elastic solids. Strains are actually not so large in that case, but large strain *effects* are necessary to predict bifurcations.

In a large strain theory, the constitutive equations involve *objective measures* of stress and strain. For instance, in an Eulerian description, an elastic constitutive law may be generically written in the form:

$$\boldsymbol{\sigma} = \beta_0 \boldsymbol{I} + \beta_1 \boldsymbol{B} + \beta_2 \boldsymbol{B}^{-1}, \qquad (1.22)$$

where $\boldsymbol{B}$ is the *left Cauchy-Green strain tensor* and the scalars $\beta_i$, $i = 0, 1, 2$ are functions of the invariants of $\boldsymbol{B}$ (Gurtin, 1981).

In any rate theory of plasticity at finite strain *objective rates* of stress and strain replace the rates $\dot{\boldsymbol{\sigma}}$ and $\dot{\boldsymbol{\epsilon}}$. A presentation of finite strain theory is far beyond the scope of the persent introduction and the interested reader is referred to (Bigoni, 2000; Gurtin, 1981; Ogden, 1984; Holzapfel, 2000).


## 1.7.  References

ANDERSON, T.L. (1995), *Fracture Mechanics*, (2nd edition), CRC Press.

ASHBY, M.F. and JONES, D.R.H. (1980), *Engineering Materials. An Introduction to Their Properties and Applications*, Pergamon Press, Elmsford, N.Y.

BESSELING, J.F. and VAN DER GIESSEN, E. (1994), *Mathematical Modelling of Inelastic Deformation*, Chapman & Hall, London.

BIGONI, D. (2000), Bifurcation and instability of nonassociative elastoplastic solids, in: *Material Instabilities in Elastic and Plastic Solids*, Petryk, H., (Ed.), CISM Lecture Notes N.414, Springer-Verlag, Wien, pp.1-52.

BOWER, A.F. and ORTIZ, M. (1991), A 3-dimensional analysis of crack trapping and bridging by tough particles, *J. Mech. Phys. Solids*, Vol.39, pp.815-858.

BROBERG, B.K. (1999), *Cracks and Fracture*, Academic Press, London.

BUDIANSKY, B. and AMAZIGO, J.C. (1989), Toughening by aligned, frictionally constrained fibres, *J. Mech. Phys. Solids*, Vol.37, pp.93-109.

BRIDGMAN, P.W. (1952), *Studies in Large Plastic Flow and Fracture*, McGraw-Hill, New York.

CLARKE, D.R. (1984), A simple calculation of process-zone toughening by microcracking, *J. Am. Ceram. Soc.*, Vol.C-15, January 1984.

COOK, R.F. and PHARR, G.M. (1994), Mechanical properties of ceramics, in: *Materials Science and Technology*, Chan, R.W., Haasen, P. and Kramer, E.J., (Eds.), Vol.11 – Structure and Properties of Ceramics, Swain, M.V., (Ed.), pp.341-384.

COTTEREL, B., and RICE, J.R. (1980), Slightly curved or kinked cracks, *Int. J. Fracture*, Vol.16, pp.155-169.

COTTREL, A.H. (1964), *The Mechanical Properties of Matter*, John Wiley & Sons, New York.

COX, B.N. and MARSHALL, D.B. (1988), A J-integral method for calculating steady-state matrix cracking stresses in composites, *Mech. Materials*, Vol.7, pp.127-133.

COX, B.N. and MARSHALL, D.B. (1994), Concepts for bridged cracks in fracture and fatigue, *Acta Metall. Mater.*, Vol.42, pp.341-363.

DE PORTU, G. (1992), *Introduction to Mechanical Behaviour of Ceramics*. Consiglio Nazionale delle Ricerche, CNR-IRTEC, Edit Faenza Printers.

DUAN, K., MAI, Y.W., and COTTEREL, B. (1995), On the paradox between crack bridging and crack interaction in quasi-brittle materials, *J. Europ. Ceram. Soc.*, Vol.15, pp.1061-1064.

DUVAUT, G. and LIONS, J.L. (1976), *Inequalities in Mechanics and Physics*, Springer-Verlag, Berlin.

EVANS, A.G. (1984), *Fracture in Ceramic Materials*, Noyes, Park Ridge.

EVANS, A.G. (1989), The new high toughness ceramics, *ASTM STP 907, American Society for Testing and Materials*, Philadelphia, pp.274-297.

EVANS, A.G. and FABER, K.T. (1981), Toughening of ceramics by circumferential microcracking, *J. Am. Ceram. Soc.*, Vol.64, pp.394-398.

EVANS, A.G. and FU, Y. (1985), Some effects of microcracks on the mechanical properties of brittle solids – II. Microcrack toughening, *Acta Metall.*, Vol.33, pp.1525-1531.

FABER, K.T. and EVANS, A.G. (1983), Crack deflection process-I and II. Theory and experiments, *Acta Metall.*, Vol.31, pp.565-576 and 577-584.

FU, Y. and EVANS, A.G. (1985), Some effects of microcracks on the mechanical properties of brittle solids – I. Stress, strain relations. *Acta Metall.*, Vol.33, pp.1515-1523.

GREEN, D.J. (1998), *An Introduction to the Mechanical Properties of Ceramics*, Cambridge University Press.

GRIFFITH, A.A. (1920), The phenomenon of rupture and flow in solids, *Phil. Trans. A*, Vol.221, pp.163-198.

GURTIN, M. (1981), *An Introduction to Continuum Mechanics*, Academic Press, San Diego.

HILL, R. (1950), *The Mathematical Theory of Plasticity*, Clarendon Press, Oxford.

HOAGLAND, R.G. and EMBURY, J.D. (1980), A treatment of inelastic deformation around a crack tip due to microcracking, *J. Am. Ceram. Soc.*, Vol.63, pp.404-410.

HOLZAPFEL, G.A. (2000), *Nonlinear Solid Mechanics*, Wiley, Chichester.

HUTCHINSON, J.W. (1987), Crack tip shielding by micro cracking in brittle solids, *Acta Metall.*, Vol.35, pp.1605-1619.

KINGERY, W.D., BOWEN, H.K. and UHLMANN, D.R. (1960), *Introduction to Ceramics*, (2nd edition), Wiley.

LAWN, B. (1993), *Fracture of Brittle Solids*, (2nd edition), Cambridge University Press.

LORET, B. and PREVOST, J.H. (1990), Dynamic strain localization in elasto-visco-plastic solids. Part I: General formulation and one-dimensional examples, *Comput. Meth. Appl. Mech. Engrg.*, Vol.83, pp.247-273.

LOVE, A.E.H. (1927), *A Treatise on The Mathematical Theory of Elasticity*, (4th edition), Cambridge University Press, Cambridge.

LUBLINER, J. (1998), *Plasticity Theory*, Prentice Hall.

MALVERN, L.E. (1969), *Introduction to the Mechanics of a Continuous Medium*, Prentice-Hall, Englewood Cliffs.

MCCLINTOCK, F.A. and ARGON, A.S. (1966), *Mechanical Behaviour of Materials*, Addison-Wesley, Reading.

MEYERS, M.A. and CHAWLA, K.K. (1999), *Mechanical Behaviour of Materials*, Prentice Hall.

MOVCHAN, A.B. and WILLIS, J.R. (1993), Asymptotic analysis of the reinforcement of a brittle crack by bridging fibres, *Quart. J. Mech. Appl. Math.*, Vol.46, pp.331-350.

MOVCHAN, N.V. and WILLIS, J.R. (1996), Critical load for a mode-1 crack reinforced by bridging fibres, *Quart. J. Mech. Appl. Math.*, Vol.49, pp.455-464.

MOVCHAN, N.V. and WILLIS, J.R. (1997a), Influence of spatial correlations on crack bridging by frictional fibres, *Eng. Fracture Mechanics*, Vol.58, pp.571-579.

MOVCHAN, N.V. and WILLIS, J.R. (1997b), Asymptotic analysis of reinforcement by frictional fibres, *Proc. R. Soc. Lond.*, Vol.453, pp.757-784.

MOVCHAN, N.V. and WILLIS, J.R. (1998), Penny-shaped crack bridging by fibres, *Quart. Appl. Math.*, Vol.LVI, pp.327-340.

MUNZ, D. and FETT, T. (1999), *Ceramics: Mechanical Properties, Failure Behaviour, Materials Selection*, Springer-Verlag, Berlin.

NADAI, A. (1950), *Theory of Flow and Fracture of Solids*, McGraw-Hill, New York.

OGDEN, R.W. (1984), *Non-linear Elastic Deformations*, Ellis Horwood, Chichester.

ORTIZ, M. (1988), Microcrack coalescence and macroscopic crack growth initiation in brittle solids, *Int. J. Solids Structures*, Vol.24, pp.231-250.

ORTIZ, M. and GIANNAKOPOULOS, A.E. (1989), Maximal crack tip shielding by microcracking, *J. Appl. Mech.*, Vol.56, pp.279-290.

PAMPUCH, R. (1991), *Constitution and Properties of Ceramic Materials*, PWN, Elsevier, Amsterdam.

PEZZOTTI, G. (1993), On the actual contribution of crack deflection in toughening platelet-reinforced brittle-matrix composites, *Acta Metall. Mater.*, Vol.41, pp.1825-1839.

PEZZOTTI, G., OKAMOTO, Y., NISHIDA, T. and SAKAI, M. (1996), On the near-tip toughening by crack-face bridging in particulate and platelet-reinforced ceramics, *Acta Mater.*, Vol.44, pp.899-914.

RICE, R.W. (1984), Pores as fracture origins in ceramics, *J. Mat. Sci.*, Vol.19, pp.895-914

ROSE, L.R.F. (1982), A cracked plate repaired by bonded reinforcements, *Int. J. Fracture*, Vol.18, pp.135-144.

ROSE, L.R.F. (1986), Microcrack interaction with a main crack, *Int. J. Fracture*, Vol.31, pp.233-242.

ROSE, L.R.F. (1987), Crack reinforcement by distributed springs, *J. Mech. Phys. Solids*, Vol.34, pp.383-405.

RUBINSTEIN, A.A. (1986), Macro-crack-micro-defect interaction, *J. Appl. Mech.*, Vol.53, pp.505-510.

SCOTT, L. (1954), Ceramics, in: *A History of Technology*, Singer, C., Holmyard, E.J., Hall, A.R. and Williams, T.I., (Eds.), Vol.I, Clarendon Press, Oxford.

SHACKELFORD, J.F. (1985), *Introduction to Materials Science for Engineers*, Macmillan Publishing Company, New York.

WESTERGAARD, H.M. (1939), Bearing pressures and cracks, *J. Appl. Mech.*, Vol.6, pp.49-53.

ZIMMERMANN, A., HOFFMAN, M., FLINN, B.D., BORDIA, R.K., CHUANG, T-.J., FULLER, E.R. and RÖDEL, J. (1998), Fracture of alumina with controlled pores, *J. Am. Ceram. Soc.*, Vol.81, pp.2449-2457.

ZIMMERMANN, A. and RÖDEL, J. (1998), Generalized Orowan-Petch plot for brittle fracture, *J. Am. Ceram. Soc.*, Vol.81, pp.2527-2532.

# On toughening in
# zirconia-containing ceramics

**Davide Bigoni** [1] **and Enrico Radi** [2]

*Transformation toughening in zirconia-containing ceramics is related to dilatational, inelastic volumetric strain. A model for steady-state, Mode I crack propagation in a pressure-sensitive, dilatational elastic-plastic material is presented, based on the Drucker-Prager yield criterion. In the framework of asymptotic analysis, results demonstrate a toughening effect related to pressure-sensitivity and volumetric inelastic strain. Asymptotic field representations may yield a deep understanding of near-crack tip stress-deformation phenomena.*

## 2.1. Introduction

Zirconia ($ZrO_2$) is often used in ceramic alloys as a toughening agent. In fact, zirconia ceramics exhibit a marked inelasticity and a relatively high

---

[1] Dipartimento di Ingegneria Meccanica e Strutturale, Università di Trento, Via Mesiano 77, 38050 Trento, Italy.

[2] Dipartimento di Scienze e Metodi dell'Ingegneria, Università di Modena e Reggio Emilia, Via Fogliani 1, 42100 Reggio Emilia, Italy.

fracture toughness, which make them suitable for different industrial applications, as for instance adiabatic engine components (Robb, 1983). The toughening effect is related to the martensitic phase transformation – accompanied with large shear (up to 16%, in an unconstrained crystal) and volumetric (up to 5%, in an unconstrained crystal) strains [3] – in which tetragonal zirconia transforms to monoclinic (t-$ZrO_2$ $\longrightarrow$ m-$ZrO_2$). More in detail, the tetragonal phase, usually found at high temperature, may be retained at low temperature, when the zirconia precipitate is sufficiently constrained by the surrounding material. This occurs when the zirconia particle is smaller than a critical size (which for instance is inferior to $0.5\,\mu$m, for a t-$ZrO_2$ particle to be retained at room temperature, Green, 1998). During fracture propagation, a stress-induced transformation has been experimentally demonstrated to occur near the crack tip (Evans and Heuer, 1980; Marshall et al. 1990; Dadkhah et al. 1991; Green et al. 1991). This gives rise to a nonlinear, irreversible [4] deformation which extends during propagation in the crack wake and yields a crack tip shielding effect (Evans, 1984; Evans and Cannon, 1986). In particular, though unstable fracture propagation would occur in the pure matrix material, stable crack growth has been observed – on the order of several millimetres – and $R$-curves have been measured in zirconia-containing ceramics (Stump and Budiansky, 1989).

There are different theoretical approaches to evaluate toughening associated with stress-induced phase transformation. Initial approaches have assumed a purely dilatational transformation strain, characterized by the macroscopic hydrostatic stress vs. dilatation strain shown in Fig. 2.1.

In particular, phase transformation initiates at a critical mean stress $\sigma_m^c$ (point 1) and proceeds until point 2. If the slope of the 1-2 line is steeper than a critical value, the transformation is unstable (supercritical case), otherwise it is stable (subcritical case) and the phase change occurs gradually, with the zirconia particles only partially transformed (for states represented by points between 1 and 2). Assuming the above model, McMeeking and Evans (1982), Budiansky et al. (1983), Lambropuolos (1986a,b), Rose (1986), Amazigo and

---

[3] Due to the constraint of the matrix phase on the zirconia precipitate, transformation occurs with extensive microcracking and shear strain is accomodated by twinning, thus resulting in an overall shear strain which may be remarkably less than 16%.

[4] The stress-induced transformation is usually considered irreversible, even if reversible transformations have been often observed (Marshall and James, 1986; Marshall and Swain, 1989).
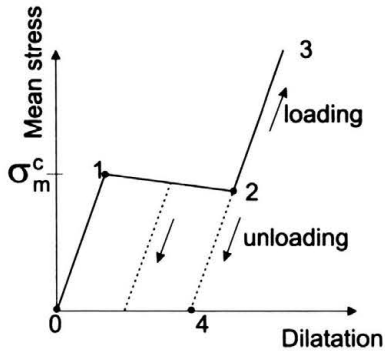
FIGURE 2.1. Hydrostatic behaviour of ceramics containing particles suffering a dilatational phase transformation.

Budiansky (1988), Stump and Budiansky (1989), and Hom and McMeeking (1990) performed various analyses at different levels of sophistication, both in the subcritical and supercritical ranges. The analyses essentially show that the shielding effect due to stress-induced phase transformation induces a rising in the $R$-curve, without changing the toughness when a stationary crack is present in an non-transformed material

In contrast with the purely dilatational behaviour, detailed experiments provided by Chen and Reyes-Morel (1986), Chen (1986) Reyes-Morel and Chen (1988), Reyes-Morel et al. (1988), and Subhash and Nemat-Nasser (1993) evidence a strong coupling between dilatational and shear strains, so that a model neglecting the latter should be considered merely approximated. The above-mentioned experiments also indicate the Drucker-Prager (1952) criterion as the best candidate for describing yielding of zirconia-containing ceramics. Moreover, calculations performed by Lambropoulos (1986b) reveals that the effect of shear transformation strain on the shape of the transformation zone may be very strong.

Therefore, a more fundamental approach has been followed by Stam et al. (1994) and Stam and van der Giessen (1995, 1996a,b), employing the model proposed by Sun et al. (1991) and Sun and Hwang (1993a,b). The numerical results presented confirm findings obtained with the simple dilatational model. Recent analyses based on the Sun model (Yi and Gao, 2000; Yi et al. 2001) again show a shielding effect related to stress-induced phase transformation. However, the Sun and Hwang model is sufficiently complicated to discourage analytical approaches to crack propagation analysis. Simpli-

fied plasticity models – retaining the key ingredients of plastic dilatancy and pressure-sensitive yielding – have been therefore employed to develop analytical solutions to crack growth near-tip fields. In particular, a stationary crack was analyzed for power-law (Li and Pan, 1990 a, b) and elastic-perfectly plastic (Li, 1992; Ben-Aoun and Pan, 1993) materials. However, according to the simplified analyses by McMeeking and Evans (1992) and Budiansky et al. (1993), the shielding effect related to phase transformation should become more evident in conditions of crack growth. Steady-state fracture propagation was considered by Amazigo and Hutchinson (1977), Ponte Castañeda (1987) and Bose and Ponte Castañeda (1992) for $J_2$-flow theory of plasticity. Their approach has been generalized to various pressure-sensitive models by Bigoni and Radi (1993, 1996), Radi and Bigoni (1993, 1994, 1996), Potthast and Hermann (1996, 1997, 2000) and Zhang and Mai (2000), Radi et al. (2001).

In particular, Bigoni and Radi (1993) and Radi and Bigoni (1993) have provided the first asymptotic solution for steady crack growth in a Drucker-Prager elastoplastic material with linear strain hardening under Mode I, plane strain and plane stress conditions, for associative and nonassociative flow rule. The results of Bigoni and Radi (1993) and Radi and Bigoni (1993) are concisely presented below in a way to give evidence to the connections with fracture behaviour in zirconia-containing ceramics.

## 2.2. Asymptotic crack-tip fields

The determination of asymptotic stress and strain fields in the plastic zone near a crack tip is a basic problem in the understanding of fracture propagation mechanisms. Our interest here is in asymptotic analyses, which give an accurate description of near tip fields. The validity of these is restricted to within an annular zone which – on one hand – is close enough to the crack tip to justify the dominance of certain terms in the asymptotic expansion of unknown tip fields, but – on the other hand – is greater than the fracture process zone, where microscopic separation processes occur (Hutchinson, 1983).

This is sketched in Fig. 2.2, where $r_1$ denotes the radius of the fracture process zone and $r_2$ sets a outer limit to the asymptotic analysis.

In the fracture propagation problem that is considered, the crack tip steadily and rectilinearly moves in an elastic-plastic material characterized
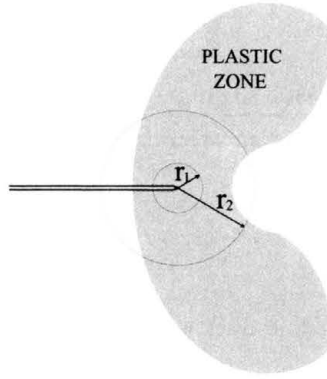
FIGURE 2.2. Validity limits of asymptotic analysis.

by the bi-linear constitutive law in shear shown in Fig. 2.3, where $\gamma$ is the engineering strain, $\tau$ the shear stress and $G$ and $G_t$ are the elastic and hardening shear moduli, respectively.
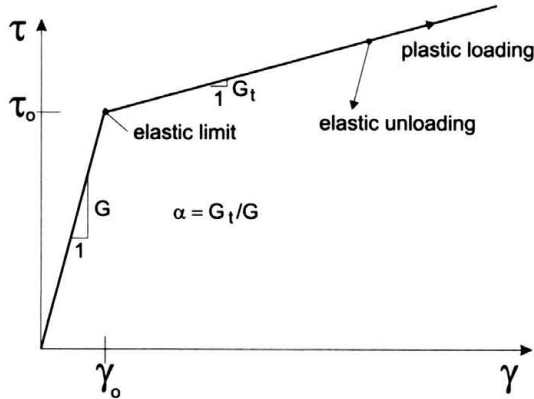


FIGURE 2.3. Shear stress $\tau$ vs. engineering strain $\gamma$ for the assumed model.

We refer to a fully incremental theory of plasticity, so that during crack propagation, elastic unloading and plastic reloading zones form, as schematically illustrated in Fig. 2.4.

Obviously, only the initial tangents to the plastic and elastic sectors are "viewed" in an asymptotic analysis, so that the analyzed situation looks like that sketched in Fig. 2.5, where $\theta_1$ and $\theta_2$ denote the angular coordinates of the elastic unloading and plastic reloading sectors, respectively.
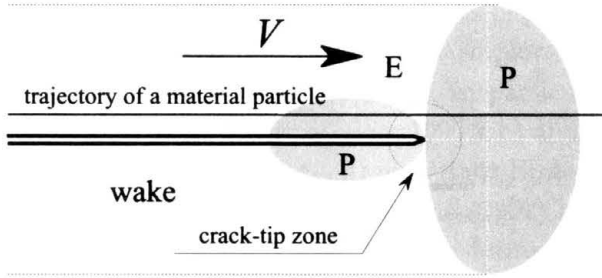
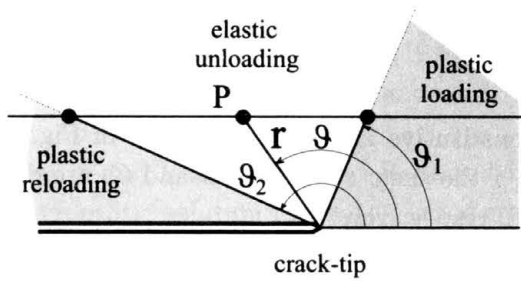FIGURE 2.4. Sketch of crack propagation in a plastic material.



FIGURE 2.5. Sketch of elastic unloading and plastic reloading sectors during crack propagation.

It may be important to remark that a plastic reloading sector must be necessarily present on crack flanks during crack propagation (Ponte Castañeda, 1987).

### 2.2.1. Constitutive equations

Small strain version of the Rudnicki and Rice (1975) model, with linear strain hardening is characterized by the following nonlinear incremental relationship between strain $\dot{\epsilon}$ and stress $\dot{\sigma}$ rates:

$$\dot{\epsilon} = \frac{1}{E}\left((1+\nu)\dot{\sigma} - \nu(\mathrm{tr}\dot{\sigma})\boldsymbol{I} + \frac{1}{h} < \boldsymbol{Q}\cdot\dot{\sigma} > \boldsymbol{P}\right), \quad \text{if } f(\sigma) = 0,$$

$$\dot{\epsilon} = \frac{1+\nu}{E}\dot{\sigma} - \frac{\nu}{E}(\mathrm{tr}\dot{\sigma})\boldsymbol{I}, \qquad\qquad \text{if } f(\sigma) < 0,$$

(2.1)

where $\nu$ is the Poisson's ratio, $E$ the Young modulus, $h$ the ratio between the hardening modulus and $E$, the operator $< \cdot >$ is the Macaulay brackets, and the yield function gradient $\boldsymbol{Q}$ and plastic mode $\boldsymbol{P}$ tensors are

$$Q = \frac{\mu}{3}I + \frac{S}{2\sqrt{J_2}}, \qquad P = \frac{\beta}{3}I + \frac{S}{2\sqrt{J_2}}, \qquad (2.2)$$

in which $J_2 = S \cdot S/2$ is the second invariant of deviatoric stress $S$ and $\mu$ and $\beta$ are two material parameters governing the pressure-sensitivity and the dilatancy of the material, respectively. Finally, $f(\sigma)$ is the Drucker-Prager yield function

$$f(\sigma) = \frac{\mu}{3}\text{tr}\sigma + \sqrt{J_2} - k, \qquad (2.3)$$

where $k$ is $1/\sqrt{2}$ time the radius of the deviatoric section of the yield surface with the $\pi$-plane in the Haigh-Westergaard stress space.

Even if the above-described constitutive model has been thoroughly employed in rock mechanics (where $\mu$ and $\beta$ may range between 0.4 and 1 and 0.2 and 0.5, respectively), there are only few experimental data for ceramics. In particular, Chen and Reyes-Morel (1986) and Reyes-Morel and Chen (1988) reported $\mu = \beta = 0.69$ for zirconia-containing ceramics. These experimental results support the validity of the associative flow rule, which is however usually violated for geomaterials. We will limit the presentation in the following to the Mode I plane-strain condition with associative flow rule, $\mu = \beta$.

### 2.2.2. Crack propagation

We refer to steady state crack propagation, so that, adopting a Cartesian reference system with origin attached to the moving crack tip (Fig. 2.6), the time derivative of a generic field may be replaced by the spatial derivative

$$(\dot{\ }) = -V(\ ),_1, \qquad (2.4)$$

where the axis 1 is in the direction of crack propagation and $V$ is the (constant) crack propagation velocity. In a cylindrical coordinate system, the equilibrium equations under plane-strain condition become
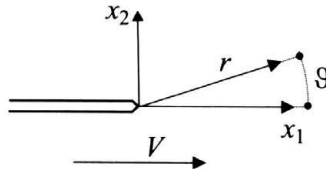


FIGURE 2.6. Moving crack and reference systems.

$$(r\sigma_{rr})_{,r} + \sigma_{r\theta,\theta} - \sigma_{\theta\theta} = 0,$$

$$(r\sigma_{r\theta})_{,r} + \sigma_{\theta\theta,\theta} + \sigma_{r\theta} = 0,$$

(2.5)

(where $\sigma_{rr}$, $\sigma_{r\theta}$ and $\sigma_{\theta\theta}$ are the three in-plane stress components) and the kinematical compatibility conditions

$$\dot{\epsilon}_{rr} = v_{r,r}, \quad \dot{\epsilon}_{\theta\theta} = \frac{v_{\theta,\theta} + v_r}{r}, \quad \dot{\epsilon}_{r\theta} = \frac{1}{2}\left(v_{\theta,r} + \frac{v_{r,\theta} - v_\theta}{r}\right), \quad \dot{\epsilon}_{33} = 0, \quad (2.6)$$

where $v_r$ and $v_\theta$ are the two in-plane components of velocity, $\epsilon_{rr}$, $\epsilon_{r\theta}$, $\epsilon_{\theta\theta}$ the three in-plane components of strain rate and the index 3 denotes out-of-plane components.

The steady-state condition (2.4) allows us to express the stress rates in terms of spatial derivatives with the following time derivative rule

$$\dot{\sigma}_{r\theta} = V\left(\frac{\sin\theta}{r}(\sigma_{rr} - \sigma_{\theta\theta} + \sigma_{r\theta,\theta}) - \sigma_{r\theta,r}\cos\theta\right),$$

$$\dot{\sigma}_{rr} = V\left(\frac{\sin\theta}{r}(\sigma_{rr,\theta} - 2\sigma_{r\theta}) - \sigma_{rr,r}\cos\theta\right),$$

$$\dot{\sigma}_{\theta\theta} = V\left(\frac{\sin\theta}{r}(\sigma_{\theta\theta,\theta} + 2\sigma_{r\theta}) - \sigma_{\theta\theta,r}\cos\theta\right),$$

$$\dot{\sigma}_{33} = V\left(\frac{\sin\theta}{r}\sigma_{33,\theta} - \sigma_{33,r}\cos\theta\right).$$

(2.7)

A substitution of Eqs. (2.6) and (2.7) into the constitutive equations (2.1) together with the equilibrium equations (2.5) yields a system of six PDEs for the six unknowns functions $v_r$, $v_\theta$ and $\sigma_{r\theta}$, $\sigma_{rr}$, $\sigma_{\theta\theta}$, $\sigma_{33}$. The key mathematical point is now to reduce the PDEs system to a system of ODEs, looking for solutions in the separable variable form proposed by Amazigo and Hutchinson (1977)

$$v_r = \frac{V}{s}\left(\frac{r}{B}\right)^s w_r(\theta), \qquad v_\theta = \frac{V}{s}\left(\frac{r}{B}\right)^s w_\theta(\theta),$$

$$\sigma_{r\theta} = E\left(\frac{r}{B}\right)^s T_{r\theta}(\theta), \qquad \sigma_{rr} = E\left(\frac{r}{B}\right)^s T_{rr}(\theta),$$

(2.8)

$$\sigma_{\theta\theta} = E\left(\frac{r}{B}\right)^s T_{\theta\theta}(\theta), \qquad \sigma_{33} = E\left(\frac{r}{B}\right)^s T_{33}(\theta),$$

where the negative exponent $s$ denotes the strength of stress and velocity singularity and $B$ denotes a characteristic dimension of the plastic zone.

Having assumed the representation (2.8), the angular functions $w_r$, $w_\theta$ and $T_{r\theta}$, $T_{rr}$, $T_{\theta\theta}$, $T_{33}$ and the field singularity $s$ become the unknowns of the problem [5]. These may be obtained through a Runge-Kutta numerical integration, combined with a shooting method to satisfy all boundary conditions. In the particular case of Mode I propagation, the boundary conditions are the following.

1. Mode I symmetry conditions (and regularity of angular functions)

$$w_\theta(0) = T_{r\theta}(0) = 0,$$
$$w_{r,\theta}(0) = T_{rr,\theta}(0) = T_{\theta\theta,\theta}(0) = T_{33,\theta}(0) = 0,$$

(2.9)

2. Boundary conditions on crack faces

$$T_{\theta\theta}(\pi) = T_{r\theta}(\pi) = 0,$$

(2.10)

3. Continuity across the elastic-plastic boundaries of all field quantities.

It is worth noting that possibility of elastic unloading and plastic reloading has to be checked and taken into account during numerical integration of the ODEs system.

## 2.3. Results

Extensive numerical investigations including plane-strain, plane-stress situations, effects of flow rule non-associativity, porosity, and fluid-saturation can be found in (Bigoni and Radi, 1993, 1996; Radi and Bigoni, 1993, 1994, 1996; Radi et al. 2001). Therefore, we limit the presentation here to the findings that may be relevant in the field of ceramic materials.

Values of the singularity $s$ and elastic unloading $\theta_1$ and plastic reloading $\theta_2$ angles as functions of the pressure-sensitivity parameter $\mu$ are reported in Figs. 2.7 and 2.8, respectively.

Small and high strain hardening are considered, corresponding to the values 0.001 and 0.75 of the hardening parameter $\alpha$ defined through

$$\frac{1}{\alpha} = 1 + \frac{1}{2(1+\nu)h}.$$

(2.11)

---

[5] The present asymptotic problem gives the leading term in the asymptotic expansion of crack tip fields. It is a homogeneous problem, so that the amplitude factor $B$ remains undetermined.
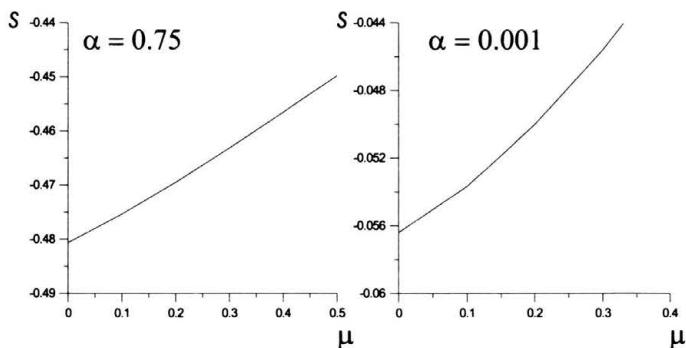
FIGURE 2.7. Singularity of stress and velocity fields $s$ as a function of pressure-sensitivity parameter $\mu$ for small ($\alpha = 0.001$) and high ($\alpha = 0.75$) strain hardening.
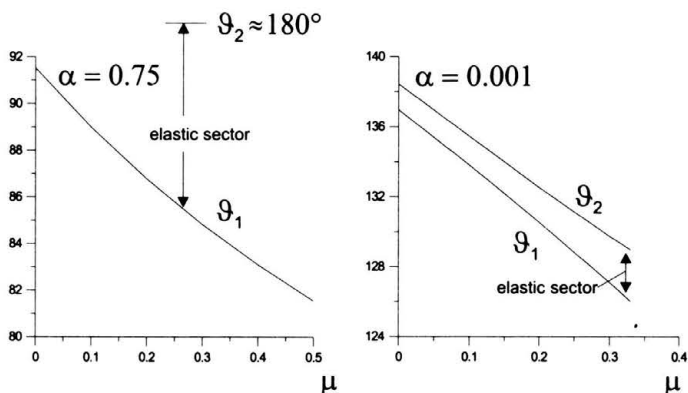


FIGURE 2.8. Elastic unloading $\theta_1$ and plastic reloading $\theta_2$ angles for small ($\alpha = 0.001$) and high ($\alpha = 0.75$) strain hardening.

It should be noted that the Poisson's ratio $\nu$ was found not influence much the results and has been chosen equal to 0.3. The angular function describing the stress and velocity components are reported in Fig. 2.9 and Fig. 2.10, respectively, where different values of pressure-sensitivity are considered for small hardening $\alpha = 0.001$.

Figures 2.7–2.10 are sufficient to draw the main conclusions of our study, namely, that an increase of the pressure-sensitivity and related dilatancy yields

- a reduction in the singularity of the stress and velocity fields;
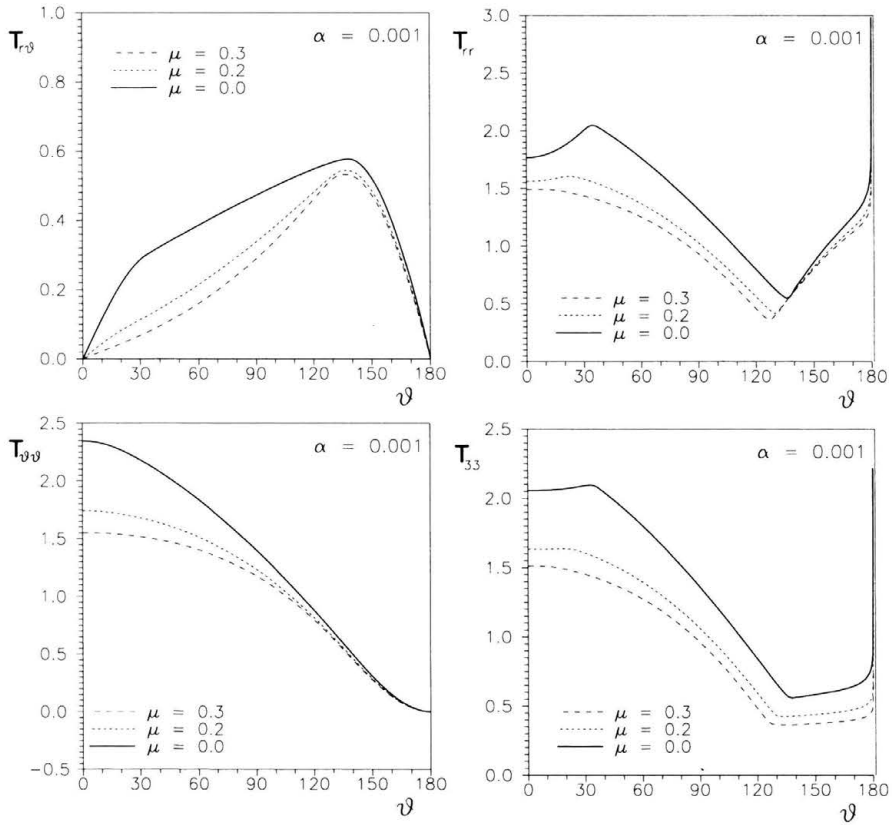- a decrease in the stress deviator ahead of the crack tip.

FIGURE 2.9.  Stress angular functions for different values of pressure-sensitivity $\mu$ at small strain hardening $\alpha = 0.001$.
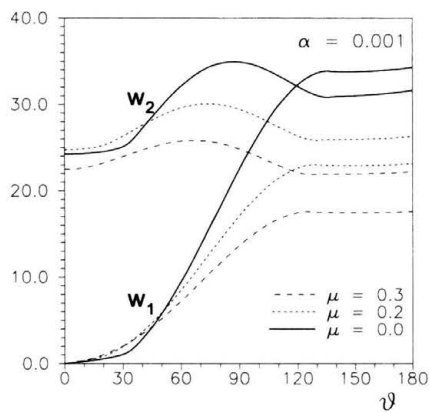


FIGURE 2.10.  Velocity angular functions for different values of pressure-sensitivity $\mu$ at small strain hardening $\alpha = 0.001$.

The above two facts imply *a crack growth stabilization connected to an increase of pressure-sensitivity and related plastic dilatancy*. This conclusion is therefore consistent with the well-known fact that the dilatancy associated with stress-induced phase transformation is directly related to the shielding effect. An analysis based on nonassociative flow rule – where plastic dilatancy is unrelated to pressure-sensitive yielding ($\mu \neq \beta$) – shows that *for a fixed pressure-sensitivity, plastic dilatancy is the key constitutive feature controlling crack stabilization* (Radi and Bigoni, 1993).

## 2.4. Conclusions

We have presented a simple model for steady-state, Mode I crack propagation in transformation-toughened ceramics. Though based on linear hardening (of the type shown in Fig. 2.3, instead of the more elaborate constitutive law sketched in Fig. 2.1), the model retains a number of features typical of behaviour of zirconia-containing ceramics. These are:

- nonlinear, inelastic deformation,
- pressure-sensitive yielding,
- inelastic dilatancy,
- coupling between shear and dilatant inelastic deformation.

Moreover, the model is simple enough to permit an asymptotic analysis of all relevant fields, including full treatment of loading/unloading conditions in the crack wake. If, on one hand, the analysis yields the known result that plastic dilatancy and pressure-sensitive yielding induce a crack stabilization effect, on the other hand, a detailed representation of near tip fields, possible with our analytical approach, may become important for design purposes.

In conclusion, we note that the approach presented in this Chapter has been extended to rather complicated situations. For instance, Radi and Bigoni (1995, 1996) analyzed isotropic and anisotropic hardening for Gurson yielding; Radi et al. (2001) included fluid saturation; Potthast and Hermann (1996, 1997, 2000) and Zhang and Mai (2000) considered dynamic and temperature effects. It may be therefore reasonable to think that the asymptotic scheme presented in the present Chapter could be further refined for material modelling of zirconia-containing ceramics.

## 2.5. References

AMAZIGO, J.C. and BUDIANSKY, B. (1988), Steady-state crack growth in super-critically transforming materials, *Int. J. Solids Structures*, Vol.24, pp.751-755.

AMAZIGO, J.C. and HUTCHINSON, J.W. (1977), Crack-tip fields in steady crack-growth with linear strain hardening, *J. Mech. Phys. Solids*, Vol.25, pp.81-97.

BEN-AOUN Z.E. and PAN, J. (1993), Effects of elasticity and pressure-sensitive yielding on plane-stress crack-tip fields, *Engng. Fracture Mech.*, Vol.44, pp.649-661.

BIGONI, D. and RADI, E. (1993), Mode I crack propagation in elastic-plastic pressure-sensitive materials, *Int. J. Solids Structures*, Vol.30, pp.899-919.

BIGONI, D. and RADI, E. (1996), Asymptotic solution for Mode III crack growth in $J_2$-elastoplasticity with mixed isotropic-kinematic strain hardening, *Int. J. Fracture*, Vol.77, pp.77-93.

BOSE, K. and PONTE CASTAÑEDA, P. (1992), Stable crack-growth under mixed-mode conditions, *J. Mech. Phys. Solids*, Vol.40, pp.1053-1103.

BUDIANSKY, B., HUTCHINSON, J.W. and LAMBROPOULUS, J.C. (1983), Continuum theory of dilatant transformation toughening in ceramics, *Int. J. Solids Structures*, Vol.19, pp.337-355.

CHEN, I-W. (1986), Implications of transformation plasticity in $ZrO_2$-containing ceramics: II, elastic-plastic indentation, *J. Am. Ceram Soc.*, Vol.69, pp.189-194.

CHEN, I-W. and REYES MOREL, P.E. (1986), Implications of transformation plasticity in $ZrO_2$-containing ceramics: I, shear and dilatation effects, *J. Am. Ceram Soc.*, Vol.69, pp.181-189.

DADKHAH, M.S., MARSHALL, D.B., MORRIS, W.L. and COX, B.N. (1991), Direct measurement of transformation zone strains in toughened zirconia, *J. Am. Ceram. Soc.*, Vol.74, pp.584-592.

DRUCKER, D.C. and PRAGER, W. (1952), Soil mechanics and plastic analysis or limit design, *Quart. Appl. Math.*, Vol.10, pp.157-165.

EVANS, A.G. (1984), Toughening mechanisms in zirconia alloys, in: *Fracture in Ceramic Materials*, Evans, A.G., (Ed.), Noyes Publications, Park Ridge, NJ, pp.16-55.

EVANS, A.G. and CANNON R.M. (1986), Toughening of brittle solids by martensitic transformations, *Acta Metall.*, Vol.34, pp.761-800.

EVANS, A.G. and HEUER, A.H. (1980), Transformation toughening in ceramics: martensitic transformations in crack tip stress fields, *J. Am. Ceram. Soc.*, Vol.63, pp.241-248.

GREEN, D.J. (1998), *An Introduction to the Mechanical Properties of Ceramics*, Cambridge University Press.

GREEN, D.J. HANNINK, R.H.J. and SWAIN, M.V. (1991), *Transformation Toughening in Ceramics*, CRC Press, Boca Raton, Fl., USA.

HOM, C.L. and MCMEEKING, R.M. (1990), Numerical results for transformation toughening in ceramics, *Int. J. Solids Structures*, Vol.26, pp.1211-1223.

HUTCHINSON, J.W. (1983), Fundamentals of the phenomenological theory of nonlinear fracture mechanics, *J. Appl. Mech.*, Vol.50, pp.1042-1051.

LAMBROPOULOS, J.C. (1986a), Effects of nucleation on transformation toughening, *J. Am. Ceram. Soc.*, Vol.69, pp.218-222.

LAMBROPOULOS, J.C. (1986b), Shear, shape and orientation effects in transformation toughening, *Int. J. Solids Structures*, Vol.22, pp.1083-1106.

LI, F.Z. (1992), The analytical solution of near-tip stress fields for perfectly plastic pressure-sensitive material under plane stress condition, *Int. J. Fracture*, Vol.53, pp.325-336.

LI, F.Z. and PAN, J. (1990a), Plane-stress crack-tip fields for pressure-sensitive dilatant materials, *Engng. Fracture Mech.*, Vol.35, pp.1105-1116.

LI, F.Z. and PAN, J. (1990b), Plane-strain crack-tip fields for pressure-sensitive dilatant materials, *J. Appl. Mech.*, Vol.57, pp.40-49.

MARSHALL, D.B. and JAMES, M.R. (1986), Reversible stress-induced martensitic transformation in ZrO, *J. Am. Ceram. Soc.*, Vol.69, pp.215-217.

MARSHALL, D.B., SHAW, M.C., DAUSKARDT, R.H., RITCHIE, R.O. READEY, M.J. and HEUER, A.H. (1990), Crack-tip transformation zones in toughened zirconia, *J. Am. Ceram. Soc.*, Vol.73, pp.2659-2666.

MARSHALL, D.B. and SWAIN, M.V. (1989), Reversible transformation and elastic anisotropy in Mg-ZrO, *J. Am. Ceram. Soc.*, Vol.72, pp.1530-1532.

MCMEEKING, R.M. and EVANS, A.G. (1982), Mechanics of transformation-toughening in brittle materials, *J. Am. Ceram Soc.*, Vol.65, pp.242-246.

PONTE CASTAÑEDA, P. (1987), Asymptotic fields in steady crack growth with linear strain-hardening, *J. Mech. Phys. Solids*, Vol.35, pp.227-268.

POTTHAST, B. and HERRMANN, K.P. (1996), Asymptotic crack tip fields for pressure-sensitive materials and dynamic crack growth under plane stress conditions, *Int. J. Fracture*, Vol.74, pp.R53-R61.

POTTHAST, B. and HERRMANN, K.P. (1997), Calculation of the asymptotic temperature field induced by dynamic crack growth in elastic-plastic materials, *Z. Angew. Math. Mech.*, Vol.77, pp.S271-S272.

POTTHAST, B. and HERRMANN, K.P. (2000), Asymptotic analysis for temperature fields induced by dynamic crack growth in pressure-sensitive materials, *Int. J. Fracture*, Vol.106, pp.57-64.

RADI, E. and BIGONI, D. (1993), Asymptotic fields of mode I steady-state crack propagation in non-associative elastoplastic solids, *Mech. Materials*, Vol.14, pp.239-251.

RADI, E. and BIGONI, D. (1994), Crack propagation in porous hardening metals, *Int. J. Plasticity*, Vol.10, pp.761-793.

RADI, E. and BIGONI, D. (1996), Effects of anisotropic hardening on crack propagation in porous-ductile materials, *J. Mech. Phys. Solids*, Vol.44, pp.1475-1508.

RADI, E., BIGONI, D. and LORET, B. (2001), Steady crack growth in elastic-plastic fluid-saturated porous media, *Int. J. Plasticity*, in press.

REYES MOREL, P.E. and CHEN, I-W. (1988), Transformation plasticity of $CeO_2$-stabilized tetragonal zirconia polycrystals: I, stress assistance and autocatalysis, *J. Am. Ceram Soc.*, Vol.71, pp.343-353.

REYES MOREL, P.E., CHERNG, J-S. and CHEN, I-W. (1988), Transformation plasticity of $CeO_2$-stabilized tetragonal zirconia polycrystals: II, pseudoelasticity and shape memory effect, *J. Am. Ceram. Soc.*, Vol.71, pp.648-657.

ROBB, S. (1983), Cummins successfully tests adiabatic engine, *Am. Ceram. Soc. Bull.*, Vol.62, pp.755-756.

ROSE, L.R.F. (1986), The size of the transformed zone during steady-state cracking in transformation toughened materials, *J. Mech. Phys. Solids*, Vol.34, pp.609-616.

RUDNICKI, J.W. and RICE, J.R. (1975), Conditions for the localization of deformations in pressure-sensitive dilatant materials, *J. Mech. Phys. Solids*, Vol.23, pp.371-394.

STAM, G. and VAN DER GIESSEN, E. (1995), Effect of reversible phase transformations on crack growth, *Mech. Materials*, Vol.21, pp.51-71.

STAM, G. and VAN DER GIESSEN, E. (1996a), Crack growth in non-homogeneous transformable ceramics. Part I: Constrained straight cracks, *Int. J. Fracture*, Vol.79, pp.249-271.

STAM, G. and VAN DER GIESSEN, E. (1996b), Crack growth in non-homogeneous transformable ceramics. Part II: Crack deflection, *Int. J. Fracture*, Vol.79, pp.273-293.

STAM, G.T.M., VAN DER GIESSEN, E. and MEIJERS, P. (1994), Effect of transformation-induced shear strains on crack growth in zirconia-containing ceramics, *Int. J. Solids Structures*, Vol.31, pp.1923-1948.

STUMP, D.M. and BUDIANSKY B. (1989), Crack-growth resistance in transformation toughened ceramics, *Int. J. Solids Structures*, Vol.25, pp.635-646.

SUBHASH, G. and NEMAT-NASSER, S. (1993), Dynamic stress-induced transformation and texture formation in uniaxial compression of zirconia ceramics, *J. Am. Ceram. Soc.*, Vol.76, pp.153-165.

SUN, Q.P. and HWANG, K.C. (1993a), Micromechanics modeling for the constitutive behavior of polycrystalline shape memory alloys. 1. Derivation of general relations, *J. Mech. Phys. Solids*, Vol.41, pp.1-17.

SUN, Q.P. and HWANG, K.C. (1993b), Micromechanics modeling for the constitutive behavior of polycrystalline shape memory alloys. 2. Study of the individual phenomena, *J. Mech. Phys. Solids*, Vol.41, pp.19-33.

SUN, Q.P., HWANG, K.C. and YU, S.W. (1991), A micromechanics constitutive model of transformation plasticity with shear and dilatation effect, *J. Mech. Phys. Solids*, Vol.39, pp.507-524.

YI, S. and GAO, S. (2000), Fracture toughening mechanism of shape memory alloys due to martensite transformation, *Int. J. Solids Structures*, Vol.37, pp.5315-5327.

YI, S., GAO, S. and SHEN. L.X. (2001), Fracture toughening mechanism of shape memory alloys under mixed-mode loading due to martensite transformation, *Int. J. Solids Structures*, Vol.38, pp.4463-4476.

ZHANG, X. and MAI, Y.W. (2000), Asymptotic fields for dynamic crack growth in pressure-sensitive elastic-plastic materials, *Int. J. Solids Structures*, Vol.37, pp.6297-6319.

Chapter **3**

# Crack deflection in ceramic materials

**Monica Valentini** [1], **Davide Bigoni** [1],
**Leonardo Esposito** [2], **Alexander B. Movchan** [3]
**and Sergey K. Serkov** [4]

*Predictions of a mathematical model developed for analyzing deviations from rectilinearity of a crack in brittle elastic materials containing a dilute distribution of voids and elastic inclusions are compared with experimental results relative to some ceramic materials: a glaze, a porcelain stoneware, and a zirconia. All these materials contain spheroidal pores. The investigation involves simple experimental setting, namely crack deflection of median-radial cracks induced by Vickers indentation. This is finally compared to the predictions of the analytical model. Despite of the strong hypotheses (plane deformations and small ratio between inclusion diameter and crack distance) the simulation results are qualitatively accurate. Under these assumptions one can obtain analytical solu-*

[1] Dipartimento di Ingegneria Meccanica e Strutturale, Università di Trento, Via Mesiano 77, 38050 Trento, Italy.

[2] Italian Ceramic Center, via Martelli 26, 40138 Bologna, Italy.

[3] Department of Mathematical Sciences, University of Liverpool, Liverpool L69 3BX, U.K.

[4] Department of Mathematics, University of Utah, Salt Lake City, UT 84112 USA.

*tions. This may suggest the use of the analytical model as a tool for the design of ceramic porous or composite materials.*


## 3.1. Introduction

Analysis of crack propagation and failure in ceramic materials is a basic problem with implications on many design aspects. Structural and traditional ceramics are usually brittle materials and the presence of porosity or second phases strongly influences fracture mechanisms. In particular, crack trajectories may be perturbed and deflected from rectilinearity by grains (Bower and Ortiz, 1993), defects, pores, inclusions, particles (Xu et al. 1997). Though with proper reserves (see Pezzotti, 1993; Pezzotti et al. 1996), deflection of crack trajectory may be related to material toughness (Evans, 1990); therefore, an analysis of the perturbation of a crack path due to the interaction with voids and inclusions may have practical applications in the design of composite ceramics. Motivated by this interest, a certain experimental and theoretical research effort has been addressed to the mechanics of cracks in elastic media containing defects, cracks or inclusions (Claussen, 1976; Cotterel and Rice, 1980; Hoagland and Embury, 1980; Faber and Evans, 1983; Clarke, 1984; Fu and Evans, 1985; Evans and Fu, 1985; Rubinstein, 1986; Rose, 1986; Hutchinson, 1987; Ortiz, 1988; Ortiz and Giannakopoulos, 1989; Duan et al. 1995) Moreover, in a series of papers, Movchan and co-workers (Movchan et al. 1992; Movchan, 1992; Movchan and Movchan, 1995) have developed an asymptotic model for the interaction of a semi-infinite crack and small defects. In the model, the defect is characterized on the basis of the Pòlya Szegö (1951) matrix. Defects modelled as elliptic elastic inclusions and voids have been considered in (Bigoni et al. 1998; Valentini et al. 1999). The solution for the crack trajectory is obtained by introducing a number of simplifying hypotheses, which make the problem solvable in analytical, closed-form. These assumptions are:

- plane strain (or stress),
- isotropic elasticity,
- small ratio between inclusion diameter and distance of the inclusion centre to the crack trajectory,
- crack of semi-infinite length,
- non-interaction between defects,

- use of the pure mode I ($K_{II} = 0$) fracture propagation criterion (Sih, 1974), an assumption which may be motivated invoking the brittleness of the matrix material.

In the present article the possibility of an application of the above analytical model is explored to predict crack paths in some ceramic materials. A well-known alternative to our method is the use of a numerical technique, e.g. finite elements. Numerical results are often problematic in situations involving singularities (as in the present case) and may be unpractical for design purposes. Therefore, a closed-form, analytical model becomes particular appealing. We restrict the attention to the simplest experimental setting, considering ceramic materials with spheroidal pores and inducing fractures with a Vickers indenter. In particular, on the surface of suitably prepared samples of zirconia, porcelain stoneware, and glaze, cracks were induced by Vickers indentation technique. The trajectories resulting from propagation of the median-radial cracks emerging from the corners of the impression have been observed. These are found to be influenced – generally attracted – by the voids. The experiments have been finally compared to the predictions of the analytical model for crack propagation as influenced by the presence of ellipsoidal voids. The applicability of the theory to the experiments is conditioned by the above-mentioned assumptions. Despite that, we have already verified a surprisingly good qualitative adherence of simulated to real crack trajectories in a few experiments on a porcelain stoneware (Valentini et al. 1999). The more systematic results reported in this chapter are also encouraging, and suggest the possibility of using the analytical tool in design situations relative to not fully densified or composite ceramics.

## 3.2. Mathematical model

To make the chapter self-contained, the model for the analysis of crack trajectory as influenced by elliptical defects is briefly described in this section (for a detailed presentation, the interested reader is referred to Movchan et al. 1992; Movchan, 1992; Movchan and Movchan, 1995; Valentini et al. 1999; Bigoni et al. 1998).

We consider an infinite, brittle-elastic body with a semi-infinite crack. The elastic properties are specified by the Lamé constants $\lambda$ and $\mu$. The crack is assumed to be a Mode-I crack propagating through the body under an external loading corresponding to a stress intensity factor $K_I$ greater than

the critical one. An elastic defect with Lamé constants $\lambda_0$ and $\mu_0$ is present in the infinite elastic medium in such a way that it is far from the trajectory of unperturbed (reference) crack (Fig. 3.1).
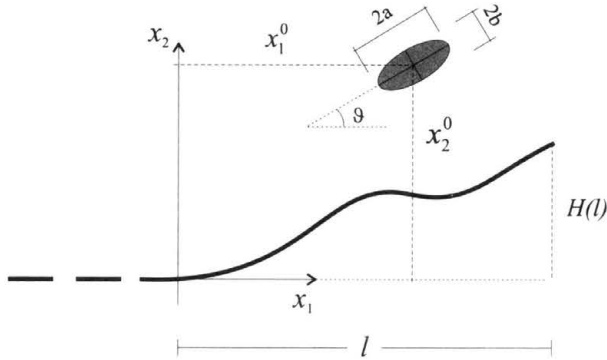


FIGURE 3.1. Sketch of the analyzed crack geometry.

This is the straight trajectory that would be described in the absence of defects. The defect has the shape of an ellipse centered at the point $(x_1^0, x_2^0)$ with major and minor semi-axes denoted by $a$ and $b$, respectively. The major axis is inclined of an angle $\theta$ with respect to the $x_1$-axis of the Cartesian plane. Due to the presence of the defect, the crack trajectory deviates from rectilinearity and this perturbation can be summarized in the closed-form formula for the crack trajectory $H(l)$ as a function of the crack tip abscissa $l$ (the details of the derivation are given by Valentini et al. 1999):

$$
\begin{aligned}
H(l) = \frac{ab}{4x_2^0}\bigg\{ &\Upsilon(\rho^4 - \Theta)(t + t^2 - 2) \\
&+ 2\rho^2\Upsilon\Theta\Big[\sin 2\theta(t+t^2)(2t-1)\sqrt{1-t^2} - \cos 2\theta(t-t^3)(1+2t)\Big] \\
&+ \frac{\Theta\rho^4}{\rho^4 + \Theta}(t-t^3)\Big[\left(1 + \Xi\cos^2 2\theta\right)(1-t)(1+2t)^2 \\
&+ \left(1 + \Xi\sin^2 2\theta\right)(1+t)(2t-1)^2 - \Xi\sin 4\theta\sqrt{1-t^2}(4t^2-1)\Big]\bigg\},
\end{aligned}
\tag{3.1}
$$

where the variable $t$ depends on $l$ through the relation

$$
t = \frac{x_1^0 - l}{\sqrt{\left(x_2^0\right)^2 + \left(x_1^0 - l\right)^2}}, \quad \text{and} \quad \rho = \sqrt{\frac{a+b}{a-b}}.
\tag{3.2}
$$

The elastic properties of the inclusion and matrix influence the crack trajectory via the constants:

$$\Theta = \frac{\mu_0 - \mu}{\kappa\mu_0 + \mu},$$

$$\Xi = \frac{2\Theta(\kappa + 1)\mu_0}{\rho^4[(\kappa_0 - 1)\mu + 2\mu_0] + \Theta[(\kappa_0 - 1)\mu - 2\kappa\mu_0]}, \quad (3.3)$$

$$\Upsilon = \frac{2[(\kappa - 1)\mu_0 - (\kappa_0 - 1)\mu]}{\rho^4[(\kappa_0 - 1)\mu + 2\mu_0] + \Theta[(\kappa_0 - 1)\mu - 2\kappa\mu_0]},$$

where, for plain strain, $\kappa = (\lambda + 3\mu)/(\lambda + \mu)$. The crack trajectory $H(l)$ and the position of the centre of the ellipse are given in an orthogonal co-ordinate system with the axis $x_1$ corresponding to the unperturbed crack trajectory, i.e. the straight trajectory representing the crack path in the absence of any defect.

The analysis of the formula for crack propagation leads to the interesting observation that the elastic properties of the materials affect the crack trajectory via Dundurs constants (Dundurs, 1967):

$$\alpha_{12} = \frac{\mu_0(\kappa + 1) - \mu(\kappa_0 + 1)}{\mu_0(\kappa + 1) + \mu(\kappa_0 + 1)}, \qquad \beta_{12} = \frac{\mu_0(\kappa - 1) - \mu(\kappa_0 - 1)}{\mu_0(\kappa + 1) + \mu(\kappa_0 + 1)}. \quad (3.4)$$

These dimensionless elastic invariants play an important role in the theory of elastic composites (Thorpe and Jasiuk, 1992). In fact, the stress field in two-dimensional, two-phase elastic composites depends on these two parameters only, rather than on the four elastic constants (shear and bulk moduli of both phases).

In our model, the constants (3.3) can be rewritten in terms of Dundurs invariants:

$$\Theta = \frac{\alpha_{12} - \beta_{12}}{\beta_{12} + 1}, \qquad \Omega = \frac{2\beta_{12}}{\alpha_{12} + 1},$$

$$\Xi = \frac{2\Theta}{\rho^4(1 - \Omega) - \Theta(1 + \Omega)}, \quad (3.5)$$

$$\Upsilon = \frac{2}{\rho^4(\Omega^{-1} - 1) - \Theta(\Omega^{-1} + 1)}.$$

In particular, it can be concluded from (3.5) that the crack trajectories belong to a two-parametric family of curves.

In the case where the inclusion is a void, the formula for the crack trajectory may be obtained taking $\mu_0 = \lambda_0 = 0$ in (3.1)-(3.3):

$$H(l) = \frac{R^2}{2x_2^0} \left[ 2(1 + m^2) - t\left(2 + t - t^2 + m^2(1 + t)\right) \right.$$

$$\left. + 2m \cos 2\theta (1 + 2t)(1 - t^2) - 2m \sin 2\theta (2t - 1)(1 + t)\sqrt{1 - t^2}\right)\right], \quad (3.6)$$

where

$$R = \frac{a + b}{2} \quad \text{and} \quad m = \frac{a - b}{a + b}.$$

Note that formula (3.6) is independent of the mechanical characteristics of the material and depends only on the morphology of the void, namely, inclination of the major axis, dimension and aspect ratio of the ellipse, i.e. parameters $\theta$, $R$ and $m$. This may be viewed as a corollary of the statement that the crack trajectory (3.1) depends on Dundurs constants and defects morphology only. The constants (3.4) and (3.5) for an elliptical void reduce to the simple expressions:

$$\alpha_{12} = -1, \qquad \beta_{12} = \frac{1 - \kappa_0}{1 + \kappa_0} \leq 0, \qquad \Theta = -1,$$

$$\Omega \to -\infty, \qquad \Xi = 0, \qquad \Upsilon = \frac{2}{1 - \rho^4}.$$

It may be interesting to note that imperfectly bonded circular inclusions have been considered in (Bigoni et al. 1998).

## 3.3. Experimental results

### 3.3.1. Materials

In order to check the expectations of the mathematical model, the following materials have been selected:

- a slip cast yttria tetragonal zirconia polycrystal TZP (TZ-3YS, Tosoh Co. Japan), preparation reported elsewhere (Salomoni et al. 1992),
- a porcelain stoneware,
- some glaze tiles.

The choice of the commercial traditional ceramics has been suggested by the possibility of exploiting their high intrinsic porosity. In fact, as a consequence of the industrial processing, pores with spheroidal geometry are usually present in the microstructure of the porcelain stoneware, when containing a large amount of glassy phase. In the glaze tiles, on the other hand,

pores of spheroidal geometry are usually trapped in the glaze layer, and often emerge on the proper surface.

Samples of TZP and porcelain stoneware were polished to mirror like, to perform a clear surface analysis. Samples of TZP were preliminary observed with SEM (Jeol, T330, Japan) to detect surface defects, for subsequent investigation of crack interaction. A selection of suitable samples of glazed ceramic tiles with porosity emerging on the proper surface was made on the basis of preliminary SEM observations. In this material, quasi-spherical pores were found on the proper surface with an average diameter ranging between 5 and 20 $\mu$m. These samples did not require any preliminary surface preparation.

### 3.3.2. Experiments

On the surface of the samples cracks were induced by Vickers indentation technique, applying indentation loads ranging between 19.62 and 49.05 N. The resulting crack paths have been finally observed both with optical and scanning electron microscopes. Note that for TZP samples Vickers indentations were induced near already detected surface defects, whereas, due to the high intrinsic porosity, indentations were induced in random positions for porcelain stoneware and glaze and subsequently observed.

For all investigated materials, a particular care was taken to the generation and development of median-radial cracks, arising from corners of the impression. Not always, in fact, the crack systems were suitable to verify the expectations of the model. For instance, sometimes the median-radial cracks were intercepted and stopped by a pore. In other cases at high indentation loads, material removal phenomena – consequent to induced lateral cracks – prevented any clear and correct observation of crack trajectory. On the other hand, indentation loads lower than 19.62 N may not even be sufficient to induce well developed median-radial cracks for fracture toughness determination (Marshall and Lawn, 1977). The experimental procedure was found particularly delicate in the case of porcelain stoneware, and was abandoned after few experiments were performed (the most representative of these are reported by Valentini et al. 1992, Bigoni et al. 1996, and Valentini, 1998). Other experiments were attempted in a zirconia/alumina composite and in a borosilicate glass containing copper platelets (Valentini, 1998). These materials did not fit correctly the model hypotheses and therefore results are not reported here.

### 3.3.3. Model prediction

In the following, the micrographs of the most representative experiments are shown, together with the corresponding simulations obtained from the analytical model, formula (3.6). The formula is used with a direct estimation of the needed geometrical parameters, namely, dimensions, orientation, shape, and relative position of the defects. Note that the use of formula (3.6) – relative to ellipsoidal voids in an elastic matrix – does not require any consideration of the mechanical characteristics of the material. Moreover, the simulations have a qualitative meaning, therefore all measures have been referred to a grid of points in an arbitrary length units, in the sense that only
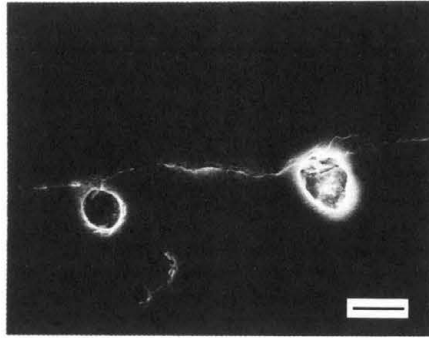


FIGURE 3.2.  Crack path near two circular voids in glaze: SEM micrograph
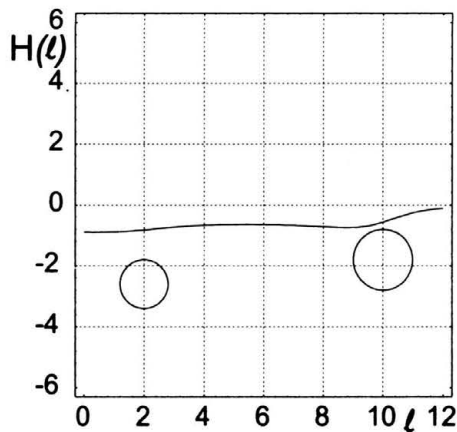(bar $= 10\,\mu$m).



FIGURE 3.3.  Crack path near two circular voids in glaze: simulation of the crack path.

Let us analyze the results in detail. Two circular voids of different dimensions present in a glaze sample are shown to attract a crack in Fig. 3.2. The corresponding model prediction is shown in Fig. 3.3.

Figure 3.4 is obtained with an optical microscope on a glaze sample. It may be observed that the crack trajectory starts from the indentation on the left side of the photograph, and is initially attracted by the void of small size and subsequently by the second, larger void. The simulation is presented in Fig. 3.5.

A crack interacting with three voids in a glaze sample is shown in Fig. 3.6. Two of the voids are approximately circular an the third has an elliptical form
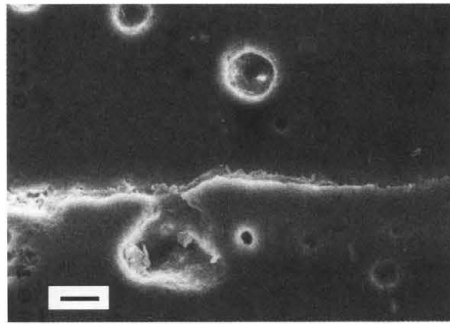


FIGURE 3.6.  Crack interacting with two circular and an elliptical void in glaze: SEM micrograph (bar $= 8.3\,\mu$m).
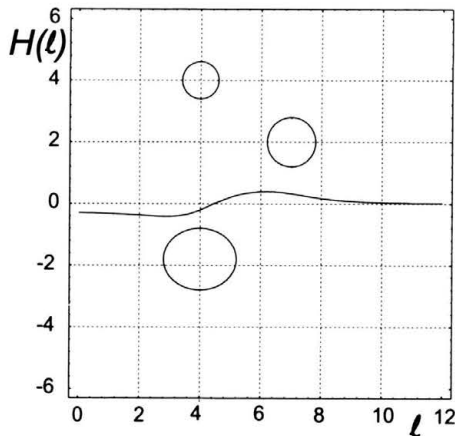


FIGURE 3.7.  Crack interacting with an elliptical and two circular voids in glaze: simulation of the crack path.

Let us analyze the results in detail. Two circular voids of different dimensions present in a glaze sample are shown to attract a crack in Fig. 3.2. The corresponding model prediction is shown in Fig. 3.3.

Figure 3.4 is obtained with an optical microscope on a glaze sample. It may be observed that the crack trajectory starts from the indentation on the left side of the photograph, and is initially attracted by the void of small size and subsequently by the second, larger void. The simulation is presented in Fig. 3.5.

A crack interacting with three voids in a glaze sample is shown in Fig. 3.6. Two of the voids are approximately circular an the third has an elliptical form
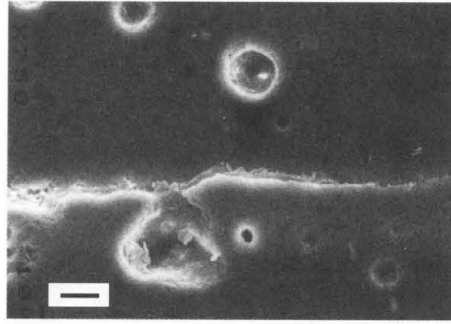


FIGURE 3.6. Crack interacting with two circular and an elliptical void in glaze: SEM micrograph (bar = 8.3 $\mu$m).
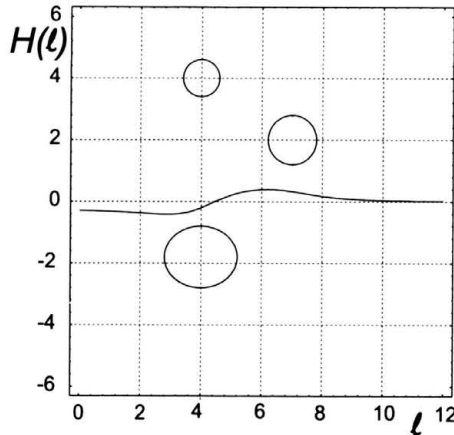


FIGURE 3.7. Crack interacting with an elliptical and two circular voids in glaze: simulation of the crack path.

(voids of smaller dimensions have been neglected in the simulation). The crack trajectory is deflected initially by the elliptical void and subsequently by the void closest to the crack path. The analytical result gives the prediction shown in Fig. 3.7.

Figure 3.8 is relative to a crack propagated in a glaze sample containing a number of voids having different dimensions. It is possible to compare the situation shown in Fig. 3.8 with the simplified geometry proposed in Fig. 3.9.

It may be observed in Fig. 3.10 that in a nearly symmetric distribution of defects the effects of each void tend to be compensated for the others. The
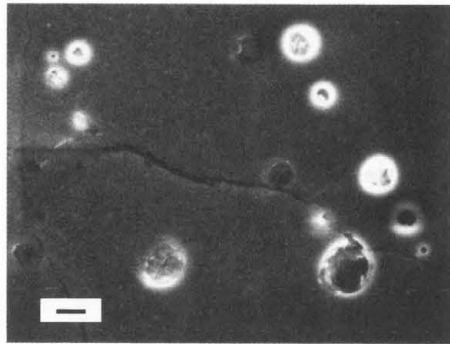


FIGURE 3.8. Crack interacting with several voids in glaze: SEM micrograph (bar $= 12.5\,\mu$m).
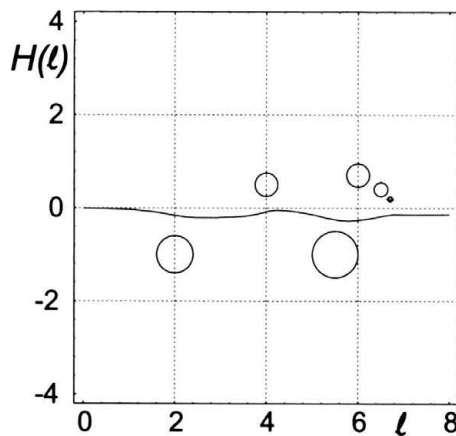


FIGURE 3.9. Crack interacting with several voids in glaze: simulation of the crack path.
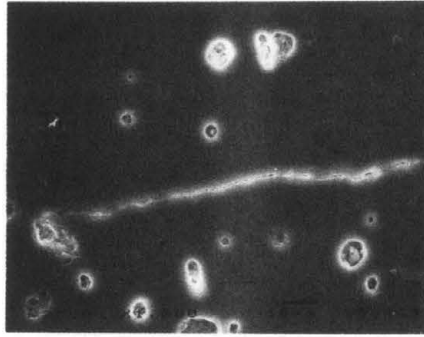
FIGURE 3.10. Crack interacting with several voids in glaze: SEM micrograph
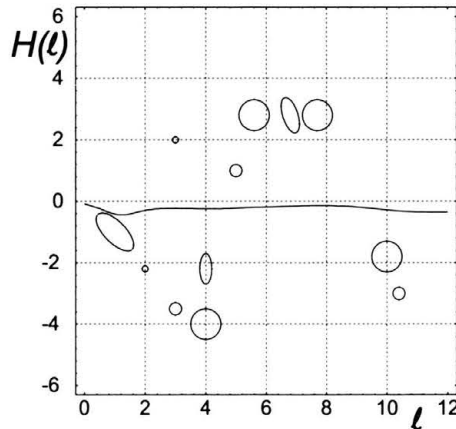(bar = $10\,\mu$m).



FIGURE 3.11. Crack interacting with several voids in glaze: simulation of the crack path.

resulting trajectory is in fact weakly deflected from the straight direction, a
result once more consistent with the simulation shown in Fig. 3.11.

Figure 3.12 is relative to a slip cast TZP material, with a $130\,\mu$m-diameter
spheroidal voids. This is much larger than those present in the glaze. The
crack trajectory results clearly attracted by the void and is simulated in
Fig. 3.13.

A general conclusion evidenced from the performed experiments is that
the crack trajectories appear to be deflected, in particular attracted, by the
voids. Moreover, the qualitative model predictions result to be in fairly good
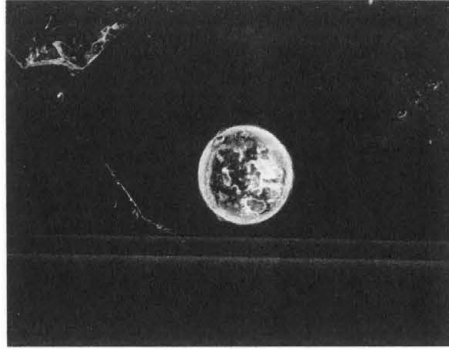agreement with the experiments.

FIGURE 3.12. Crack interacting with a void in a slip cast TZP ceramic: SEM micrograph (bar = $100\,\mu$m).
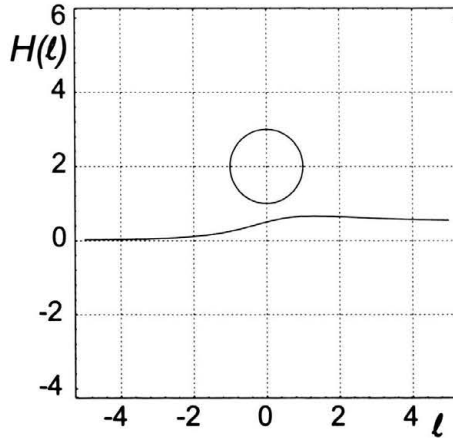


FIGURE 3.13. Crack interacting with a void in a slip cast TZP ceramic: simulation of the crack path.

## 3.4. Conclusions

Results obtained with a simple experimental setting on crack trajectories in ceramics containing nearly spherical voids have been presented. These results have been compared to the predictions of an analytical model. Despite of the limitative assumptions on which the model is based, a satisfactory agreement has been found. This encourages, on one hand, a systematic experimental investigation on various materials and, on the other hand, a practical use of the model in design and reliability analyses of ceramic components.

## 3.5. References

Bigoni, D., Movchan, A., Esposito, L., Serkov, S., and Valentini, M. (1996), Crack propagation in brittle, elastic solids with defects, in: *XII Italian Group of Fracture National Congress, Parma*, pp.59-67.

Bigoni, D., Serkov, S.K., Valentini, M. and Movchan, A.B. (1998), Asymptotic models of dilute composites with imperfectly bonded inclusions, *Int. J. Solids Structures*, Vol.35, pp.3239-3258.

Bower, A.F. and Ortiz, M. (1993), The influence of grain size on the toughness of monolithic ceramics, *J. Appl. Mech.*, Vol.115, pp.228-236.

Claussen, N. (1976), Fracture toughness of Al2O3 with an unstabilized ZrO2 dispersed phase, *J. Am. Ceram. Soc.*, Vol.59, pp.49-51.

Clarke, D.R. (1984), A simple calculation of process-zone toughening by microcracking, *J. Am. Ceram. Soc.*, Vol.C-15, January 1984.

Cotterel, B. and Rice, J.R. (1980), Slightly curved or kinked cracks, *Int. J. Fracture*, Vol.16, pp.155-169.

Duan, K., Mai, Y.W. and Cotterel, B. (1995), On the paradox between crack bridging and crack interaction in quasi-brittle materials, *J. Europ. Ceram. Soc.*, Vol.15, pp.1061-1064.

Dundurs, J. (1967), Effect of elastic constants on stress in a composite under plane deformation, *J. Comp. Mater.*, Vol.1, pp.310-322.

Evans, A.G. (1990), Perspective on the development of high-toughness ceramics, *J. Am. Ceram. Soc.*, Vol.73, pp.187-206.

Evans, A.G. and Fu, Y. (1985), Some effects of microcracks on the mechanical properties of brittle solids – II. Microcrack toughening, *Acta Metall.*, Vol.33, pp.1525-1531.

Faber, K.T. and Evans, A.G. (1983), Crack deflection process – I and II. Theory and experiments, *Acta Metall.*, Vol.31, pp.565-576 and 577-584.

Fu, Y. and Evans, A.G. (1985), Some effects of microcracks on the mechanical properties of brittle solids – I. Stress, strain relations, *Acta Metall.*, Vol.33, pp.1515-1523.

Hoagland, R.G. and Embury, J.D. (1980), A treatment of inelastic deformation around a crack tip due to microcracking, *J. Am. Ceram. Soc.*, Vol.63, pp.404-410.

Hutchinson, J.W. (1987), Crack tip shielding by micro cracking in brittle solids, *Acta Metall.*, Vol.35, pp.1605-1619.

MARSHALL, D.B. and LAWN, B.R. (1977), An indentation technique for measuring stresses in tempered glass surfaces, *J. Am. Ceram. Soc.*, Vol.60, pp.86-87.

MOVCHAN, A. B. (1992), Integral characteristic of elastic inclusions and cavity in two dimensional theory of elasticity, *Eur. J. Appl. Math.*, Vol.3, 21-30.

MOVCHAN, A.B. and MOVCHAN, N.V. (1995), *Mathematical Modelling of Solids with Non Regular Boundaries*, CRC Press.

MOVCHAN, A. B., NAZAROV, S. A. and POLYAKOVA, O. R. (1992), The quasi static grow of a semi-infinite crack in a plane containing small defects, *Comptes Rendus de L'Academie des Sciences*, Paris, series II, Vol.313, pp.1223-1228.

ORTIZ, M. (1988), Microcrack coalescence and macroscopic crack growth initiation in brittle solids, *Int. J. Solids Structures*, Vol.24, pp.231-250.

ORTIZ, M. and GIANNAKOPOULOS, A.E. (1989), Maximal crack tip shielding by microcracking, *J. Appl. Mech.*, Vol.56, pp.279-290.

PEZZOTTI, G. (1993), On the actual contribution of crack deflection in toughening platelet-reinforced brittle-matrix composites, *Acta Metall. Mater.*, Vol.41, pp.1825-1839.

PEZZOTTI, G., OKAMOTO, Y., NISHIDA, T. and SAKAI, M. (1996), On the near-tip toughening by crack-face bridging in particulate and platelet-reinforced ceramics, *Acta Mater.*, Vol.44, pp.899-914.

PÓLYA, G. and SZEGÖ G. (1951), Isoperimetric inequalities in mathematical physics, *Ann. Math. Studies*, Vol.27 Princeton University Press, New York.

ROSE, L.R.F. (1986), Microcrack interaction with a main crack, *Int. J. Fracture*, Vol.31, pp.233-242.

RUBINSTEIN, A.A. (1986), Macro-crack-micro-defect interaction, *J. Appl. Mech.*, Vol.53, pp.505-510.

SALOMONI, A., STAMENKOVIC, I., TUCCI, A. and ESPOSITO, L. (1992), Sintering of alumina and zirconia greens obtained via slip casting and pressure slip casting, in: *Proc. Symp. Forming Science and Related Properties of Ceramics*, M.J. Cima, (Ed.), The American Ceramic Society, Westerville, OH, pp.178-186.

SIH, G.C. (1974), Strain-energy-density factor applied to mixed mode crack problems, *Int. J. Fracture*, Vol.10, pp.305-321.

THORPE, M.F. and JASIUK, I. (1992), New results in the theory of elasticity for two-dimensional composites, *Proc. R. Soc. Lond. A*, Vol.438, pp.531-544.

VALENTINI, M. (1998), *Fracture Propagation in Ceramic Materials*, Ph. D. Thesis (in Italian), University of Bologna, Bologna, Italy.

VALENTINI, M., SERKOV, S., BIGONI, D. and MOVCHAN, A. (1999), Crack propagation in a brittle elastic material with defect, *J. Applied Mech.*, Vol.66, pp.79-86.

XU, Y., ZANGVIL, A. and KERBER, A. (1997), SiC nanoparticle-reinforced $Al_2O_3$ matrix composites: role of intra- and intergranular particles, *J. Europ. Ceram. Soc.*, Vol.17, pp.921-928.

# Chapter 4

# Failure of silicon nitride in uniaxial compression

**Massimiliano Gei** [1], **Stefano Guicciardi** [2]
**and Davide Bigoni** [3]

*Failure modes of silicon nitride cylinders have been investigated under uniaxial compression at 1200°C in air. Samples with different aspect ratios (h/d) have been tested: 5/2, 4/2, 2/2, and 1/2 (mm/mm). In all cases, the stress/strain curves evidence an initial linear portion followed by a peak and a slight softening, denoting a plastic behaviour. Most of the tests were interrupted at about 3-4% of load drop after the peak, and the samples observed with optical and electronic microscope. Two samples catastrophically broke in correspondence of the test stop and further observations were precluded. In all the other cases, the observed failure patterns involve modes presenting interesting symmetries. Particularly, surface exfoliation seems to play a central role in limiting the load-bearing capacity of the sample. The reason of such a behaviour may be interpreted in different ways, though we believe that a surface bifur-*

[1] Dipartimento di Scienze e Metodi dell'Ingegneria, Università di Modena e Reggio Emilia, Via Fogliani 1, 42100 Reggio Emilia, Italy

[2] IRTEC-CNR, Via Granarolo 64, 48018 Faenza, Italy.

[3] Dipartimento di Ingegneria Meccanica e Strutturale, Università di Trento, Via Mesiano 77, 38050 Trento, Italy.

*cation mechanism is the more likely to have occurred. In addition to this surface mode, traces of localized patterns of deformations – which initiated and propagated macro-cracks – can be found in some samples. A bifurcation analysis, which takes into account the surface residual stress induced by machining, has been carried out in order to describe the specific failure mode in terms of surface instability. The first failure mode predicted by this approach is an antisymmetric mode, while symmetric modes almost immediately follow. However, antisymmetric modes may be partially hampered by friction at the specimen/cushion contact. Moreover, the bifurcation analysis does not provide information for the post-critical behaviour, so that a possible interpretation of the observed failure mode is that the exfoliation mechanism may result as an evolution of a first antisymmetric mode into a symmetric one and that localized patterns of deformations follow to produce final macrocracks growth.*

## 4.1. Introduction

Advanced ceramics are known to be a good candidate as materials for high temperature structural applications (Larsen et al. 1985; Ichinose, 1987; Davidge and van de Vorde, 1990; Meetham, 1991; Raj, 1993). Unfortunately, the large use of ceramic components is restricted by intrinsic limits, like the low fracture toughness, and by a poor knowledge of the mechanical behaviour under the particular conditions in which the material will operate. Being brittle materials, advanced ceramics are mainly tested in tension, as this is considered the most harmful stress condition. However, this does not mean that failure cannot occur when compression loads are involved. For instance, a picture (taken with an optical microscope) is shown in Fig. 4.1 where an alumina water jet pump plunger is shown, which failed during service as a consequence of the seizure caused by the presence of hard dust particles in the water, a situation involving compressive rather than tensile stresses. From scientific point of view, failure in compression is an intriguing mechanism, much less investigated than fracture in tension (Horii and Nemat-Nasser, 1985; Ashby and Hallam, 1986; Sammis and Ashby, 1986; Meyers and Chawla, 1999).
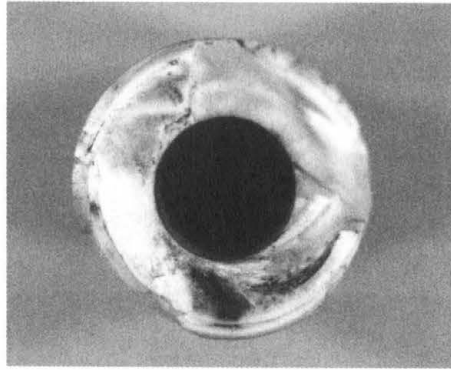
FIGURE 4.1. Failure of a pump plunger (external diameter 32 mm).

Of interest here for us is the behaviour of ceramic materials at high temperature and subject to compressive uniaxial stresses. For the specific ceramics under investigation, sometimes sintering aids are needed to obtain fully dense components. Usually, these sintering aids remain as intergranular vitreous phase in the final microstructure of the material. Being less refractory than the ceramic itself, at high temperature this phase becomes viscous promoting viscous flow and grain sliding when a stress is applied (Tsai and Raj, 1982; Wilkinson and Chadwick, 1991; Chan and Page 1993; Lueke et al. 1995). Moreover, under stress, due to the high hydrostatic pressure which sets up at the triple grain boundary junction, the intergranular glassy phase is the place where cavitation occurs mostly, even in compression (Lange et al. 1980; Crampon et al. 1997). At high temperature, when the above-mentioned relaxing mechanisms come into play, both the tensile and the compressive strengths of the material drop. The ratio of the tensile to the compressive strength, which at room temperature is about 1/10 (Atkins and Mai, 1988), could be higher when the temperature is increased, depending on which failure mechanism prevails.

A few works on short-term tensile tests appeared in the literature on advanced ceramics at high temperature (Ohji et al. 1990; Lin et al. 1993; Ohji and Yamauchi, 1994), while little or nothing can be found about short-term compression tests. This study represents an initial contribution in this almost unexplored field. In particular, we observe peculiar modes of failure of our tested cylindrical specimen and we propose an interpretation in terms of bifurcation theory, in which initiation of failure is explained by the occurrence of a surface bifurcation mode.

## 4.2. Experimental

The selected material was prepared by mechanically mixing an $\alpha$-Si$_3$N$_4$ powder (S-Stark LC 12 SX, H. C. Stark, New York, NY) with 8 wt% Y$_2$O$_3$ and 3 wt% Al$_2$O$_3$ as sintering aids. The mixture was uniaxially hot-pressed in a graphite crucible under a pressure of 30 MPa at 1810°C. X-ray diffractometry of the as-sintered material revealed that the main phases were $\beta$-Si$_3$N$_4$ with $\approx$ 10% residual $\alpha$-Si$_3$N$_4$. Some relevant microstructural and mechanical properties are summarised in Table 4.1 (measured at room temperature unless otherwise indicated). Further information can be found in Biasini et al. (1992).

TABLE 4.1. Microstructural and mechanical properties of the tested silicon nitride.

| Density  (g/cm$^3$) | 3.28 | | |
|---|---|---|---|
| Mean grain size  ($\mu$m) | 0.8 | | |
| $\beta$−grain aspect ratio | $\approx 7$ | | |
| Thermal expansion coefficient  ($10^{-6}$ °C$^{-1}$) | 3.25 | | |
| Hardness  (GPa) | $20.7 \pm 0.9$ | | |
| Young modulus  (GPa) | 301 | | |
| Toughness  (MPa$\sqrt{m}$) | $4.8\pm0.15$ | | |
| Flexural strength  (MPa) | R.T. | 895$\pm$35 | |
| | 1000°C | 603$\pm$39 | |
| | 1300°C | 281$\pm$22 | |

From the pellet (45 mm in diameter and 15 mm height), cylinders with a diameter of 2 mm were obtained by machining with their axis parallel to the hot-pressing direction. Samples with different heights were prepared: 1 mm, 2 mm, 4 mm and 5 mm, respectively. The tests were conducted in air at 1200°C using an Instron machine mod. 6025 (Instron Ltd., High Wycombe, U.K.). To avoid excessive friction at the interface, two larger Si$_3$N$_4$ cylinders (6 mm in diameter and 3 mm in height) machined from the same billet of the samples were inserted between the sample and the alumina pushrods. All the tests were conducted at a nominal strain rate of $5 \times 10^{-5}$s$^{-1}$. The strain rate was calculated from the specimen height and the crosshead displacement rate. The heating rate was 10°C/min and, before loading, the sample was allowed to soak for 18 min to insure thermal equilibrium. Most of the tests were stopped after a load drop of about 3-4% of the peak load. The load was removed before the cooling down. Two out of nine samples broke just after the test stop. To observe the full evolution of damage, one thick sam-

ple, 1 mm height, was deformed up to 0.12. The sample failure patterns were observed by optical (Leitz DMRME, Leica, Wetzlar, Germany) and scanning electron microscope (Cambridge Instruments, Cambridge, U.K.).

## 4.3. Results and discussion

Values of the peak loads for the investigated specimens are reported in Fig. 4.2, with reference to the sample height. The peak load shows a slight tendency to lower when the height of the sample is increased, Fig. 4.2. This slenderness effect will be later explained in terms of bifurcation theory and has been also documented for concrete (Hudson et al. 1971). Including all the values reported in Fig. 4.2, the peak load averages 4509 N with a standard deviation of 303 N.
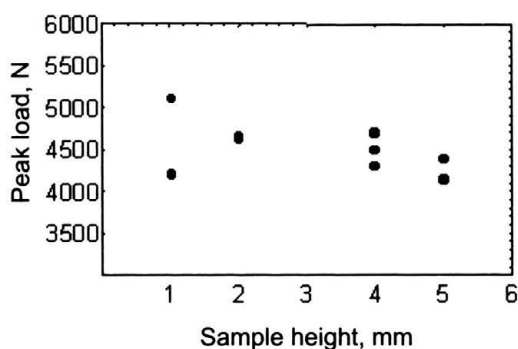


FIGURE 4.2. Compression peak loads vs. sample height for $Si_3N_4$ cylinders tested at 1200°C in air.

A standard procedure may be applied to the load-displacement curves in order to evaluate the effective strain of the sample. The system compliance can be estimated according to the following relationship:

$$C_T = \frac{h}{E\,S} + C_s, \qquad (4.1)$$

where $C_T$ is the total compliance, $h$ the initial height of the sample, $E$ the Young modulus, $S$ the cross section of the sample and $C_s$ the system compliance. Using at least three samples with different heights, it is possible to evaluate, by a linear regression analysis, the Young modulus of the material

and the system compliance. Subtracting the system compliance from the measured total compliance, the true load-displacement curve of the sample (and whence the nominal stress-deformation behaviour) is obtained. The stress-strain curves calculated in this way are reported in Fig. 4.3. The regression analysis gives a Young modulus value of about 105 GPa.
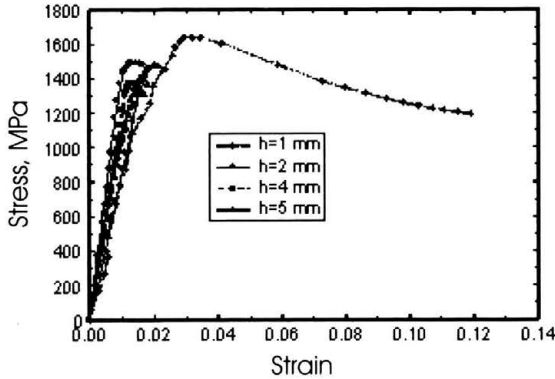


FIGURE 4.3. Compression stress-strain curves for $Si_3N_4$ cylinders tested at 1200°C in air; $h$ is the sample height.

The general shape of the stress-strain curve does not indicate any significant difference among samples with different height [this is also consistent with results presented in Hudson et al. (1971) for concrete, where the strong difference in the stress/strain curves is relative to the post-peak behaviour].

SEM micrographs of the samples are reported in Figs. 4.4–4.8, for different aspect ratios. Figures 4.4 and 4.5 pertain to aspect ratios 2/2 and 1/2, respectively. In both cases a surface exfoliation is evident. The exfoliation layer was quantified to be about 30-35 $\mu$m, Fig. 4.4. Internal cracks can also be observed, Fig. 4.5. Surface exfoliation is also very clear from Fig. 4.6 (aspect ratio 4/2). However, this sample was longitudinally sectioned and cracks almost parallel to the loading direction were observed, Fig. 4.7.

These may be interpreted as a localized axial-splitting failure mode. The thick sample (aspect ratio 1/2), Figs. 4.8 and 4.9, shows once more the surface exfoliation failure mode. Interestingly, this exfoliation is, in this case, a progressive mechanism: at least four exfoliated layers can be detected in Fig. 4.9 (particular of Fig. 4.8), with almost equal thickness of about 70 $\mu$m.

Summarizing, axially-symmetric surface exfoliation is the dominant failure mechanism (also consistent with the failure pattern of the pump plunger reported in Fig. 4.1). This is a well-known mechanism in rock mechanics (Var-
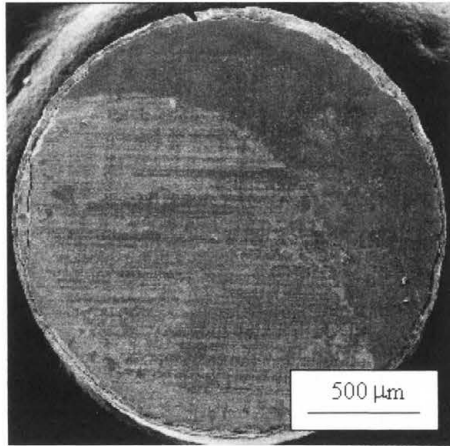
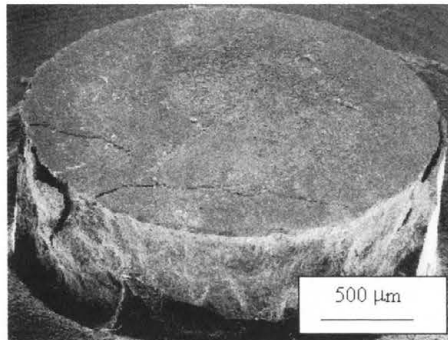FIGURE 4.4. SEM micrograph of a sample 2 mm height after test. Top view.



FIGURE 4.5. SEM micrograph of a sample 1 mm height after test.

doulakis and Sulem, 1995, their Fig. 1.2.6) and also found in axial compression of concrete (Hudson et al. 1971). The observed failure can be interpreted from a number of perspectives. It can be related to the effect of friction at the specimen/cushion contact, but in our case the test set up was specifically arranged to minimize this effect. Another possibility is to explain failure as an axial splitting phenomenon occurring as consequence of a branching of an inclined crack into a vertical fracture (Horii and Nemat-Nasser, 1985). This explanation appears rather weak in our case for different reasons. First, the crack branching mechanism would generate vertical, planar cracks instead of the observed axisymmetric modes. Second, that mechanism is typical of brit-
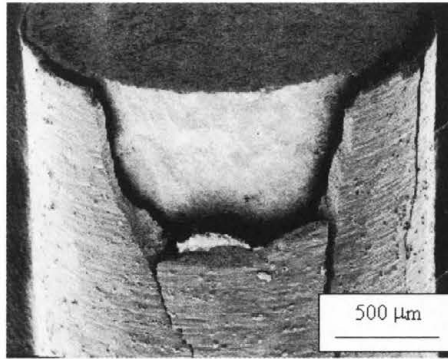
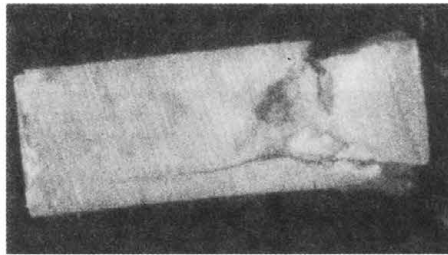FIGURE 4.6. SEM micrograph of a sample 4 mm height after test.



FIGURE 4.7. Longitudinal section of sample 4 mm height after test (Fig. 4.6).

tle materials, but in our case there is an evident ductility, so that behaviour of our material can be classified as "brittle-cohesive". Third, the presence of microcracks in the material before the test initiation cannot be *a priori* excluded in our case, but is strongly unlikely.

Alternatively, failure of our samples can be interpreted as the analogous for, say, a brittle-cohesive material of the surface effects observable in metal specimens (Rittel, 1990; Rittel et al. 1991). From this point of view, it may be interpreted as a bifurcation phenomenon: the homogeneous deformation pattern corresponding to the cylindrical shape may cease to be unique and bifurcate into an inhomogeneous pattern with surface undulations, which decay rapidly away from free surface. The problem of bifurcation of a cylindrical specimen subject to uniaxial compression was analyzed by Chau (1992) for rock-like materials and by Bigoni and Gei (2001) for metals. An analysis of these results reveals that the surface mode corresponds usually to bifurcation loads higher than those corresponding to barrelling or antisymmetric
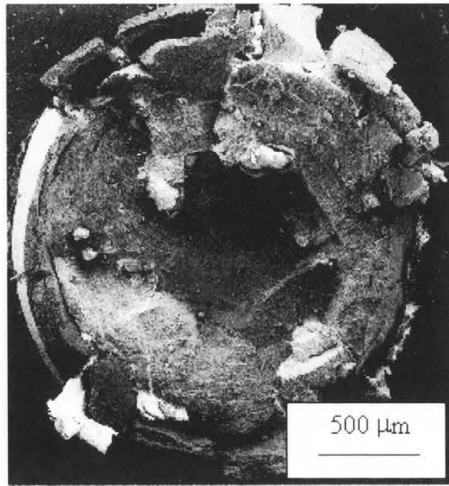
FIGURE 4.8. SEM micrograph of a sample 1 mm height deformed up to 0.12. Top view.
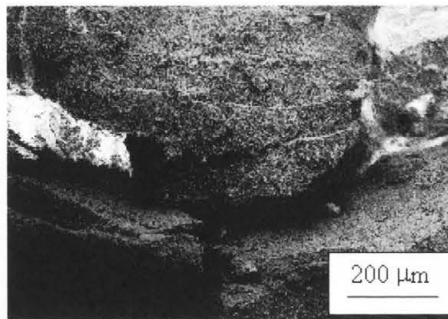


FIGURE 4.9. Detail of micrograph 4.8. Note the successive exfoliations formed during the test.

modes. Therefore, the explanation of the experimental results needs often to resort to some peculiar physical mechanisms. In rock mechanics, the presence of cracks parallel to the free surface is often invoked for bifurcation to occur (Vardoulakis and Sulem, 1995). For the analyzed material, such type of cracks are first unlikely and, second, they would not produce failure in a axisymmetric fracture mode. On the other hand, due to the fabrication process, a thin layer of material subject to residual stress may exist close to the free surface due to machining. This layer, often detected in ceramic materials (Samuel et al. 1989), could give rise to a surface bifurcation mode

occurring before other modes, a situation that can be anayzed in our case using models developed in (Bigoni et al. 1997; Bigoni and Gei, 2001).

In closure of the present discussion, it may be worth noting that the failure modes observed in our specimens share some similarities with modes relative to the triaxial compression of sand specimens (Desrues et al. 1996). In those specimens, failure has been attributed to a localization of deformation organized in a conical geometry. Although we do not completely agree with that conclusion [4], strain localization still remains a possibility of explaining our experimental results. Strain localization may be analyzed in terms of a bifurcation of the response of an infinite medium subject to increasing homogeneous strain (Rudnicki and Rice, 1975; Rice, 1977). For the material under consideration, there is not enough experimental evidence to adopt a definite constitutive framework. Anyway, a rough modelling may correspond to the Drucker-Prager model (Rudnicki and Rice, 1975). For this model strain localization was thoroughly analyzed. In our case, to interpret strain localization, a localized band must be found (almost) parallel to the loading direction. For the material under consideration, the ratio between tensile and compressive uniaxial yield stresses may be estimated to be around $1/7$. This value lies beyond the range of parameters analyzed in (Rudnicki and Rice, 1975). However, simple calculations show that a band parallel to the loading direction is predicted during softening and for values of plastic dilatancy sufficiently close to the value corresponding to associativity, so that localization does not appear to be excluded in the present context. To clarify this and the related issue of diffuse bifurcation modes – remaining the most likely explanation for the observed surface exfoliation – we present in the next section explicit calculations of diffuse and localized bifurcations.

## 4.4. Bifurcation analysis

Testing of materials at high temperature poses such difficulties that the presumption of extracting enough data from experiments to build a refined constitutive model for our material is simply illusory. Therefore, we propose a simple, hyperelastic model taken from the framework of $J_2$-deformation

---

[4] For fixed top of the testing machine, we think that strain localization should occur along the *two* weaker planes, inevitably present in any real specimen. Therefore, we believe that the localization observed in the sand specimens should have occurred *after* an axisymmetric bifurcation mode has occurred.

theory of plasticity, to describe our uniaxial experiments. The model will be tailored on our experimental results to describe a smooth transition from hardening to softening behaviour in uniaxial compression.

Loss of uniqueness in the incremental response of an incompressible, elastic cylinder subject to uniaxial compression is examined. A bifurcation point is detected when, at a certain stage of the primary path of equilibrium, an inhomogeneous field (called *bifurcation mode*) is found to satisfy the incremental equilibrium equations (in addition to the trivial homogeneous response).

In order to reproduce the physical conditions of the tested samples two problems have been considered:

- bifurcation of incompressible, homogeneous cylinders of 2 mm diameter and heights equal to 1, 2, 4 and 5 mm;
- bifurcation of cylinders with the above geometry and constitutive law, but with a circumferential residual stress of $-200$ MPa distributed in an external layer of the specimen of $10\,\mu$m thickness.

Compared to the former, the latter analysis did not give appreciably different results, so that we have concluded that residual stress does not influence significantly our problem. Therefore, only the former setting is considered below. Here, we briefly summarize the equations and the methodology, referring the interested reader to Bigoni and Gei (2001) for further details.

Let us consider a cylinder of radius $R$ and height $h$ in the undeformed, natural configuration $(C)$, whose points are labelled by $\boldsymbol{x}$, subject to a prescribed homogeneous deformation $\boldsymbol{\varphi}$. The current configuration $\bar{C} = \boldsymbol{\varphi}(C)$, whose points are denoted by $\bar{\boldsymbol{x}}$, is described by a cylindrical coordinates system $(r, \theta, z)$, with $z$ coincident with the axis of the cylinder and origin at the lower base of the body. The incompressibility constraint (det $\boldsymbol{F} = 1$, where [5] $\boldsymbol{F} = \mathrm{Grad}\varphi$) allows us to express the current state in terms of a single parameter, the logarithmic axial strain $\varepsilon$ ($\varepsilon < 0$ in compression), so that the current radius, $\bar{r}$, and height, $\bar{h}$, are given by $\bar{r} = \exp(-\varepsilon/2)R$ and $\bar{h} = \exp(\varepsilon)h$, respectively. In the context of small deformations $\varepsilon$ reduces to the axial principal strain.

The lateral surface of the cylinder is traction-free and a uniaxial stress is present directed along its axis. The following expression for the true stress $\sigma$ is particularly suited to fit the experimental stress-strain curves reported in Fig. 4.3

---

[5] The operator Grad is calculated with respect to $C$.

$$\sigma = K \exp\left(\frac{\varepsilon}{c\,\varepsilon_0}\right) \tanh\left(\frac{\varepsilon}{\varepsilon_0}\right), \tag{4.2}$$

with $K = 1650$ MPa, $c = 30$, and $\varepsilon_0 = 0.007$. Equation (4.2) corresponds to a nominal stress $s$ of the form

$$s = \frac{\sigma}{\exp(\varepsilon)} = K \exp\left(\frac{\varepsilon}{c\,\varepsilon_0} - \varepsilon\right) \tanh\left(\frac{\varepsilon}{\varepsilon_0}\right). \tag{4.3}$$

Let us consider now an incremental displacement field $\boldsymbol{u}(\bar{\boldsymbol{x}}) = \dot{\bar{\boldsymbol{x}}}$ superimposed upon the current deformation. In an updated Lagrangian formulation, the incremental equilibrium equations may be expressed in terms of increment in the first Piola-Kirchhoff stress tensor, $\dot{\boldsymbol{S}}$[6], as

$$\operatorname{div} \dot{\boldsymbol{S}} = \boldsymbol{0}. \tag{4.4}$$

The boundary conditions that complete the formulation of the incremental boundary-value problem are:

- null tractions at the lateral surface,

$$\dot{S}_{rr} = \dot{S}_{\theta r} = \dot{S}_{zr} = 0, \quad \text{at } r = \bar{r}; \tag{4.5}$$

- perfectly smooth contact with a rigid, flat constraint on the faces $z = 0$ and $\bar{h}$,

$$\dot{S}_{\theta z} = \dot{S}_{rz} = u_z = 0, \quad \text{at } z = 0, \bar{h}. \tag{4.6}$$

The constitutive equations are taken to be linear relationships between $\dot{\boldsymbol{S}}$ and $\boldsymbol{L} = \operatorname{grad} \boldsymbol{u}$ and are expressed in terms of three incremental moduli, $\mu_i$ ($i = 1, 2, 3$). In cylindrical components, these are

$$
\begin{aligned}
\dot{S}_{rr} &= \dot{p} + 2\mu_2 L_{rr} + 2(\mu_1 - \mu_2)L_{\theta\theta}, \\
\dot{S}_{\theta\theta} &= \dot{p} + 2\mu_2 L_{\theta\theta} + 2(\mu_1 - \mu_2)L_{rr}, \\
\dot{S}_{zz} &= \dot{p} + (2\mu_1 - \sigma)L_{zz}, \\
\dot{S}_{r\theta} &= \dot{S}_{\theta r} = (2\mu_2 - \mu_1)(L_{r\theta} + L_{\theta r}), \\
\dot{S}_{rz} &= \left(\mu_3 + \frac{\sigma}{2}\right)L_{rz} + \left(\mu_3 - \frac{\sigma}{2}\right)L_{zr}, \\
\dot{S}_{zr} &= \left(\mu_3 - \frac{\sigma}{2}\right)L_{rz} + \left(\mu_3 - \frac{\sigma}{2}\right)L_{zr},
\end{aligned}
\tag{4.7}
$$

---

[6] The first Piola-Kirchhoff stress tensor is defined as $\boldsymbol{S} = \det(\boldsymbol{F})\,\boldsymbol{\sigma}\boldsymbol{F}^{-T}$.

$$\dot{S}_{\theta z} = \left( \mu_3 + \frac{\sigma}{2} \right) L_{\theta z} + \left( \mu_3 - \frac{\sigma}{2} \right) L_{z\theta},$$

$$\dot{S}_{z\theta} = \left( \mu_3 - \frac{\sigma}{2} \right) L_{\theta z} + \left( \mu_3 - \frac{\sigma}{2} \right) L_{z\theta},$$

(4.7)
[cont.]

where $\dot{p}$ is the Lagrange multiplier associated with the incompressibility constraint.

The incremental moduli are functions of the pre-stress which affects the incremental response of the solid. In the framework of the finite strain generalization of the $J_2$−deformation theory (Hutchinson and Tvergaard, 1980; Neale, 1981), they depend on the tangent modulus ($E_t = d\sigma/d\varepsilon$) and secant modulus ($E_s = \sigma/\varepsilon$) of the curve (4.2) at $\sigma$ [7], namely

$$\mu_1 = \frac{1}{3} E_t, \qquad \mu_2 = \frac{1}{6} (E_s + E_t), \qquad \mu_3 = \frac{1}{2} E_s \varepsilon \coth \left( \frac{3}{2} \varepsilon \right). \qquad (4.8)$$

In order to simplify the formulation, we note that, exploiting the condition of incompressibility of the incremental deformation $[u_{r,r} + (u_r + u_{\theta,\theta})/r + u_{z,z} = 0]$, the components of $\boldsymbol{u}$ can be written in terms of two displacement potentials, $\Omega = \Omega(r, \theta, z)$ and $\Psi = \Psi(r, \theta, z)$, as

$$u_r = \Omega_{,rz} + \Psi_{,\theta}/r, \qquad u_\theta = \Omega_{,\theta z}/r - \Psi_{,r}, \qquad u_z = -\mathcal{M}(\Omega), \qquad (4.9)$$

where $\mathcal{M}(\cdot) = (\cdot)_{,rr} + (\cdot)_{,r}/r + (\cdot)_{,\theta\theta}/r^2$ is the two-dimensional Laplacian operator in polar coordinates.

Bifurcations are sought in the separate variables form

$$\begin{cases} \Omega(r, \theta, z) = \omega(r) \cos n\theta \sin \eta z, \\[2mm] \Psi(r, \theta, z) = \psi(r) \sin n\theta \cos \eta z, \\[2mm] \dot{p}(r, \theta, z) = q(r) \cos n\theta \cos \eta z, \end{cases} \qquad (4.10)$$

where $\eta = k\pi/\bar{h}$ ($k = 1, 2, \dots$) and $n$ ($n = 0, 1, 2, \dots$) are, respectively, the longitudinal and the circumferential wave numbers. The definition of $\eta$ assures that boundary conditions (4.6) are satisfied.

---

[7] In general, $E_s$ and $E_t$ are calculated with respect to the equivalent stress ($\sigma_e = \sqrt{3\,\sigma_{\text{dev}} \cdot \sigma_{\text{dev}}/2}$) – uniaxial logarithmic strain ($|\varepsilon|$) curve, where $(\cdot)_{\text{dev}}$ denotes the deviatoric part of the relevant argument. In our case $\sigma_e = |\sigma|$.

Substitution of $(4.10)_{1,2}$ into (4.9), (4.7), and (4.4) yields two ordinary differential equations for $\omega(r)$ and $\psi(r)$ and an expression for $q(r)$. The solutions for the three functions are

$$\begin{cases} \omega(r) = a_1 J_n(\rho_1 \eta r) + a_2 J_n(\rho_2 \eta r), \\ \psi(r) = b I_n(\rho_3 \eta r), \\ q(r) = (2\mu_1 - \mu_3 - \sigma/2)\eta \mathcal{L}_n(\omega) - (\mu_3 - \sigma/2)\mathcal{L}_n^2(\omega)/\eta, \end{cases} \qquad (4.11)$$

where $a_i$ $(i = 1, 2)$ and $b$ are arbitrary constants, $J_n(x)$ and $I_n(x)$ are – respectively – the ordinary and the modified Bessel functions of order $n$, $\mathcal{L}_n(\cdot) = (\cdot)'' + (\cdot)'/r - n^2(\cdot)/r^2$ is the Bessel operator, $\rho_i^2$ $(i = 1, 2)$ are the solutions of the characteristic equation

$$(\mu_3 - \sigma/2)\rho^4 + 2(\mu_1 + \mu_2 - \mu_3)\rho^2 + (\mu_3 + \sigma/2) = 0, \qquad (4.12)$$

and

$$\rho_3^2 = \frac{\mu_3 + \sigma/2}{2\mu_2 - \mu_1}. \qquad (4.13)$$

It is worth noting that the nature of roots $\pm\rho_1$ and $\pm\rho_2$ of (4.12) defines the classification of regimes: complex conjugate $\pm\rho_1$ and $\pm\rho_2$ in the elliptic complex regime (EC); pure imaginary $\pm\rho_1$ and $\pm\rho_2$ in the elliptic imaginary regime (EI); real $\pm\rho_1$ and $\pm\rho_2$ in the hyperbolic regime (H); two real and two pure imaginary $\pm\rho_1$ and $\pm\rho_2$ in the parabolic regime (P). It should be noted that failure of ellipticity corresponds to localization of deformation. Therefore, the investigation of bifurcation is restricted to the elliptic range, where $\mu_3 + \sigma/2 > 0$, $2\mu_2 - \mu_1 > 0$, so that the coefficient $\rho_3^2$ (4.13) is always positive either in (EI) or in (EC) regimes.

Equations (4.9)–(4.11) fully specify the displacement field and, through (4.7), the incremental stress state. The imposition of the boundary conditions on the lateral surface (4.5) provides a homogeneous algebraic system for the constants $a_i$ $(i = 1, 2)$ and $b$. Non trivial solution are obtained if the determinant of the associated matrix vanishes (*bifurcation condition*). Once the current geometry and state is known, the bifurcation mode has to be selected in terms of the circumferential wave number $n$ and of the dimensionless parameter $\eta\bar{r}$, so that the bifurcation condition determines the critical logarithmic strain $\varepsilon_{\text{bif}}$.

### 4.4.1. Results

Bifurcation points and modes for samples with aspect ratios $1/2$, $2/2$, $4/2$ and $5/2$ have been computed and reported in Figs. 4.10 and 4.11. The bifurcation points are marked in Fig. 4.10 on the uniaxial stress vs. logarithmic strain curves with vertical segments, since they correspond to two different values of Cauchy (or true) and nominal stresses, but to the same value of strain.

In the present problem, localization of deformation occurs when the (EC)/(H) boundary is touched, i.e. at $|\varepsilon_{loc}| = 0.0693$, as can be calculated from Eq. (4.12). The point corresponding to strain localization is reported in the first plot of Fig. 4.10, where it can be clearly appreciated that localization occurs in the strain softening regime.

The critical, i.e. occurring at lowest strain, bifurcation point for each of the four aspect ratios considered are reported in the first plot of Fig. 4.10. All the four critical bifurcations correspond to an antisymmetric mode, characterized by $n = 1$. Note that the critical bifurcation occurs

- when the material is still in the hardening regime, for the aspect ratios $h/d = 4/2$ and $5/2$,
- at around the peak of stress/strain curve, for the aspect ratio $h/d = 2/2$,
- during softening, for the aspect ratio $h/d = 1/2$.

However, bifurcation modes with $n \neq 1$ become available at strains slightly higher than the critical, specially for thick samples. In order to present a complete picture of the bifurcation landscape, the first six modes for every aspect ratio are indicated in Fig. 4.10 and the relative parameters listed in Table 4.2.

For $h/d = 1/2$ (second plot in Fig. 4.10), the mode P, following the mode M, is a surface-type mode with double longitudinal wave number – corresponding to half wavelength – and $n = 4$. Moreover, the mode H (axisymmetric) is almost coincident with the mode G (antisymmetric) for the aspect ratio $2/2$ (third plot in Fig. 4.10).

After the sixth mode is attained, infinite bifurcation modes follow one upon other and become closer and closer towards the point S, representing the surface instability threshold ($|\varepsilon_{si}| = 0.0349$). Continuing along the uniaxial curve, strain localization occurs as a final instability.
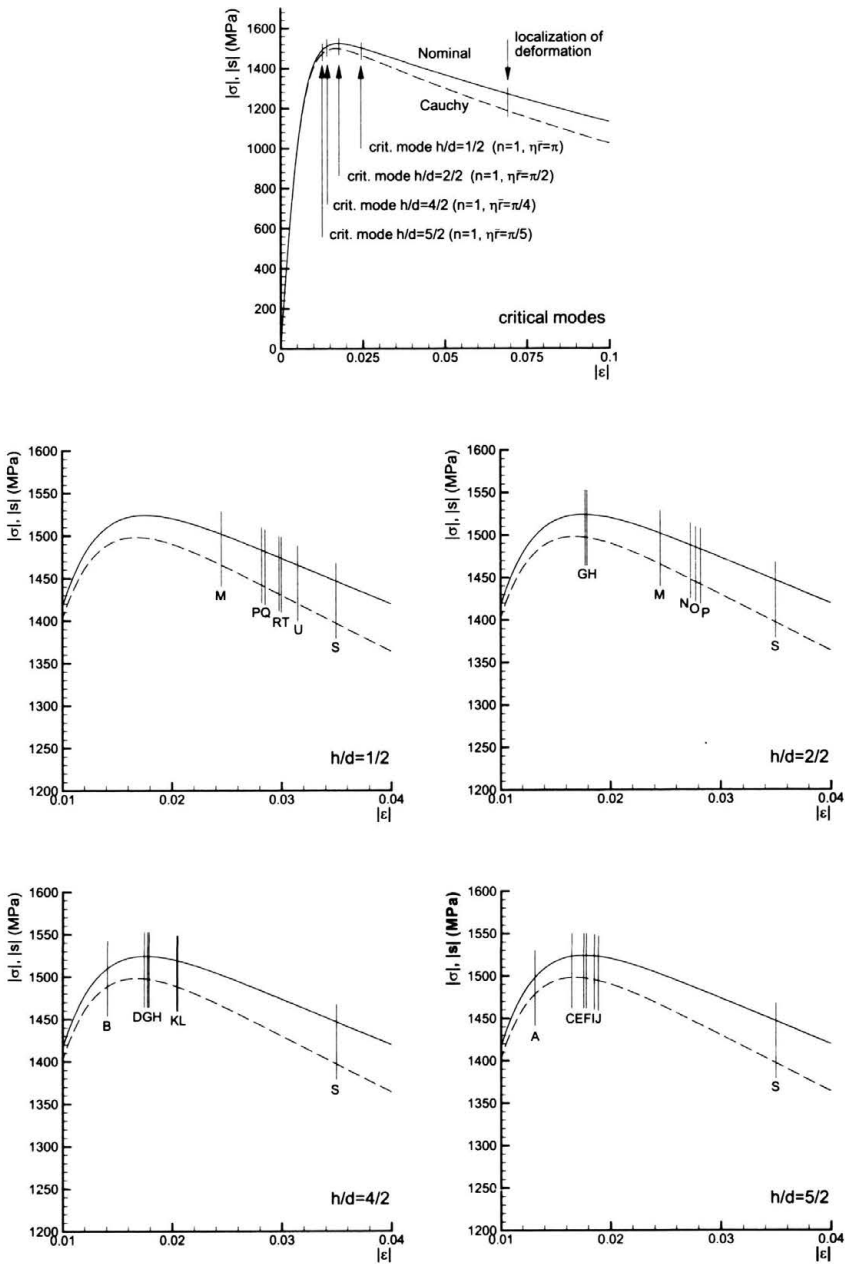
FIGURE 4.10. True (Eq. 4.2) and nominal (Eq. 4.3) stress vs. logarithmic strain curves (the former is dashed), with superimposed critical points for bifurcation. S denotes surface instability that occurs at $|\varepsilon_{si}| = 0.0349$. Characteristics of modes A through U are reported in Table 4.2.
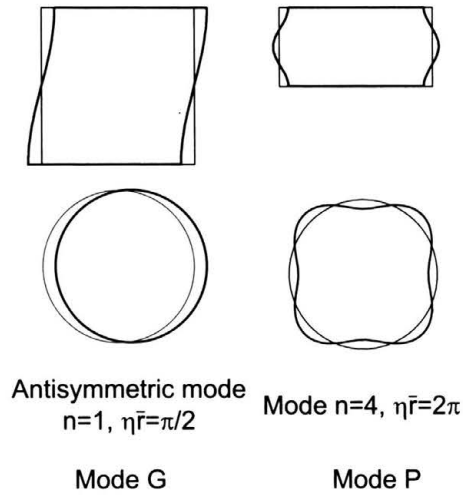
Antisymmetric mode
n=1, $\eta\bar{r}=\pi/2$

Mode n=4, $\eta\bar{r}=2\pi$

Mode G                    Mode P

FIGURE 4.11. Sketch of mode G (critical mode for the specimen $h/d=2/2$) and mode P.

TABLE 4.2. Bifurcation mode parameters of Fig. 4.10.

| Mode | $n$ | $\eta\bar{r}$ | $|\varepsilon_{\text{bif}}|$ | Mode | $n$ | $\eta\bar{r}$ | $|\varepsilon_{\text{bif}}|$ |
|------|-----|-----|-----|------|-----|-----|-----|
| A | 1 | $\pi/5$ | 0.0131 | K | 1 | $3\pi/4$ | 0.0204 |
| B | 1 | $\pi/4$ | 0.0143 | L | 0 | $3\pi/4$ | 0.0205 |
| C | 1 | $2\pi/5$ | 0.0165 | M | 1 | $\pi$ | 0.0245 |
| D | 0 | $\pi/4$ | 0.0175 | N | 2 | $3\pi/2$ | 0.0273 |
| E | 0 | $\pi/5$ | 0.0176 | O | 3 | $3\pi/2$ | 0.0278 |
| F | 0 | $2\pi/5$ | 0.0177 | P | 4 | $2\pi$ | 0.0282 |
| G | 1 | $\pi/2$ | 0.0178 | Q | 2 | $\pi$ | 0.0285 |
| H | 0 | $\pi/2$ | 0.0179 | R | 3 | $3\pi$ | 0.0298 |
| I | 0 | $3\pi/5$ | 0.0185 | T | 6 | $3\pi$ | 0.0299 |
| J | 1 | $3\pi/5$ | 0.0188 | U | 8 | $4\pi$ | 0.0315 |

From the reported results it can be clearly understood that

*strain localization will never occur in a homogeneously deformed specimen, but will take place on a bifurcated deformation path* [8].

We observe that the surface mode S corresponds to an "orange-peel" pattern where both $n$ and $\eta\bar{r}$ diverge. Something similar was found, for a simpler

[8] Therefore a calculation of strain localization performed assuming homogeneity may retain some validity only when the bifurcated path followed by the specimen does not involve high strain inhomogeneities.

uniaxial stress-strain law than (4.2), by Bigoni and Gei (2001) for uniaxial tension, but not for compression.

In terms of total compression loads, the nominal peak load calculated from the constitutive law (4.3) is equal to 4788 N. For $h/d = 4/2$ and $5/2$ bifurcation occurs for a load of about 4749 N and 4706 N, respectively, indicating the presence of the slenderness effect noticed in the experimental results (Fig. 4.2). This effect, that is a consequence of loss of uniqueness in the hardening branch, may be observed in specimens having $h/d > 1$.

## 4.5. Conclusions

Experimental results have been presented, relative to uniaxial compression at $1200°C$ in air of silicon nitride cylinders. Results pertain to different diameter/height ratios. In the experiments, this parameter did not influence much the overall features of the stress-strain curve (which in the present case were interrupted just after the peak) and of the failure modes. For all investigated diameter/height ratios, failure was initiated by surface exfoliation followed by the formation and growth of macrocracks. Three possible interpretations of this behaviour seem to cover all possibilities. These are:

1. effects related to specimen/cushion friction;
2. effects related to the presence of microcracks;
3. effects related to a bifurcation mechanism emerging during deformation.

The first possibility should be minimized with the assumed experimental setup and microcracks can also be excluded, so that the second possibility is also ruled out. Only the last possibility appears relevant to our situation. Bifurcations fall within the following classes:

- diffuse bifurcations:
  - axisymmetric modes,
  - antisymmetric modes;
- surface modes;
- localized modes.

Presented calculations, performed with a material model suitable to describe our uniaxial experiments, show that:

- the first bifurcation mode occurs around (before for slender specimens, after for thick) the peak of the uniaxial stress/strain curve, in agreement

with the observed failure. This explains the observed slight decrease in the peak load, as related to the increase of the slenderness of the specimen;

- the first possible bifurcation mode is always antisymmetric for all considered geometries;
- the surface modes follow after diffuse mode, but occur "not far" from the first mode;
- localized modes always follow after surface modes;
- the above results remain practically unchanged even if a circumferential residual stress is considered.

Following the bifurcation approach, it can be concluded that the observed failure starts at around the peak of the stress-strain curve as an antisymmetric mode[9] and degenerate during postcritical behaviour to a surface mode, leading to final failure, with possible strain localization.

## 4.6. References

ASHBY, M.F. and HALLAM, S.D. (1986), The failure of brittle solids containing small cracks under compressive stress states, *Acta Metall.*, Vol.34, pp.497-510.

ATKINS, A.G. and MAI, Y.-W. (1988), *Elastic and Plastic Fracture*, Ellis Horwood Series in Engineering Science, Ellis Horwood Ltd, Chichester, U.K., p.175.

BIASINI, V., GUICCIARDI, S. and BELLOSI, A. (1992), Silicon nitride-silicon carbide composite materials, *Refractory Metals Hard Materials*, Vol.11, pp.213-221.

BIGONI, D. and GEI, M. (2001), Bifurcations of a coated, elastic cylinder, *Int. J. Solids Struct.*, Vol.38, pp.5117-5148.

BIGONI, D., ORTIZ, D. and NEEDLEMAN, A. (1997), Effect of interfacial compliance on bifurcation of a layer bonded to a substrate, *Int. J. Solids Struct.*, Vol.34, pp.4305-4326.

CHAN, K.S. and PAGE, R.A. (1993), Creep damage development in structural ceramics, *J. Am. Ceram. Soc.*, Vol.76, pp.803-826.

CHAU, K.T. (1992), Non-normality and bifurcation in a compressible pressure-sensitive circular cylinder under axisymmetric tension and compression, *Int. J. Solids Struct.*, Vol.29, pp.801-824.

---

[9] Though antisymmetric modes might be at least partially impeded by friction at the specimen/cushion contact.

CRAMPON, J., DUCLOS, R., PENI, F., GUICCIARDI, S. and DE PORTU, G. (1997), Compressive creep and creep failure of 8Y(2)O(3)/3Al(2)O(3)-doped hot-pressed silicon nitride, *J. Am. Ceram. Soc.*, Vol.80, pp.85-91.

DAVIDGE, R.W. and VAN DE VORDE, M.H. (1990), *Design with Structural Ceramics*, Elsevier Science Publishers Ltd, Barking, U.K.

DESRUES, J., CHAMBON, R., MOKNI, M. and MAZEROLLE, F. (1996), Void ratio evolution inside shear bands in triaxial sand specimens studied by computed tomography, *Géotechnique*, Vol.46, pp.529-546.

HORII, H. and NEMAT-NASSER, S. (1985), Compression-induced microcrack growth in brittle solids: axial splitting and shear failure, *J. Geophys. Res.*, Vol.90, pp.3105-3125.

HUDSON, J.A., BROWN, E.T. and FAIRHURST, C. (1971), Proceedings 13th Symp. on Rock Mech., Cording, E.J., (Ed.), University of Illinois Urbana Press, U.S.A.

HUTCHINSON, J.W. and TVERGAARD, V. (1980), Surface instabilities on statically strained plastic solids, *Int. J. Mech. Sci.*, Vol.22, pp.339-354.

ICHINOSE, N. (1987), *Introduction to Fine Ceramics*, John Wiley & Sons Ltd, Chichester, U.K.

LANGE, F.F., DAVIES, B.I. and CLARKE, D.R. (1980), Compressive creep of Si3N4/MgO alloys. Part I: Effect of composition, *J. Mater. Sci.*, Vol.15, 601-610.

LARSEN, D.C., ADAMS, J.W., JOHNSON, L.R. and TEOTIA, A.P.S. (1985), *Ceramic Material for Advanced Heat Engines*, Noyes Publications, Park Ridge, U.S.A.

LIN, C.K.J., JENKINS, M.G. and FERBER, M.K. (1993), Tensile dynamic and static fatigue relations for a hiped silicon-nitride at elevated temperatures, *J. Europ. Ceram. Soc.*, Vol.12, pp.3-13.

LUEKE, W.E., WIEDERHOM, S.M., HOCKEY, B.J., LONG, G.G. and KRAUSE JR., R.F. (1995), Cavitation contributes substantially to creep in silicon nitride, *J. Am. Ceram. Soc.*, Vol.78, pp.2085-2096.

MEETHAM, G.W. (1991), High-temperature materials. A general review, *J. Mater. Sci.*, Vol.26, pp.853-860.

MEYERS, M.A. and CHAWLA, K.K. (1999), *Mechanical Behaviour of Materials*, Prentice Hall, NJ.

NEALE, K.W. (1981), Phenomenological constitutive laws in finite plasticity, *SM Archives*, Vol.6, Sijthoff and Noordhoff International Publishers, Alphen aan den Rijn, The Netherlands.

OHJI, T. and YAMAUCHI, Y. (1994), Diffusional crack growth and creep rupture of silicon carbide doped with alumina, *J. Am. Ceram. Soc.*, Vol.77, pp.678-682.

OHJI, T., YAMAUCHI, Y., KANEMATSU, W. and ITO, S. (1990), Dependence of high-temperature tensile strength on displacement rate for hot-pressed silicon-nitride, *J. Mater. Sci.*, Vol.25, pp.2990-2996.

RAJ, R. (1993), Fundamental research in structural ceramics for service near 2000 degrees C, *J. Am. Ceram. Soc.*, Vol.76, pp.2147.

RICE, J.R. (1977), The localization of plastic deformation, in: *Theoretical and Applied Mechanics*, Koiter, W.T., (Ed.), North-Holland, Amsterdam, pp.207-220.

RITTEL, D. (1990), The influence of microstructure on the macroscopic patterns of surface instabilities in metals, *Scripta Metall. Mater.*, Vol.24, pp.1759-1764.

RITTEL, D., AHARONOV, R., FEIGIN, G. and ROMAN, I. (1991), Experimental investigation of surface instabilities in cylindrical tensile metallic specimens, *Acta Metall. Mater.*, Vol.39, pp.719-724.

RUDNICKI, J.W. and RICE, J.R. (1975), Conditions for the localization of deformations in pressure-sensitive dilatant materials, *J. Mech. Phys. Solids*, Vol.23, pp.371-394.

SAMMIS, C.G. and ASHBY, M.F. (1986), The failure of brittle porous solids under compressive stress states, *Acta Metall.*, Vol.34, pp.511-526.

SAMUEL, R., CHANDRASEKAR, S., FARRIS, T.N. and LICHT, R.H. (1989), Effect of residual stresses on the fracture of ground ceramics, *J. Am. Ceram. Soc.*, Vol.72, pp.1960-1966.

TSAI, R.L. and RAJ, R. (1982), *Acta Metall.*, Vol.30, p.1043.

VARDOULAKIS, I. and SULEM, J. (1995), *Bifurcation Analyisis in Geomechanics*, Chapman & Hall, London, U.K.

WILKINSON, D.S. and CHADWICK, M.M. (1991), Creep mechanisms in glass-containing ceramics, *J. Phys. III*, Vol.1, pp.1131-1139.

Chapter **5**

# Forming of advanced ceramics

---

**Andrea Piccolroaz** [1], **Alessandro Gajo** [1]
**and Davide Bigoni** [1]

*Cold compaction of powders is a basic process in ceramics forming. After a review of existing phenomenological models for mechanical behaviour of powders, experiments are presented, which were performed on a commercial alumina powder. These are used to calibrate a plasticity model for soils, namely, the Cam-clay. F.E. simulations are finally presented of a simple forming process and results are shown to be in qualitative agreement with experiments.*

## 5.1. Introduction

Powder compaction is a process in which granular materials are made cohesive through mechanical densification. These may or may not involve temperature and permit an efficient production of parts ranging widely in size and shape to close tolerances with low drying shrinkage (Reed, 1995).

---

[1] Dipartimento di Ingegneria Meccanica e Strutturale, Università di Trento, Via Mesiano 77, 38050 Trento, Italy.

Metallurgical (German, 1984) and pharmaceutical (Lordi and Cuitiño, 1997) applications are common; moreover, forming of traditional (for instance: ceramic tiles, porcelain products) and structural ceramics (for instance: chip carriers, spark plugs, cutting tools) involves essentially powder compaction. The focus of this chapter is the analysis of cold compaction of ceramic powders to obtain a constitutive model capable of describing green body formation.

In the case of advanced ceramics, a ceramic powder is usually obtained through spray-drying and is made up of particles (granules) of dimensions ranging between 50 and $200\,\mu m$ (Fig. 5.1), coated with the binder system. The granules are aggregates of crystals having dimensions on the order $1\,\mu m$.
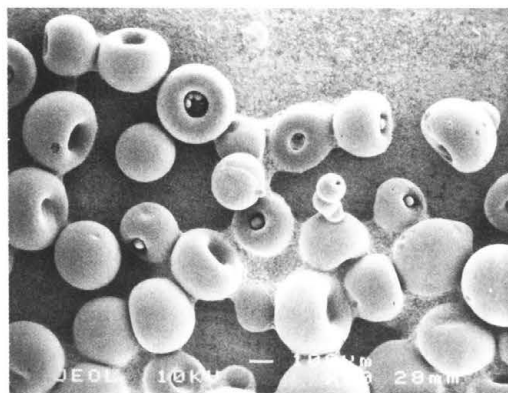


FIGURE 5.1. SEM micrograph of the analyzed alumina powder (bar $= 100\,\mu m$).

Figure 5.1 refers to the specific material analyzed in the present article. This is a commercial ready-to-press alumina powder (96% purity), manufactured by Martinswerk GmbH (Bergheim, Germany) and identified as 392 Martoxid KMS-96. The data presented by the manufacturer are given in Table 5.1. It can be noted from Fig. 5.1 that the granules have a mean diameter of $250\,\mu m$.

Densification of ceramic powders induced by cold pressing can be divided in three main stages (Matsumoto, 1986; Reed, 1995; Bortzmeyer, 1996):

- **Phase I** granule sliding and rearrangement,
- **Phase II** granule deformation,
- **Phase III** granule densification.

TABLE 5.1. Granulometric and density properties of the tested alumina powder.

| MWM 28 Vibration sieving | |
|---|---|
| sieve residue $> 300\,\mu$m | 3.9% |
| sieve residue $> 150\,\mu$m | 56.3% |
| sieve residue $< 63\,\mu$m | 2.5% |
| Bulk density (g/cm$^3$) | 1.219 |
| Green density (p $= 50$ MPa) (g/cm$^3$) | 2.39 |
| Fired density (T$=1600°$C, 2h) (g/cm$^3$) | 3.77 |

The three phases of densification can be distinguished by the changes in the inclination of the semi-logarithmic plot of density versus applied pressure. These determine the "breakpoint pressure" and "joining pressure" points. The Phase I always occurs in early volumetric deformation of granular materials (at low stress), so that it has been thoroughly investigated for geomaterials. However, densification process in ceramic powders is often highly non homogeneous, so that usually at least two phases coexist. With reference to continuum mechanics modelling, phases II and III of deformation are related to the gain in cohesion of the material and have been scarcely investigated.

### 5.1.1. The need of research

Many technical, unresolved difficulties arise in the forming process of ceramic materials (Brown and Weber, 1988; Bortzmeyer, 1996). In fact, if on one hand the compact should result intact after ejection, should be handleable without failure and essentially free of macro defects, on the other hand, defects of various nature are always present in the greens (Deis and Lannutti, 1998; Ewsuk, 1997; Hausner and Kumar-Mal, 1982; Glass and Ewsuk, 1997; Thompson, 1981b), badly influencing local shrinkage during sintering (Deis and Lannutti, 1998; Hausner and Kumar-Mal, 1982). Defects can be caused by densification process, that may involve highly inhomogeneous strain fields, or by mold ejection, often producing end and ring capping, laminations, shape distortions, surface defects, vertical cracks, and large pores (Glass and Ewsuk, 1997).

In view of a reduction in the defects – crucial in setting the reliability of the final piece – simulations of the forming process become an important tool to optimize ceramics design (in terms of shape of final piece and type and composition of the powder).

### 5.1.2.  A state-of-the-art

Though compaction of granular materials has been the focus of intense research, ceramic powders have been scarcely considered. We review various contributions and methodologies developed for mechanical modelling of granular materials of different nature.

**Metallic powders.**  Several phenomenological or micromechanical models have been developed to describe Phases I and II densification for various metallic powders. Some of them are reviewed below.

Compaction of metallic powders under isostatic pressure was considered by Arzt (1982) and Helle et al. (1985). Other models describe the powder compaction into cylindrical dies with axial loading and concern generic powders (Thompson, 1981a; Kenkre et al., 1996).

Brown and Weber (1988) develop an elastic-plastic model at large strains based on an *ad hoc* yield function. Both experiments and numerical simulations are presented.

Micromechanical approaches have been developed by Fleck et al. (1992), Akisanya et al. (1994) and Fleck (1995). Akisanya et al. (1994) derive a relationship between pressure and density defined within the context of Phase II. Fleck et al. (1992) and Fleck (1995) obtain analytical expressions for yield surfaces at the level of a phenomenological theory of plasticity. The analyses are based on a ductile behaviour, typical of metallic powders. Other works, based on the micromechanical approach are hardly extendible to the simulation of industrial processes with complex geometries (Cuitiño and Gioia, 1999; Kuhn et al. 1991; Pavanachand and Krishnakumar, 1997; Subramanian and Sofronis, 2001; Ng, 1999; Parhami et al. 1999).

Gurson and McCabe (1992) show experimental results concerning high pressure triaxial tests on tungsten-nickel-iron powders and discuss possibility of simulating the cohesion increase by using a particular hardening mechanism.

Tran et al. (1993) use an elastic-plastic model analogous to those developed for sands, in a large strain formulation. Even if the model is limited to Phase I, the approach allows the numerical simulation of the forming process of simple components.

Lewis et al. (1993) propose a computer-aided simulation procedure for metal powder die compaction. They develop the model within the large deformation theory, using a modified von Mises criterion for porous material as proposed by Oyane et al. (1973). The friction between the powder compact and the rigid die wall is taken into account. Simulations of the die compaction of powder compact having variable cross-sections are presented. The main limits in this approach are the as-

sumptions of a rigid-plastic behaviour and a yield surface independent of the third stress invariant.

Jernot et al. (1994) propose a microstructural approach to simulate metallic powder compression, based on tools of mathematical morphology (erosion and dilation).

Brown and Abou-Chedid (1994) illustrate pressing experiments and present an elastic-plastic model. They claim that in the field of metallic powders there are no experimental tests enabling to clarify the issue of flow-rule associativeness or lack of it.

Lippmann and Iankov (1997) describe the process of compaction and sintering by means of a rigid-plastic model, which cannot describe the so-called "springback" effect.

The large strain elastic-plastic model proposed by Oliver et al. (1996) is employed in f.e. simulations accounting for friction between powder and cast. In the constitutive modelling a yield surface independent of the third stress invariant is assumed.

Ariffin et al. (1998), Lewis and Khoei (1998) and Khoei and Lewis (1999) use a large strain formulation of a constitutive model which combines Mohr-Coulomb criterion with an elliptical cap model. Friction between powder and cast is accounted for and remeshing is used to follow complex geometries. This model does not describe the increase in cohesion when the material is subjected to hydrostatic stress states.

Using several elastic-plastic models, Sun and Kim (1997) analyze the compaction of iron and copper powders and conclude that a modified Cam-Clay model is the more suited.

Geindreau et al. (1999a;b) present experiments on lead powder for investigating the constitutive behaviour during hot pressing.

Numerical simulations of the powder compaction of a cup have been performed by Redanz (1999; 2001), using two different porous material models: that by Fleck et al. (1992a) and a material model including interparticle cohesive strength (Fleck, 1995).

Gu et al. (2001) have developed a constitutive model where the plastic flow is assumed to be representable as a combination of a distortion mechanism and a consolidation mechanism. For the distortion mechanism a Mohr-Coulomb type yield criterion with a non-associative flow rule is used, whereas for the consolidation mechanism an elliptical shape yield function with an associative flow rule is employed.

A simple isotropic and two anisotropic micromechanical models of compaction are compared in Henderson et al. (2001).

Subramanian and Sofronis (2001) present a micromechanical model for interaction between densification mechanisms in powder compaction. Elastic deformation, power-law creep deformation, diffusional mass transport on the interparticle contact areas and pore surfaces are taken into account.

**Sands and granular materials.** The constitutive models developed in this field are concerned with the behaviour of geotechnical materials and refer essentially to low pressures, corresponding to Phase I compaction. Despite microstructural differences, sands and clays have similar macroscopic properties, so that constitutive models have been developed for both materials, assuming that the behaviour of sands and clays is governed by different zones of the same yield surface. For instance, it is common to assume that a dense sand behaves as a strongly overconsolidated clay. Other models have been specifically developed for sands. A fundamental feature of granular materials is the presence of plastic strains at low load levels, and the occurrence of a notable anisotropy induced by the loading process. The main elastic-plastic models which can describe these aspects are very briefly summarized in the following.

Mróz et al. (1978) and Prevost (1977) propose the use of vector-valued yield functions coupled with kinematic hardening to describe the mechanical behaviour of granular materials, in such a way extending to soils an approach originally proposed for metals by Mróz (1967) and by Iwan (1967).

Dafalias and Popov (1975) and Krieg (1975) simplify the Mróz approach, by suggesting the use of two surfaces only: an inner one, describing the elastic behaviour, is subjected to kinematic hardening and an outer one, modelling the extent of the plastic strains, is fixed and named "bounding surface". A similar approach has been proposed also by Hashiguchi and Ueno (1977) with the so-called "subloading surface" model.

More specifically oriented towards sands at low loading levels are the models proposed by Ghaboussi and Momen (1982) and by Poorooshasb and Pietruszczak (1985), based on two surfaces only, shaped as two open cones with non circular cross-section and with vertices coinciding with the origin of the stress space.

Zienkiewicz and Mróz (1984) and Pastor and Zienkiewicz (1986) propose a generalized plasticity model, in which the directions of plastic loading and unloading, as well as the amplitude of the plastic strains, are defined at each point of the stress space without making reference to a yield surface or to a consistency criterion.

De Boer (1988) has developed constitutive equations for granular materials based on a "single-surface" criterion and a non-associative flow rule. A review of the state of the art of the macroscopic porous media theory can be find in de Boer (2000).

Morland et al. (1993) describe a model for the uniaxial compaction of granular materials valid at small strains.

Borja and Wren (1995), Wren and Borja (1997) present a methodology for deriving the overall constitutive relations for granular materials based on microme-

chanical concepts. The overall response is obtained using particulate mechanics and considers the particle-to-particle interaction at contact points. Finally, a methodology for calculating the overall tangential moduli for periodic assemblies of circular disks has been proposed.

Anand and Gu (2000) have been formulated a large deformation three-dimensional elasto-plastic constitutive model for dry granular materials at low pressure, based on the classical Mohr-Coulomb criterion. The model is used to predict the formation of shear bands in plane strain compression and expansion and to predict the stress state in a static sand pile.

The main drawback of the described models is that the same sand behaves as different materials at different densification levels. Such problem becomes important in the description of ceramic powders, where the density is a variable of the primary importance, subjected to evolution during the forming process. Recently, Manzari and Dafalias (1997) and Gajo and Muir Wood (1999a,b) have independently developed an approach originally proposed by Muir Wood et al. (1994) to account for the dependence of the mechanical properties from the densification level by means of a state parameter (Been and Jefferies, 1985). Both models are based on two open conical surfaces, with vertex coinciding with the origin of the reference system; in particular, some restrictions existing in the model of Manzari and Dafalias (1997) are overcome in the approach of Gajo and Muir Wood (1999a,b) by means of the use of a normalized stress space. Recently Gajo et al. (2001) have extended this model to include the elastic anisotropy induced during the deformation process. In this way it has been possible to show how this model can describe the onset of strain localization and the post-localization behaviour, both under axisymmetric and biaxial conditions.

**Ceramic powders.** A general review of the powder pressing technology is given in Volume 22 of the *MRS Bulletin* (1997). It is explicitly stated in the introduction (Ewsuk, 1997) that the numerical modelling of densification phenomena is still an open problem, that there is a need of employing a large strain formulation and that several techniques (slip-casting, pressure filtration, centrifugal casting, injection molding, tape casting, gelcasting) are much less known than the widely used dry-powder pressing. Similar conclusions are reached by Schilling et al. (1998). It may be therefore appreciated that the state-of-the-art of mechanical modelling of ceramic densification process is still rather poor. Some contributions to this specific field are reviewed below.

Shima and Mimura (1986) illustrate experimental results and formulate a yield criterion for ceramic powders. They claim that the experimental evidence points towards an associative flow-law.

The model by Kuhn et al. (1991) reduces the problem of Phase I densification to the search for the critical load of an arch. This model may be useful both for practical applications and in the description of experimental results. However, the model may be too limited to allow an adequate extension for modelling an entire compaction process.

Höhl and Schwedes (1992) discuss the possibility of extending to powders the models used in geomechanics. However, they do not formulate a new model able to improve on the limits of those currently used in geomechanics.

The relationship between density and tensile strength of ceramic powders are discussed by Bortzmeyer (1992a). A micromechanical model to determine the microscopic behaviour of packing during tensile tests is also proposed. Bortzmeyer (1992b) presents experimental results carried out on a zirconia powder with a standard triaxial apparatus and numerical simulations performed using a Cap-model with non-associative flow rule.

Experimental results are given in Shima and Saleh (1993), where it is proved that a strong anisotropy is induced during pressing. This effect is then modelled in terms of kinematic hardening.

Ahzi et al. (1993) employ crystal plasticity models for the analysis of the forming of BSCCO superconductive powders. Owing to the peculiar lamellar microstructure of their powders, their analysis is hardly extensible to powders with a different microstructural morphology.

A relationship is proposed by Santos et al. (1996) to describe the variation of the density as function of the applied pressure, valid for alumina powders under pressures above 150 MPa.

Brandt and Nilsson (1998; 1999) present an elastic-plastic model for powder compaction and sintering, with a kind of anisotropic hardening taken from models used in geomechanics (DiMaggio and Sandler, 1971; Sandler and Rubin, 1979).

A comparison between the model of Shima and Oyane (1976) and the model of Fleck et al. (1992a) is presented by Kim and Kim (1998), whereas Sun and Kim (1997) and Sun et al. (1998) compare the same models to the Cam-clay. A similar work is that of Park and Kim (2001), where a yield function is proposed, with associative flow-law and independent of the third stress invariant.

Phase I densification is interpreted by Cuitiño and Gioia (1999) as a phase transformation. Their model is based on a micromechanical approach and is applicable to a wide class of granular materials. However, it may be difficult to extend it to Phases II and III.

The "CRADA group" (Aydin et al. 1997a,b; Ewsuk et al. 2001; Keller et al. 1998; Zipse, 1997) reports about a model for powder compaction based on a proposal by Sandler and Rubin (1979) for describing mechanical behaviour of concrete. Such model appears to be not fully adequate to the description of the ceramic powder behaviour in several respects (a small strain theory is used; the cohesion gain due to densification is not accounted for; the yield surface is independent of the third

stress invariant; the elastic parameters do not depend on both the current stress and the past history; hardening is present only in the cap region).

On the basis of the above reported state-of-the-art, we feel it is possible to conclude as follows:

- the description of industrial processes, in the presence of complex geometries, still requires the use of phenomenological models and could hardly be based upon micromechanical approaches;

- a realistic elastic-plastic model, able to describe the powder compaction process, should include:
  - a large strain formulation (during forming the material undergoes strains exceeding 50%);
  - description of elastic phenomena (a rigid-plastic model would miss to capture several aspects which strongly affect the strength of the green bodies);
  - pressure-sensitivity of yielding;
  - dependence of the yield function on the third stress invariant;
  - non-associative flow-law;
  - closure of the yield function in compression, in order to simulate compaction during isostatic pressing;
  - hardening and softening. In particular, the hardening must describe the increase in cohesion of the material during the pressing (Bortzmeyer, 1992a);
  - explicit introduction of density as a state variable;
  - variation of the elastic moduli with density (Brown and Weber, 1988), an effect which could be accounted for by using the theory of elastic-plastic coupling (Hueckel, 1976);
  - progressive anisotropy, both elastic and plastic, due to plastic straining (Shima and Saleh, 1993; Uematsu et al. 1995).

- Moreover, the simulation of the forming process should include:
  - effects of the deformability of the die (Matsumoto, 1986);
  - effects of friction between powder and die (Song and Chandler, 1990);
  - simulation of the complete mold extrusion process, which may cause fracture upon unloading (Bortzmayer, 1996);
  - analysis of strain localization and relevant numerical treatment.

## 5.2. Experimental

Experimental investigation has been performed on the alumina powder described in Section 5.1. Experiments include uniaxial strain tests in a cylindrical mold, direct shear tests and biaxial flexure tests on the tablets obtained through uniaxial strain.

### 5.2.1. Uniaxial strain tests

Uniaxial deformation tests have been performed in a single-sided, cylindrical mold having inner diameter of 30 mm. A universal MTS 810 machine
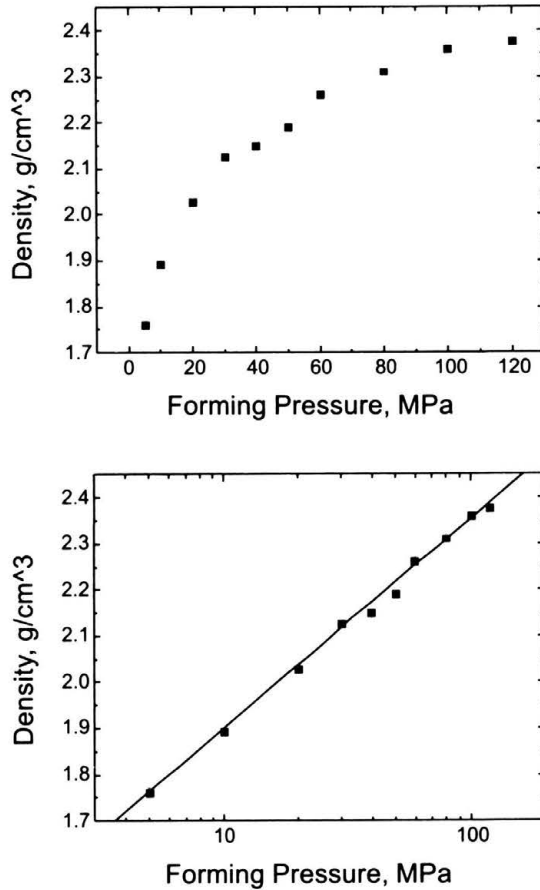


FIGURE 5.2. Compaction behaviour of the tested alumina powder (in a natural and semilog representation).

TABLE 5.2. Measured density as function of the forming pressure.

| Forming pressure (MPa) | Mean density (g/cm$^3$) | Standard deviation |
|:---:|:---:|:---:|
| 5 | 1.76 | 0.007 |
| 10 | 1.89 | 0.007 |
| 20 | 2.03 | 0.006 |
| 30 | 2.13 | 0.002 |
| 40 | 2.15 | 0.003 |
| 50 | 2.19 | 0.007 |
| 60 | 2.26 | 0.005 |
| 80 | 2.31 | 0.007 |
| 100 | 2.36 | 0.002 |
| 120 | 2.38 | 0.003 |

(by MTS Systems Gmbh, Berlin, Germany) has been employed. Tests were performed without lubricant at a 2 mm/min velocity of moving punch, for pressure levels ranging between 5 and 120 MPa. Five tests have been performed at given values of pressure, selected as 5, 10, 20, 30, 40, 50, 60, 80, 100, 120 MPa. After uniaxial strain, tablets have been weighted and measured, so that the mean density has been evaluated. A quantity of 8 g of powder has been used for each test, discharged in the mold from an height of 10 cm and shaken. Experiments were performed at a relative humidity of 28%. Results are reported in Fig. 5.2 (in a natural and semi-logarithmic representation) and Table 5.2. As can be noted from Fig. 5.2, points in the semi-logarthmic plot lies on a straight line, accordingly to DiMilia and Reed (1983a,b) and Lukasiewicz and Reed (1978). A representative load $F$ versus vertical displacement $s$ curve is reported in Fig. 5.3, from which the density $\rho$ versus pressure $p$ curve can be obtained through the simple relationships

$$\rho = \frac{M}{A(h_0 - s)}, \qquad p = \frac{F}{A}, \tag{5.1}$$

(where $A$ is the sample cross-section area, $M$ its mass and $h_0$ its initial height), as shown in Fig. 5.4. The strong influence of the die and machine deformations can be appreciated in Fig. 5.3. The changes in the slope of the curve in Fig. 5.4 identify the three compaction phases. In particular, the breakpoint and joining pressures are approximately 1 MPa and 20 MPa, respectively. However, the latter point is much less evident from the graph than the former. Note that results reported in Fig. 5.2 agree well with those
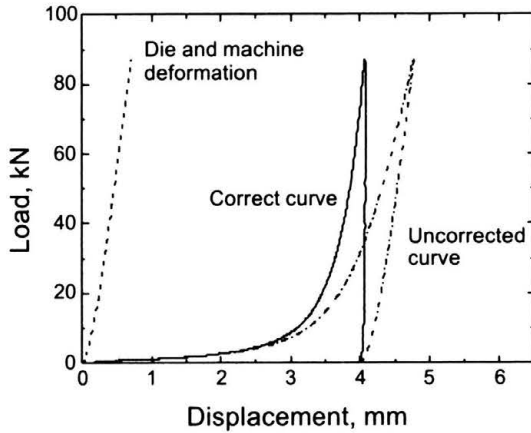
FIGURE 5.3.　Load vs. displacement curve in uniaxial strain.
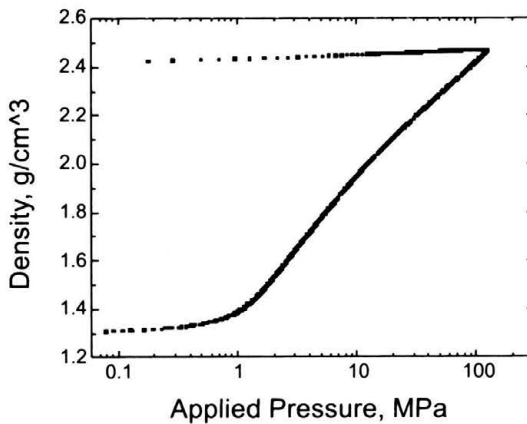


FIGURE 5.4.　Compaction diagram in uniaxial strain (semilog representation).

reported in Fig. 5.4, except that Phase I behaviour is not visible in the former figure.

### 5.2.2.　Biaxial flexure strength tests

Biaxial flexure strength tests have been performed on the tablets obtained through uniaxial strain, following the indications of ASTM F 394. For this test the velocity of the cylindrical ram was 0.4 mm/min. The increase in biaxial flexural strength as a function of the forming pressure is shown in Fig. 5.5.
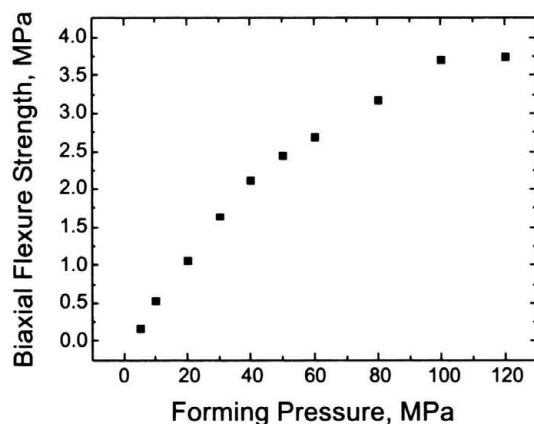
FIGURE 5.5. Biaxial flexure strength as related to forming pressure.

Results are in good agreement with existing data (Reed, 1995) and clearly show the mechanism of cohesion increase, as related to densification.

A SEM micrograph of the fracture surface after a biaxial flexural test of a tablet formed at a pressure of 50 MPa is shown in Fig. 5.6. Note that 50 MPa is the optimal forming pressure indicated by the powder manufacturer.
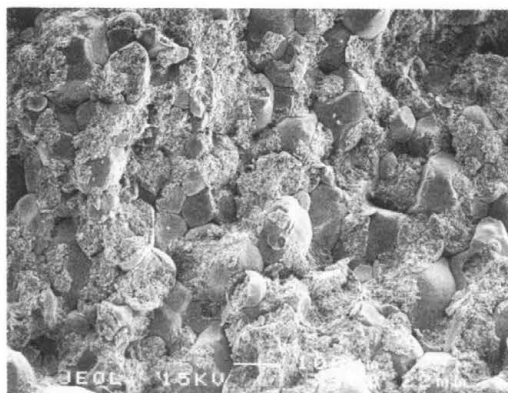


FIGURE 5.6. Fracture surface of a tablet formed at 50 MPa pressure (bar $= 100\,\mu$m).

Fracture results to be partially transgranular and partially intergranular. It may be noted that there are clusters of deformed granules with low intergranular porosity. Figure 5.7 is a detail of a fractured granule, where the aggregate crystals are visible.
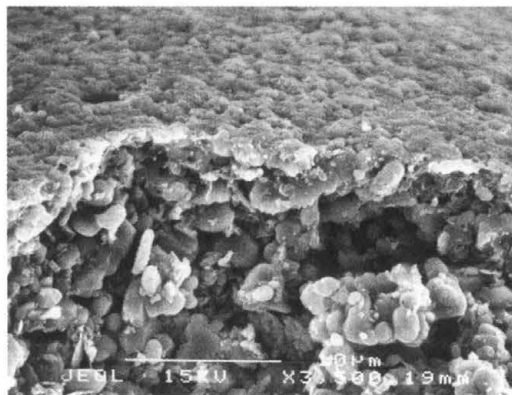
FIGURE 5.7. Particular of Fig. 5.6 (bar $= 10\,\mu$m).

### 5.2.3. Direct shear tests

A few direct shear tests have been performed using a standard geotechnical apparatus. The apparatus consists of a shear box which contains the sample and which is split in the mid-height. When a normal force is applied, the horizontal force required to induce a movement of the upper half of the sample with respect to the lower half is measured. This test is useful for the evaluation of the friction angle of a granular material, like the alumina powder in Phase I of densification. In order to investigate the shear strength of the cohesionless material, a low vertical pressure was applied: three values were considered, namely, 200, 500, and 1000 kPa. The samples were formed by carefully pouring the ceramic powder within the shear box. Shearing was performed at a velocity of 0.2 mm/min. The variation of the vertical displacement of the sample upper surface and of the applied shear force during shearing is shown in Figs. 5.8 and 5.9.

The samples have the typical behaviour of a loose sand, with compressive volumetric strains during shearing, without a peak strength followed by a softening phase. The fact that the samples sheared at 500 kPa and 1000 kPa of vertical pressure have the same volumetric strains is probably related to a slightly looser initial condition of the former sample. It can be observed that, except for the test performed under a vertical stress of 200 kPa, the steady state condition typical of the critical state is not reached and at the end of the test the strength and the volumetric strains of the samples are still slightly increasing. This effect is more pronounced at larger applied vertical pressures
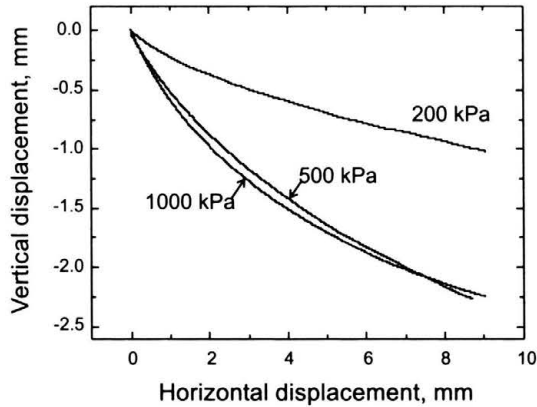
FIGURE 5.8. Vertical vs. horizontal displacements of three samples, for different vertical pressures (200, 500 and 1000 kPa).
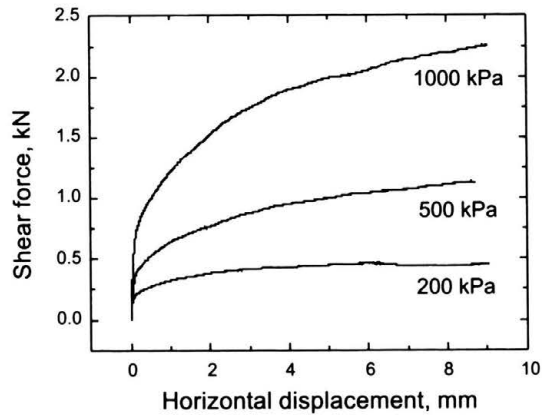


FIGURE 5.9. Shear force vs. horizontal displacement of three samples, for different vertical pressures (200, 500 and 1000 kPa).

and is probably connected to the progressive deformation and rupture of the grains constituting the alumina powder occurring during shearing even at low confining pressures. This is consistent with the experimental evidences that very large shear strains are necessary to reach the steady state in sands when grain crushing occurs.

The maximum shear force reached at the end of the test is plotted in Fig. 5.10 as a function of the applied vertical load. The results clearly lie on a straight line and may be interpreted following the Coulomb-Mohr
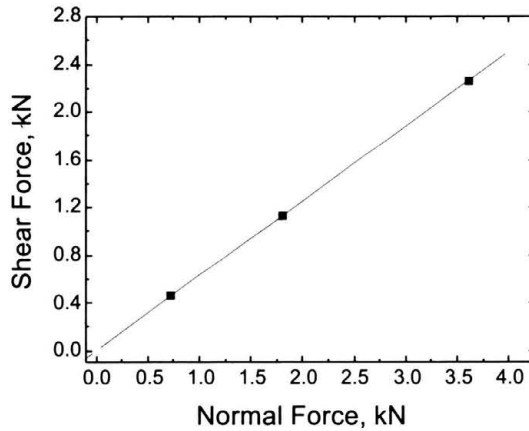
Figure 5.10. Maximum shear force at different vertical loads.

failure criterion, to yield a friction angle approximately equal to 32°. Accepting a slight approximation, this angle was considered the critical state friction angle in the following simulations. Moreover, since experimental information on the shear strength of the cohesive material after compaction are missing, the measured friction angle was assumed to characterise also the behaviour of the material after compaction.

## 5.3. Modelling and calibration

It can be concluded from the above reported experiments that a plasticity model is the best candidate for a phenomenological description of powder compaction. First, in fact, an elastoplastic model is needed to simulate the irreversible deformation representing the forming process itself, second, it allows determination of *residual stresses* after forming, a fundamental parameter for design purposes.

In general, an elastoplastic model is formulated as a nonlinear relationship between objective rates of stress $\overset{\nabla}{T}$ and strain $D$

$$\overset{\nabla}{T} = \begin{cases} \mathcal{E}[D] - \dfrac{1}{H} < Q \cdot \mathcal{E}[D] > \mathcal{E}[\mathbf{P}] & \text{if } f(T, \mathcal{K}) = 0, \\ \mathcal{E}[D] & \text{if } f(T, \mathcal{K}) < 0, \end{cases} \tag{5.2}$$

where $\mathcal{E}$ is the elastic fourth order tensor, the operator $< \cdot >$ denotes the Macaulay brackets which associate to any scalar $\alpha$ the value $< \alpha > = \max\{\alpha, 0\}$,

$f$ is the yield criterion, function of the stress measure $\boldsymbol{T}$ and of a generic collection of *state variables* $\mathcal{K}$ (which may for instance describe the density of the material), $\boldsymbol{Q}$ and $\boldsymbol{P}$ are the yield function and plastic potential gradients, respectively ($\boldsymbol{Q} = \boldsymbol{P}$ for associative elastoplasticity). Finally, the plastic modulus $H$ is related to the hardening modulus $h$ through

$$H = h + \boldsymbol{Q} \cdot \mathcal{E}[\boldsymbol{P}]. \tag{5.3}$$

Elastoplasticity as described by the rate equations (5.2) is a broad context in which many constitutive assumptions are to be introduced. The similarity of the Phase I compaction with the deformation of granular materials suggests the possibility of using a model already developed for geomaterials. In particular, on the basis of our experimental results, we have decided to employ a finite strain version of the Cam-clay model (Roscoe et al. 1958, 1963; Roscoe and Poorooshasb, 1963; Roscoe and Burland, 1968; Schofield and Wroth, 1968). The model is based on the following assumptions:

$\mathcal{A}$1. Yield function:

$$f(\boldsymbol{T}, p_c) = M^2 p^2 - M^2 p_c p + q^2, \tag{5.4}$$

where $p = -\operatorname{tr}\boldsymbol{T}/3$ is the hydrostatic stress component, $q = \sqrt{3J_2}$ (with $J_2 = \boldsymbol{T} \cdot \boldsymbol{T} - 3p^2$) is the Mises stress, $M$ is a material constant and $p_c$ is a hardening parameter.

$\mathcal{A}$2. Associative plastic flow rule:

$$\boldsymbol{Q} = \frac{M^2}{3}(p_c - 2p)\boldsymbol{I} + 3\boldsymbol{S}, \tag{5.5}$$

where $\boldsymbol{S} = \boldsymbol{T} - (\operatorname{tr}\boldsymbol{T})/3\boldsymbol{I}$ is the stress deviator.

$\mathcal{A}$3. Isotropic hardening rule:

$$p_c = p_{c0} \exp(1 + e_0)\frac{1 - J^p}{\Lambda - \kappa J^p}, \tag{5.6}$$

where $J^p = \det \boldsymbol{F}^p$, being $\boldsymbol{F}^p$ the plastic part of the deformation gradient $\boldsymbol{F}$, $p_{c0}$ and $e_0$ are the initial values of hardening parameter and void ratio, respectively, (the void ratio is defined as the ratio between the volume of voids and volume of solid phase). $\Lambda$ is the logarithmic hardening modulus and $\kappa$ the logarithmic elastic bulk modulus and are represented by the slopes of plastic and elastic branches of the $e$ vs. $\log p$ curve obtained under isotropic compression.

It may be anticipated, however, that the Cam-clay model has definitive limitations when applied to the modelling of ceramic powders. In particular, a more refined model should include the following features, not considered in the Cam-clay:

- the yield function should depend also on the third stress invariant;
- a non-associative flow-law should be introduced;
- the hardening should describe the increase in cohesion of the material during the pressing;
- the elastic moduli should depend on the increase in cohesion during densification (an effect that could be accounted for by using the theory of elastic-plastic coupling, Hueckel, 1976).

Among the above points, the dependence of the cohesion on the relative density is the more important. In the Cam-clay model, in fact, the material remains cohesionless during all the process of inelastic deformation. On the contrary, the proper description of cohesion gain during forming is a fundamental aspect for design purposes.

Calibration of the model has been performed on the basis of our experiments (with the exception of the Poisson's ratio, which was estimated from values available in the literature). In particular, the values of the parameters $\Lambda$ and $\kappa$ were deduced from the slopes of curves obtained by loading and unloading the samples in the uniaxial strain test. For this evaluation, we have assumed a constant ratio between the horizontal $\sigma_h$ and vertical $\sigma_v$ stresses equal to 0.47, as deduced from the formulae

$$\frac{\sigma_h}{\sigma_v} = 1 - \sin\phi,$$

which is currently used for granular media ($\phi$ is the angle of internal friction). The values of parameters used in the subsequent numerical simulations are summarized in Table 5.3.

TABLE 5.3. Values of material parameters estimated from experiments.

| Elastic logarithmic bulk modulus $\kappa$ | | 0.040 |
|---|---|---|
| Logarithmic hardening modulus $\Lambda$ | | 0.290 |
| Material constant $M$ | | 1.287 |
| Initial value of hardening parameter $p_{c0}$ | (MPa) | 0.648 |
| Initial values of void ratio $e_0$ | | 2.054 |
| Initial confining pressure $p_0$ | (MPa) | 0.063 |
| Poisson's ratio $\nu$ (taken from literature) | | 0.26 |

## 5.4. Numerical simulations

Numerical simulations with finite elements have been performed – within the environment allowed by the commercial code ABAQUS (Hibbitt, Karlsson & Sorensen, 2001) – to simulate forming of the (axisymmetric) piece shown in Figs. 5.11 and 5.12. Four pieces where formed at a final mean pressure of 100 MPa starting from 5 g of powder. The axisymmetric mesh used in the simulations is shown in Fig. 5.13. Axisymmetric 4-node elements (CAX4) have been used.
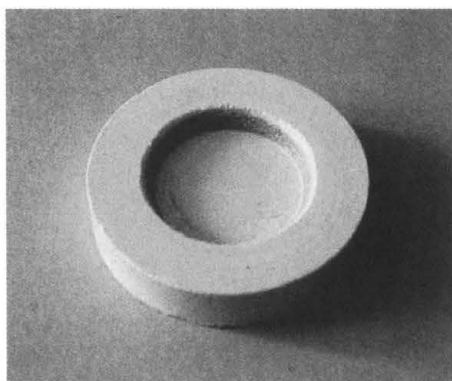
FIGURE 5.11. Photograph of the formed piece.
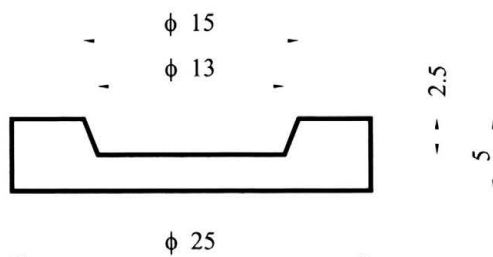
FIGURE 5.12. Geometry of the formed piece (dimensions in mm).

The following assumptions have been introduced:
- the die is undeformable;
- the contact between powder and die walls is smooth;
- the initial configuration is that shown in Fig. 5.13.
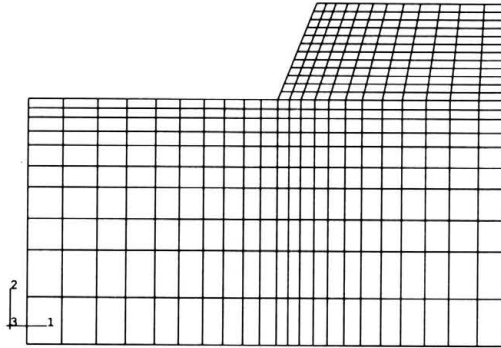
FIGURE 5.13.  Initial mesh.
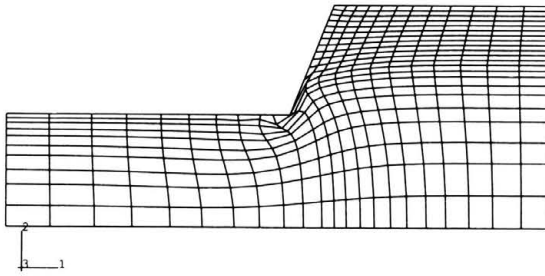
FIGURE 5.14.  Deformed mesh at the end of step 1.
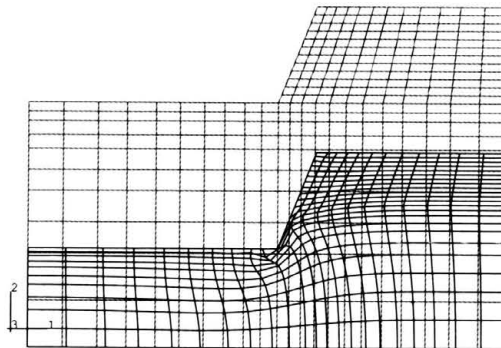
FIGURE 5.15.  Initial and deformed (end of step 1) meshes.

It may be worth noting that the above assumptions are not particularly strong in our specific analysis. In particular, we remark that, due to the large strains that will be reached during pressing, the assumption that the initial configuration shown in Fig. 5.13 is homogeneous does not affect much final results.

After the initial state – defined by initial values of void ratio and confining pressure – has been defined, the loading history is assigned, which is divided in the following three steps:

1. forming is prescribed by imposing the motion of the upper part of the boundary (3.78 mm, corresponding to the value measured during forming at the final load of 50 kN);

2. unloading is simulated by prescribing null forces on the upper part of the boundary;

3. ejection is simulated by prescribing null forces on all the boundary.

Due to the fact that the Cam-clay model is not defined for tensile stresses and is singular for null mean stress, the last of the above steps cannot be concluded and the analysis ends up when the applied external forces are reduced to a minimal percent of the values at the beginning of the step. Obviously, a more fundamental constitutive approach would require the definition of a gain of cohesion and related variation of elastic properties, as mentioned in Section 5.3.

The deformed mesh at the end of step 1 is shown in Fig. 5.14, whereas the same mesh superimposed on the initial mesh is shown in Fig. 5.15. It can be noted that the elements near the corner of the punch are unphysically distorted so that results in this zone should not be considered realistic.

It is immediate to conclude from Figs. 5.14, 5.15 that the deformation suffered by the piece is quite high. The hydrostatic stress component $p$ (taken positive when compressive), the Mises stress $q$ and the void ratio are reported in Figs. 5.16–5.18, respectively, at the end of step 1.

Excluding the small, unrepresentative zone near the corner of the punch, the hydrostatic stress $p$ ranges from 25.3 MPa to 108 MPa and the Mises stress $q$ from 15.4 MPa to 70.1 MPa. These values show that the stress is highly inhomogeneous. The $q/p$ ratio ranges from 0.31 to 1.14, so that it is always inferior than the value of $M$.

Values of the hydrostatic and Mises stress components at the end of step 2 are reported in Figs. 5.19 and 5.20, whereas the map of void ratio is shown
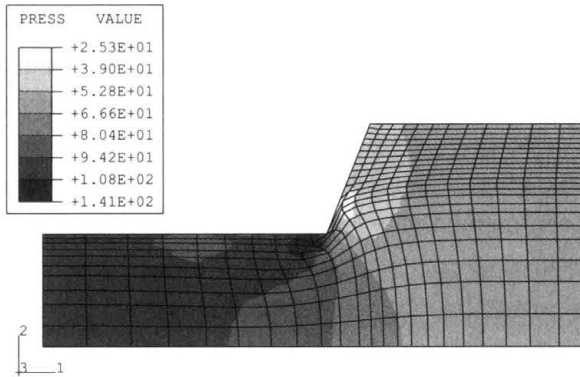
PRESS    VALUE
— +2.53E+01
— +3.90E+01
— +5.28E+01
— +6.66E+01
— +8.04E+01
— +9.42E+01
— +1.08E+02
— +1.41E+02

FIGURE 5.16.  Distribution of hydrostatic stress component (MPa) at the end of step 1.



MISES    VALUE
— +1.54E+01
— +2.45E+01
— +3.36E+01
— +4.27E+01
— +5.19E+01
— +6.10E+01
— +7.01E+01
— +1.11E+02
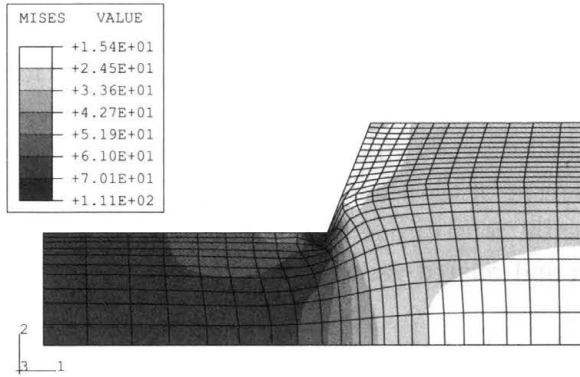
FIGURE 5.17.  Distribution of Mises stress (MPa) at the end of step 1.



VOIDR    VALUE
— +4.42E-01
— +4.94E-01
— +5.45E-01
— +5.97E-01
— +6.49E-01
— +7.00E-01
— +7.52E-01
— +8.76E-01
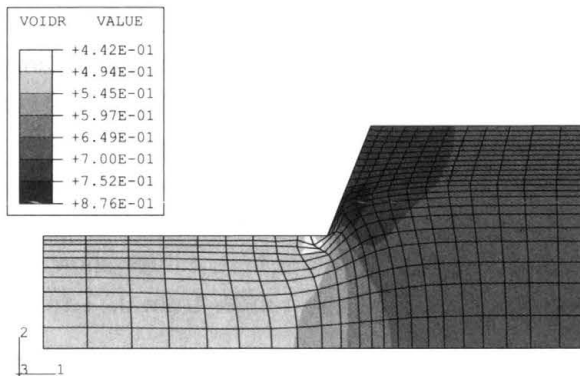
FIGURE 5.18.  Void ratio distribution at the end of step 1.
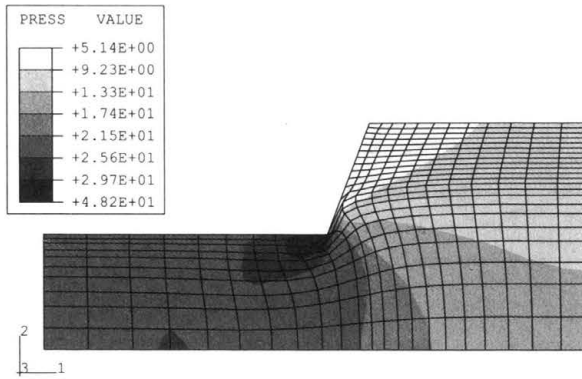
FIGURE 5.19. Distribution of hydrostatic stress component (MPa) at the end of step 2.
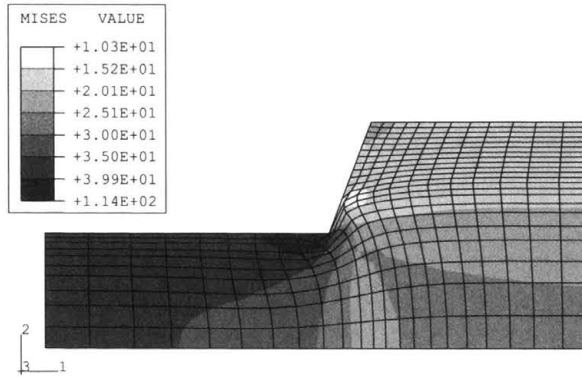


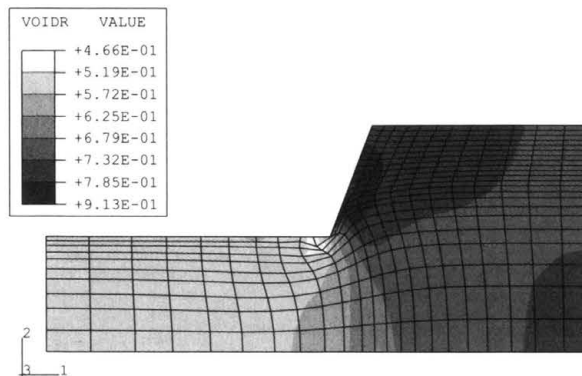FIGURE 5.20. Distribution of Mises stress component (MPa) at the end of step 2.



FIGURE 5.21. Void ratio distribution at the end of step 2.

in Fig. 5.21. It may be important to note that residual stress is quite high, due to the lateral constraint still present at the end of step 2. The knowledge of the lateral stress is important for practical purposes since the force needed for the ejection of the final piece can be estimated through Coulomb friction law, when the lateral stress at the end of step 2 is known. A rough, but simple evaluation can be immediately obtained from numerical output at the end of step 2 employing the formula

$$\textit{ejection force} = \alpha \tan \phi \, (\textit{mean lateral stress} \times \textit{lateral surface of the piece}),$$

where $\phi$ is the powder friction angle (equal to $32°$ in our case) and $\alpha$ is a coefficient dependent on the roughness of the die wall and ranging between 0 and 1, typically $\alpha = 0.6$.

The deformed mesh at the end of step 3 is shown in Figs. 5.22 and 5.23. In the latter figure, the deformed mesh is superimposed on the initial. The springback effect and the shape distortion are evident.
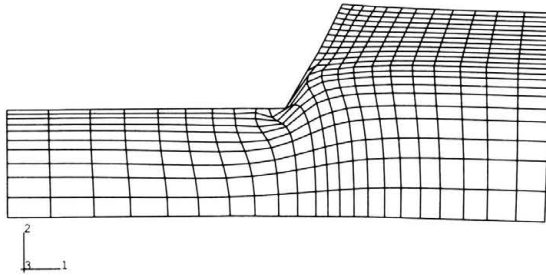


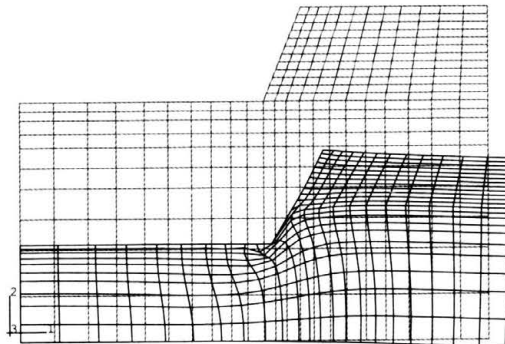FIGURE 5.22. Deformed mesh at the end of step 3.



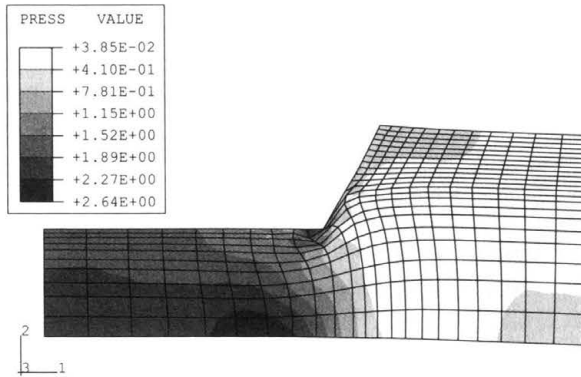FIGURE 5.23. Initial and deformed (step 3) meshes.

FIGURE 5.24. Distribution of hydrostatic stress component (MPa) at the end of step 3.
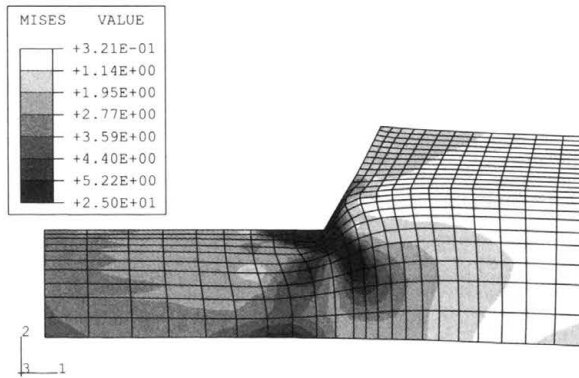


FIGURE 5.25. Distribution of Mises stress component (MPa) at the end of step 3.
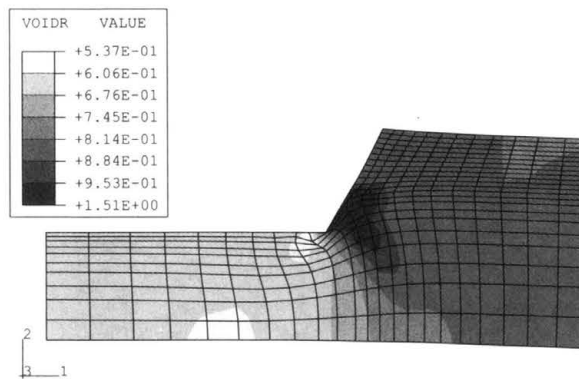


FIGURE 5.26. Void ratio distribution at the end of step 3.

The residual stress distribution at the end of forming is reported in
Figs. 5.24 and 5.25, where the hydrostatic stress and the Mises stress compo-
nents are also shown. The void ratio distribution is finally shown in Fig. 5.26.
Excluding the small, unrepresentative zone near the corner of the punch,
the hydrostatic stress $p$ ranges now between 0.038 MPa and 2.64 MPa and
the Mises stress $q$ between 0.32 MPa and 5.22 MPa. Moreover, the void ratio
varies between 0.54 and 0.95. It can be noted that the minimum void ratio is
usually associated with the maximum residual mean stress. The results sug-
gest that two annular, concentric zones of material are formed, the inner of
which is subject to high compressive mean stresses, whereas the outer tends
to be subject to tensile stresses. This can represent a potentially danger-
ous situation, in which the tensile stresses tend to open possible microcracks
induced by ejection on the external surface of the piece, leading to serious de-
fects formation in the green. However, even when the green is approximately
free of macro defects, its mechanical behaviour and shrinkage during future
sintering are deeply affected by the inhomogeneities in the residual stress and
density distributions.

Finally, we note from Figs. 5.24–5.26 that an annular zone of very dense
material forms near the bottom of the sample. This prediction is indeed
confirmed by the visual inspection of the formed sample, clearly showing an
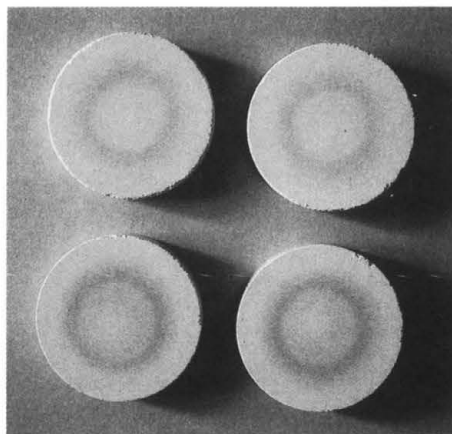annular dark zone, Fig. 5.27.



FIGURE 5.27.  Photograph of the bottom side of the formed samples.

Experimental and simulated load displacement curves during forming of the piece shown in Fig. 5.11 are compared in Fig. 5.28 (natural and semilogarithmic representations are reported), where a satisfying agreement can be noted.
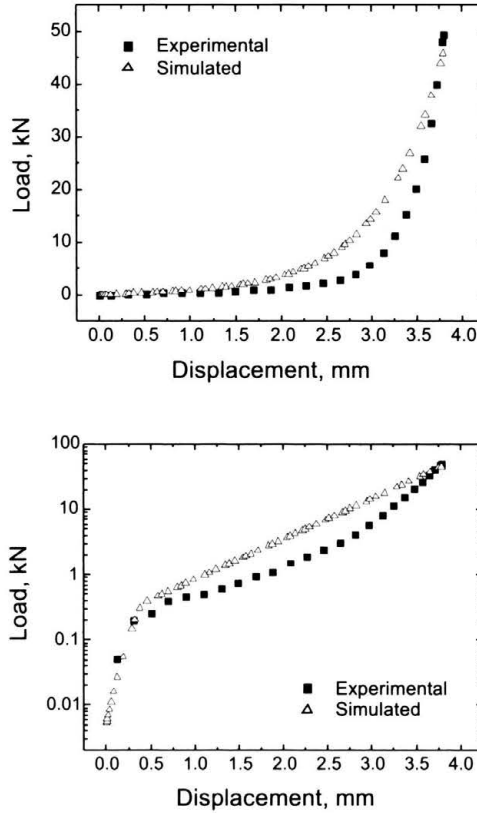


FIGURE 5.28. Experimental and simulated load vs. displacement curves, in a natural and semilog representation.

## 5.5. Conclusions

Results discussed in the present chapter represent a first step toward the development of a model capable of realistically describing forming processes of ceramic materials. Even if the experimental results are still incomplete and the employed elastoplastic model, the Cam-clay, does not describe properly

some important feature of material behaviour – as for instance the strong relation between density and cohesion – our results demonstrate that it is possible to realistically predict:

- the springback effect and related shape distortion,
- the force needed for mold ejection,
- the residual stress distribution,
- the density distribution and the related presence of defects in the green body.

The final remark is related to the prediction of defects in the sintered piece and therefore its investigation has an important practical meaning.

In closure, we mention that the modelling presented in this Chapter can be extended in different directions. Referring to thermoplasticity, the sintering phase might be covered by modelling, so that simulation could be extended to the entire production process. Moreover, both sintering aids and powder characteristics might enter the elastic-plastic constitutive laws, so that the optimal powder composition and morphology could be predicted for different forming problems.

## 5.6. References

AHZI, S., ASARO, R.J. and PARKS, D.M. (1993), Application of crystal plasticity theory for mechanically processed BSCCO superconductors, *Mech. Materials*, Vol.15, pp.201-222.

AKYSANYA, A.R., COCKS, A.C.F. and FLECK, N.A. (1994), Hydrostatic compaction of cylindrical particles, *J. Mech. Phys. Solids*, Vol.42, pp.1067-1085.

ANAND, L. and GU, C. (2000), Granular materials: constitutive equations and strain localization, *J. Mech. Phys. Solids*, Vol.48, pp.1701-1733.

ARIFFIN, A.K., GETHIN, D.T. and LEWIS, R.W. (1998), Finite element simulation and experimental validation for multilevel powder compact, *Powder Metallurgy*, Vol.41, pp.189-197.

ARZT, E. (1982), The influence of an increasing particle coordination on the densification of spherical powders, *Acta metall.*, Vol.30, pp.1883-1890.

AYDIN, I., BRISCOE, B.J. and SANLITURK, K.Y. (1997), Dimensional variation of die-pressed ceramic green compacts: comparison of a finite element modelling with experiment, *J. Eur. Ceram. Soc.*, Vol.17, pp.1201-1212.

AYDIN, I., BRISCOE, B.J. and OZKAN, N. (1997), Modeling of powder compaction: a rewiev, *MRS Bull.*, Vol.22, pp.45-51.

BEEN, K. and JEFFERIES, M.G. (1985), A state parameter for sands, *Géotechnique*, Vol.35, pp.99-112.

BORJA, R.I. and WREN, J.R. (1995), Micromechanics of granular media Part I: Generation of overall constitutive equation for assemblies of circular disks, *Comput. Methods Appl. Mech. Engrg.*, Vol.127, pp.13-36.

BORTZMEYER, D. (1992a), Tensile strength of ceramic powders, *J. Material Sci.*, Vol.27, pp.3305-3308.

BORTZMEYER, D. (1992b), Modelling ceramic powder compaction, *Powder Technology*, Vol.70, pp.131-139.

BORTZMEYER, D. (1996), Die pressing and isostatic pressing, in: *Materials Science and Technology*, Cahn, R.W., Haasen, P. and Kramer, E.J., (Eds.), VCH, Weinheim, pp.127-152.

BRANDT, J. and NILSSON, L. (1998), FE-simulation of compaction and solid-state sintering of cemented carbides, *Mech. Cohesive-Frict. Mater.*, Vol.3, pp.181-205.

BRANDT, J. and NILSSON, L. (1999), A constitutive model for compaction of granular media, with account for deformation induced anisotropy, *Mech. Cohesive-Frict. Mater.*, Vol.4, pp.391-418.

BROWN, S.B. and ABOU-CHEDID, G. (1994), Yield behaviour of metal powder assemblages, *J. Mech. Phys. Solids*, Vol.42, pp.383-399.

BROWN, S.B. and WEBER, G.A. (1988), A constitutive model for the compaction of metal powders, *Mod. Dev. Powder Metall.*, Vol.18-21, pp.465-476.

CUITIÑO, A.M. and GIOIA, G. (1999), Early compaction of cohesive powders, Technical Report, Dept. Mech. & Aerosp. Engineering, University of New Jersey.

DAFALIAS, Y.F. and POPOV, E.P. (1975), A model for non linear hardening materials for complex loadings, *Acta Mechanica*, Vol.21, pp.173-192.

DE BOER, R. (2000), Contemporary progress in porous media theory, *Appl. Mech. Rev.*, Vol.53, pp.323-369.

DE BOER, R. (1988), On plastic deformation of soils, *Int. J. Plasticity*, Vol.4, pp.371-391.

DEIS, T.A. and LANNUTTI, J.J. (1998), X-ray computed tomography for evaluation of density gradient formation during the compaction of spray-dried granules, *J. Am. Ceram. Soc.*, Vol.81, pp.1237-1247.

DiMAGGIO, F.L. and SANDLER, I.S. (1971), Material model for granular soils, *J. Engng. Mech. Div. ASCE*, Vol.97, pp.935-950.

DiMILIA, R.A. and REED, J.S. (1983a), Stress transmission during the compaction of a spray-dried alumina powder in a steel die, *J. Am. Ceram. Soc.*, Vol.66, pp.667-672.

DiMILIA, R.A. and REED, J.S. (1983b), Dependence of compaction on the glass transition temperature of the binder phase, *Am. Ceram. Soc. Bull.*, Vol.62, pp.484-488.

EWSUK, K.G. (1997), Compaction science and technology, *MRS Bull.*, Vol.22, pp.14-16.

EWSUK, K.G., ARGÜELLO, J.G., ZEUCH, D.H., FARBER, B., CARINCI, L., KANIUK, J., KELLER, J., CLOUTIER, C., GOLD, B., CASS, R.B., FRENCH, J.D., DINGER, B. and BLUMENTHAL, W. (2001), CRADA develops model for powder pressing and die design, Part one, *Am. Ceram. Soc. Bull.*, Vol.80, pp.53-60.

EWSUK, K.G., ARGÜELLO, J.G., ZEUCH, D.H., FARBER, B., CARINCI, L., KANIUK, J., KELLER, J., CLOUTIER, C., GOLD, B., CASS, R.B., FRENCH, J.D., DINGER, B. and BLUMENTHAL, W. (2001), CRADA develops model for powder pressing and die design, Part two, *Am. Ceram. Soc. Bull.*, Vol.80, pp.41-46.

FLECK, N.A. (1995), On the cold compaction of powders, *J. Mech. Phys. Solids*, Vol.43, pp.1409-1431.

FLECK, N.A., KUHN, L.T. and McMEEKING, R.M. (1992a), Yielding of metal powder bonded by isolated contacts, *J. Mech. Phys. Solids*, Vol.40, pp.1139-1162.

FLECK, N.A., OTOYO, H. and NEEDLEMAN, A. (1992b), Indentation of porous solids, *Int. J. Solids Struct.*, Vol.29, pp.1613-1636.

GAJO, A. and MUIR WOOD, D. (1999a), Severn-Trent sand: a kinematic hardening constitutive model for sands: the q-p formulation, *Géotechnique*, Vol.49, pp.595-614.

GAJO, A. and MUIR WOOD, D. (1999b), A kinematic hardening constitutive model for sands: the multiaxial formulation, *Int. J. Num. and Anal. Meth. Geomechanics*, Vol.23, pp.925-965.

GAJO, A., BIGONI, D. and MUIR WOOD, D. (2001), Stress induced elastic anisotropy and strain localisation in sand, in: *Proc. of the International Workshop on Localisation and Bifurcation in Geomechanics*, Perth (Australia), Balkema, in press.

GEINDREAU, C., BOUVARD, D. and DOREMUS, P. (1999a), Constitutive behaviour of metal powder during hot forming. Part I: Experimental investigation with lead powder as a simulation material, *Eur. J. Mech. A/Solids*, Vol.18, pp.581-596.

GEINDREAU, C., BOUVARD, D. and DOREMUS, P. (1999b), Constitutive behaviour of metal powder during hot forming. Part II: Unified viscoplastic modelling, *Eur. J. Mech. A/Solids*, Vol.18, pp.597-615.

GERMAN, R.M. (1984), *Powder Metallurgy Science*, MPIF, Princeton, New Jersey.

GHABOUSSI, J. and MOMEN, H. (1982), *Modelling and Analysis of Cyclic Behaviour of Sands, Soil Mechanics Transient and Cyclic Loads*, Pande, G.N. and Zienkiewicz, O.C., (Eds.), pp.313-342.

GLASS, S.J. and EWSUK, K.G. (1997), Ceramic powder compaction, *MRS Bull.*, Vol.22, pp.24-28.

GU, C., KIM, M. and ANAND, L. (2001), Constitutive equations for metal powders: application to powder forming processes, *Int. J. Plasticity*, Vol.17, pp.147-209.

GURSON, A. and MCCABE, T. (1992), Experimental determination of yield functions for compaction of blended metal powders, in: *Proc. MPIF/APMI World Congress on Powder Metallurgy and Particular Materials*, S. Francisco, USA, pp.133-145.

HASHIGUCHI, K. and UENO, M. (1977), Elasto-plastic constitutive laws of granular materials, Const. Eqs. of Soils. 9th ICSMFE, pp.73-82.

HAUSNER, H.H. and KUMAR-MAL, M. (1982), *Handbook of Powder Metallurgy*, Chemical Publishing.

HELLE, H.S., EASTERLING, K.E. and ASHBY, M.F. (1985), Hot-isostatic pressing diagrams: new developments, *Acta Metall.*, Vol.33, pp.2163-2174.

HENDERSON, R.J., CHANDLER, H.W., AKISANYA, A.R., CHANDLER, C.M. and NIXON, S.A. (2001), Micro-mechanical modelling of powder compaction, *J. Mech. Phys. Solids*, Vol.49, pp.739-759.

HIBBITT, KARLSSON & SORENSEN (2001), *ABAQUS Theoretical & User's Manuals, Release 6.2.*, Pawtucket, RI, USA.

HÖHL, H.W. and SCHWEDES, J. (1992), Extension of elastoplastic constitutive models with respect to cohesive bulk solids, *Powder Technology*, Vol.70, pp.31-42.

HUECKEL, T. (1976), Coupling of elastic and plastic deformation of bulk solids, *Meccanica*, Vol.11, pp.227-235.

IWAN, W.D. (1967), On a class of models for the yielding behaviour of continuous and composite systems, *J. Appl. Mech.*, Vol.34, pp.612-617.

JERNOT, J.P., JOUANNOT, P. and BHANU PRASAD, P. (1994), Three-dimensional simulation of metallic powder compression: global microstructural approach, *Powder Metallurgy*, Vol.37, pp.197-200.

KELLER, J.M., FRENCH, J.D., DINGER, B., McDONOUGH, M., GOLD, B., CLOU-TIER, C., CARINCI, L., VAN HORN, E., EWSUK, K. and BLUMENTHAL, B. (1998), Industry, government team to improve ceramic manufacturing, *Am. Ceram. Soc. Bull.*, Vol.77, pp.52-57.

KENKRE, V.M., ENDICOTT, M.R., GLASS, S.J. and HURD, A.J. (1996), A theoretical model for compaction of granular materials, *J. Am. Ceram. Soc.*, Vol.79, pp.3045-3054.

KHOEI, A.R. and LEWIS, R.W. (1999), Adaptive finite element remeshing in a large deformation analysis of metal powder forming, *Int. J. Numer. Meth. Engng.*, Vol.45, pp.801-820.

KIM, K.T. and KIM, J.S. (1998), Stage 1 compaction behaviour of tool steel powder under die pressing, *Powder Metallurgy*, Vol.41, pp.199-204.

KRIEG, R.D. (1975), A practical two-surface plasticity theory, *J. Appl. Mech.*, Vol.42, pp.641-646.

KUHN, L.T., McMEEKING, R.M. and LANGE, F.F. (1991), A model for power consolidation, *J. Am. Ceram. Soc.*, Vol.74, pp.682-685.

LEWIS, R.W., JINKA, A.G.K., and GETHIN, D.T. (1993), Computer-aided simulation of metal powder die compaction processes, *Powder Metall. Int.*, Vol.25, pp.287-293.

LEWIS, R.W. and KHOEI, A.R. (1998), Numerical modelling of large deformation in metal powder forming, *Comput. Methods Appl. Mech. Engng.*, Vol.159, pp.291-328.

LIPPMANN, H. and IANKOV, R. (1997), Mathematical modelling of sintering during powder forming processes, *Int. J. Mech. Sci.*, Vol.39, pp.585-596.

LORDI, N.G. and CUITIÑO, A.M. (1997), Compaction of pharmaceuticals, *MRS Bull.*, Vol.22, pp.34-37.

LUKASIEWICZ, S.J. and REED, J.S. (1978), Character and compaction response of spray-dried agglomerates, *Am. Ceram. Soc. Bull.*, Vol.57, pp.798-801.

MANZARI, M.T. and DAFALIAS, Y.F. (1997), A critical state two-surface plasticity model for sands, *Géotechnique*, Vol.47, pp.255-272.

MATSUMOTO, R.K.L. (1986), Generation of powder compaction response diagrams, *Comm. Am. Cer. Soc.*, Vol.69, C-246-247.

MORLAND, L.W., SAWICKI, A. and MILNE, P.C. (1993), Uni-axial compaction of a granular material, *J. Mech. Phys. Solids*, Vol.41, pp.1755-1779.